Engineering Bicontinuous Interfaces for Enhanced Mechanical Performance

by

Benjamin K. Derby

A dissertation submitted in partial fulfillment
of the requirements for the degree of
Doctor of Philosophy
(Materials Science and Engineering)
in The University of Michigan
2020

Doctoral Committee:

Professor Amit Misra, Chair
Professor Michael Atzmon
Assistant Professor John Heron
Assistant Professor Liang Qi

Benjamin K. Derby

benderby@umich.edu

ORCID: 0000-0003-4692-4615

To my friends and family whose shoulders must be sore now that I have stood on them for so long.

"To be good, and to do good, is all we have to do." - John Adams

"Opportunity is missed by most people, because it is dressed in overalls and looks like work." - Thomas Edison

ACKNOWLEDGEMENTS

The path to obtaining a doctoral degree is viewed by some as long and arduous. While my journey has often been marked by moments of doubt, worry, and late nights, the moments of pure joy, abounding fun, and profound self-discovery made this part of my life worth every minute. The life-long friends I have met along the way have forever made me a better person and for that I am truly thankful. The people I acknowledge here deserve more credit than they will ever realize, and I just hope that I provided them at least half of the love and support that they shared with me.

I would like to first express my sincere appreciation to my advisor, Professor Amit Misra. I knew I wanted to become Amit's first graduate student when he valued my career and much as the research I was about to embark upon. One could not ask for a better scientist and leader to emulate as a student. His guidance allowed me to develop into a scientist that asks critical questions about our material world and seek answers those questions so that we can have a positive impact on the world. It is without question that my leadership capability was greatly expanded under Amit's mentorship. I learned something new about myself after every conversation I

have had with Amit. The devotion he has for his students, his passion for materials science, and his appreciation for good mentorship has me hoping that I become half the advisor he was to me one day. Thank you for all of the great conversations, Amit.

I would also like to extend special thanks to the rest of my committee, Prof. John Heron, Prof. Michael Atzmon, and Prof. Liang Qi. I have been fortunate to learn much from each of my committee members, whether this was through class instruction, direct one-on-one discussions, research collaborations, or even through students or post-docs that learned from them and passed this knowledge onto me.

Special thanks are extended to Kevin Baldwin, Dr. Nathan Mara, Dr. Nan Li, and Dr. Khalid Hattar for their support while conducting research at Los Alamos and Sandia National Laboratories.

My graduate school journey would have been much less fun if it were not for the organizations I was lucky enough to be a part of during my time at the University of Michigan. I would foremost like to thank the MSE Graduate Student Council. I found a home with this organization here at UM. The opportunity to lead the MSE GSC was a true honor of mine. I sincerely hope that the efforts of the GSC made the lives of our graduate students just a little better. My personal success and the organization's success would not have existed without the continued support of Prof. Amit Misra (Department Chair), Prof. Anisha Tuteja (graduate chair), Renee Hilgendorf (graduate coordinator), Patti Vogel, Shelley Fellors and the rest of the

MSE staff for their support of the MSE GSC goals.

I want to acknowledge my scientific collaborators with which I have worked while at UM. In no particular order I would like to extend my deepest gratitude towards Yuchi Cui, Dr. Qian Lei, Dr. Kai Sun, Dr. Michael Demkowicz, Dr. Ankit Kumar, Dr. Chris Adams, Dr. Haiping Sun, Dr. Shujuan Wang, Dr. Lumin Wang, Mohsen Taheri, Max Powers, Dr. Remi Dingreville, Dr. Raymundo Arryave, Dr. Di Chen, Dr. Yungzhi Wang, Hari Haran, Wesley Higgins, Dr. George Pharr, and Dr. Yong Wang.

The friendships I developed outside of the lab made this journey all the worthwhile. It is hard to write in words how blessed I am to have shared so many memories with my friends during this part of my life. I am most thankful for all of the utter joy, gut-hurting laughter, and lending ears my friends shared. These folks kept me happy, sane, and helped me to develop into better versions of myself each day. To Zachary Mendel, Laina Weinman, Avi Bregman, Kelsey Mengle, Bryan Vansaders, Benjamin Swerdlow, Adi Viswanath, Brian Iezzi, Kathleen Chou, Kartheek Gangadhara, Max Powers, Erika Salem, Jill Wenderott, Yuchi Cui, Michael Chen, Jake Garvis, and Alex Thum, I thank you from the bottom of my heart. I hope I provided you half of the friendship and love you provided me. And to my TRI family (esp. Sarah, Jan, and Theresa), I truly thank you for some of the best fun and laughter I have had in my life. And finally, for all my friends (from childhood, undergrad, and in-between) that are living their best lives in other locations outside of Ann Arbor, I also thank

you for your support, love, and in a lot of cases, coming to visit.

My graduate school career would be nothing without the love and support from my family back in NY and in Germany: my selfless mother, Anita; my dependable father, Doug; my courageous sister, Melanie; my caring godmother, Angie; my humorous godfather, Ken; my kind uncle and aunt, Udo and Monika; my best friend, Brandon Mack; and all of my grandparents, aunts, uncles, and cousins. I miss you all every day, and I am entirely grateful for your presence in my life. I also specially recognize my late grandmother and grandfather, Anna und Leo. My family, past and present, has taught me to value and believe in myself.

Lastly, I must thank Sydney for all of the love and understanding she has shown me since she so unexpectedly and wonderfully entered my life. It seems proper to both thank Ann Arbor for bringing me to you and thank you for bringing me through the end of graduate school. I cannot wait for many more "10,000 hours" with you.

TABLE OF CONTENTS

LIST OF FIGURES

Figure

LIST OF TABLES

Table

ABSTRACT

In this work, we report on the evolution of phase-separated morphologies in co-sputtered Cu-Mo films as a result of varying substrate temperature and deposition rate during deposition. A transition from vertically-oriented concentration modulations to laterally-oriented modulations followed by randomly-oriented modulations was observed in the Cu-Mo films because of changing substrate temperature at constant deposition rate. A refinement of the Cu-Mo domains was observed at increasing deposition rate at a constant substrate temperature. A coarsening of phase-separated domains was also observed with increasing substrate temperature. While these morphologies have been observed in state of the art research and technology, no work has shown the transition between these morphologies for a given system. The phase separation kinetics that controlled film morphology were limited by the surface in-

terdiffusion of each species as the film grew in thickness. Control over the surface interdiffusion length was achieved by altering the deposition temperature and material flux.

Additionally, a new processing route has been discovered through which far-from-equilibrium, metastable architectures with unprecedented properties are synthesized. This novel architecture contains many orders of hierarchy with multiple concentration modulation wavelengths. At one length scale, the matrix consists of lateral modulations of BCC Mo and pseudomorphic BCC Cu with a wavelength of 10nm. FCC, Cu-rich islands of approximate 250nm diameter are woven in-between the Mo-Cu matrix and contain ordered arrays of pseudomorphic, FCC, Mo-rich, coherent precipitates of approximately 1.0nm diameter spacing. The resulting material exhibits unprecedented mechanical behavior of extensive plastic deformability at room temperature. Traditional phase separated thin film morphologies are monolithic in architecture with only one concentration wavelength. By carefully manipulating the self-assembly kinetics through the deposition rate, we processed a structure with multiple concentration modulation wavelengths.

Furthermore, with the introduction of high power impulse magnetron sputtering (HiPIMS) as a new sputtering technique, the range of morphologies achieved during deposition has been expanded. In this work, we co-deposit thin films composed of immiscible Cu, Fe constituents via traditional DC magnetron sputtering (DCMS) and compare this to deposition of the same Cu, Fe system using the HiPIMS technique.

Microstructural features, including porosity, columnarity, and roughness were altered as a function of the Cu and Fe metal ion current. The nanostructured phase morphology also evolved from lateral concentration modulations of Cu and Fe deposited via DCMS to a more randomized phase domain structure when the film was deposited using HiPIMS. This change in structure is reasoned through an interdiffusion model as a function of deposition conditions.

Finally, this work reports on Helium (He) accumulation in these novel metal nanocomposites fabricated by phase separation in three-dimensions. Since, these nanocomposites are dense with semi-coherent interfaces that ultimately influence He implantation response. The effect of film morphology on three aspects of He response is investigated: size and distribution of He precipitates, He retention, and He-induced changes in mechanical properties. Transmission electron microscopy analysis showed that He bubbles agglomerated along the vertical phase boundaries in morphologies with lateral and random domains of Cu and Mo. Nuclear Reaction Analysis (NRA) and nanoindentation results show He retention and hardness is morphology dependent.

CHAPTER I

Introduction

Thin films are incorporated into a broad range of advanced technologies. They allow for the combination of bulk materials' properties with the surface properties of other materials. Thin films are used in applications that include scratch resistant coatings utilized in eye glasses [1], decorative films applied on modern cellular devices [2], and magnetic recording thin-film memory [3]. Much scientific investigation has concluded that the performance of thin films used in these applications is largely dependent on the nanostructure of the material comprising the film. As such, modern thin film research has focused on ascertaining how synthesis conditions manipulate the nanostructure of thin films in order to achieve the performance required for different applications. This dissertation aims to advance knowledge in the area of thin films by studying the fundamental synthesis physics required to manufacture and control the nanostructure of multi-component thin films. The novel materials shown in this work contain unique, bicontinuous interfaces, which enhance the films' mechanical response.

In many applications, thin films are processed with a monomodal nanostructure geometry. Monomodal geometries include thin films composed of a single phase material (e.g. Cu) or sequentially depositing two elements in a thin film multilayer laminate. These monomodal designs can be characterized by one length parameter as seen in Fig. 1.1(a).

The key structural features that characterize monolithic thin films, such as those presented in Fig. 1.1(a), can be defined by one length parameter [4]. For single phase films this is often the grain size, e.g. d, or the layer thickness for multilayer laminates, e.g. λ. The multilayer geometry, particular those which interface face-centered cubic and body-centered cubic materials, is of much interest to the thin films community as they often exhibit unique mechanical properties relative to bulk materials with the same composition.

It is a well established empirical observation that in bulk metallic materials, strength continues to increase with decreasing grain size (up until approximately 2030 nm) [5–7]. This has been since dubbed the Hall-Petch relationship. Grain boundaries act as dislocation, or crystal defect, pinning points, and as the spacing between these pinning points decreases, the stress required for dislocations to move throughout the material increases. In turn, the material hardens [4]. This relationship no longer holds once the grain size is decreased beyond approximately 20 nanometers [8].

The Hall-Petch relationship has been similarly observed in thin film materials by

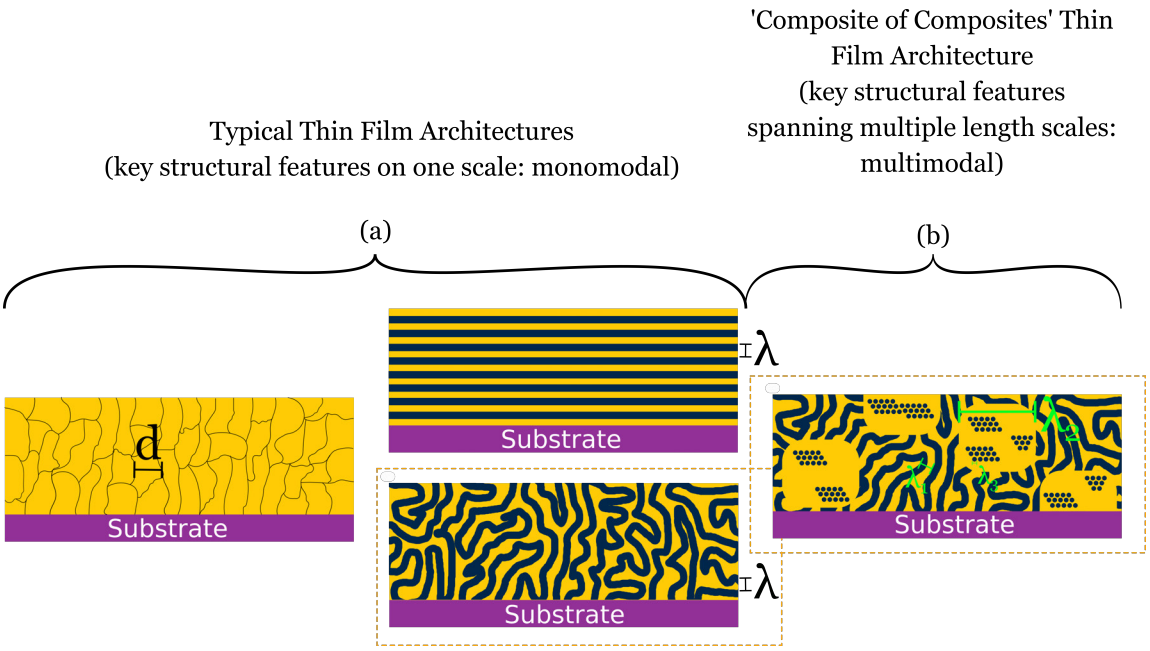

Figure 1.1: Schematic cartoons of various thin film architectures. (a) Monomodal films are characterized with key structural features defined on one length scale. Examples of this length scale include grain/column size or concentration modulation. (b) Multimodal films, also known as "Composite of Composite" architectures, are characterized with key structural features on multiple length scales. The two morphologies outlined by the dotted lines will be studied in this work.

Nix [9]. This work concluded that as film thickness decreased, the biaxial strength of the film material increased. Kang and Ho supported this theory by determining that the most influential factor in film strengthening was small grain sizes [10].

When studying multilayer metallic thin films, morphologies with unique semi-coherent interfaces between body-centered cubic and face-centered cubic were found to have ultra-high strengths [4]. Similar to bulk materials, it was observed that the bilayer period spacing in these multilayer films behave like grain boundaries in single phase thin films [4]. As the bilayer period shortens, the film yields at higher hardness [11]. Furthermore, multilayered thin films have been observed to show flow stresses beyond values predicted by the rule of mixtures, i.e., the average hardness of the two individual films [4]. The physical mechanism for this phenomenon is akin to single phase film grain boundary strengthening in that two-dimensional layer interfaces markedly restrict dislocation motion [12].

For these reasons, it has been well-established that the metallic thin film multilayer geometry presents significant mechanical advantages over conventional bulk metals. Among these properties are uniaxial strength values above 2 GPa [13, 14], and fatigue and radiation resistance [15, 16].

The scientific issue preventing the broad utilization of multilayers geometries in some applications, is their brittle-like failure [17]. Mara *et. al.* identified plastic flow localization as the mechanism for this behavior. Under mechanical load, plasticity does not distribute uniformly in the materials but instead concentrates into narrow

bands [17] when these types of materials are loaded under compression. The localized shear bands formed in the sample deform to high strains and eventually fracture even though the surrounding material remains undeformed. This phenomenon is shown in Fig. 1.2.

This work aims to address this scientific issue by designing nanocomposite materials that resist flow localization. By engineering bicontinous nanocomposite architectures, interfaces/surfaces, and compositions, we hypothesize that plastic flow will uniformly distribute in the material. Two driving design criteria have guided our choice for material architectures. Firstly, we will interface an FCC material with a BCC material with a short length scale from the start of the FCC domain to the end of the BCC domain, or λ in 1.1 . The created semi-coherent interface maximizes the strain hardening rate in the film similar to the strain hardening mechanism in FCC/BCC multilayer designs. Secondly, we will prevent flow-localized bands from permeating in the material by extending these multi-component interfaces in three dimensions in a bicontinuous architecture like that shown in Fig. 1.1(a) [18]. We hypothesize that extending these nano-metallic and bicontinuous interfaces in three dimensions, the material will resist flow localization under mechanical load.

This introductory chapter will start with a discussion and understanding of how deposition conditions are linked to coating morphology in monolithic thin films. Phase separation in bulk materials and in thin film materials is considered next. Theoretical and simulation models describing phase separation in thin films are then

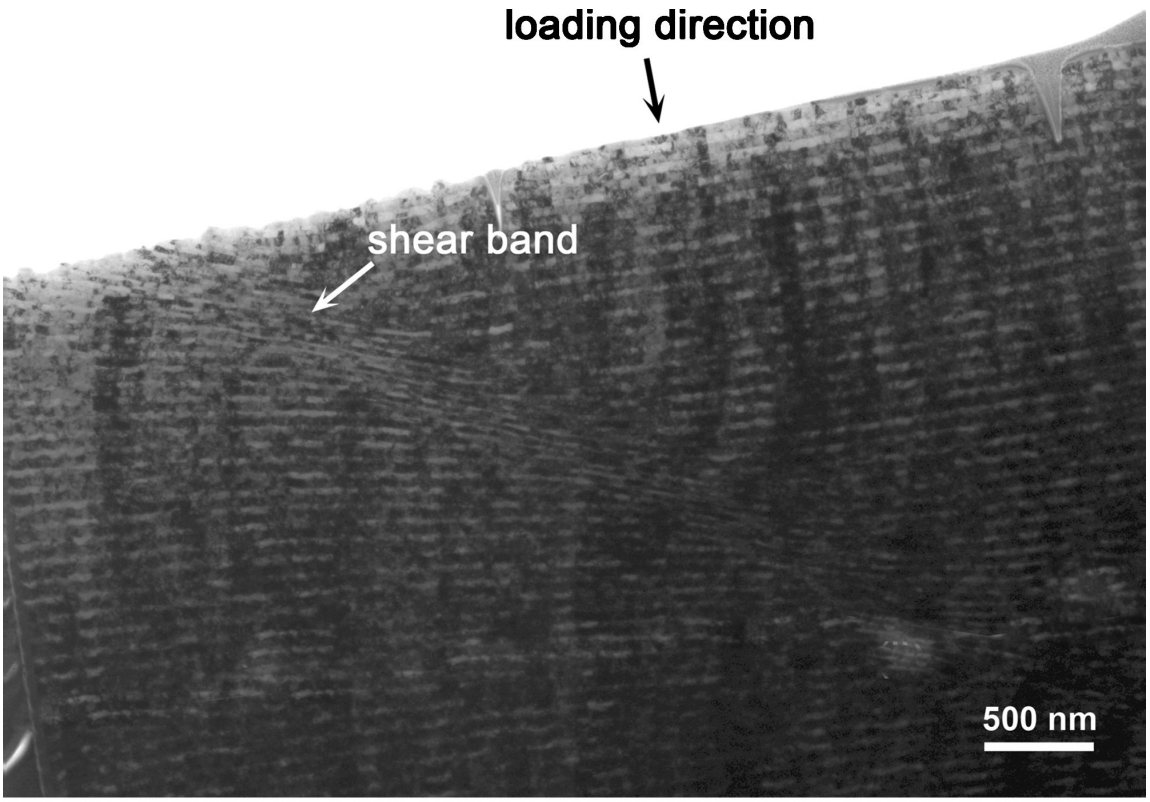

Figure 1.2: Shear banding or plastic flow localization into narrow region in a layered Cu/Nb multilayer thin film. From [17].

introduced as a guide to the development of these new, phase separated thin film geometries.

In proceeding chapters, a series of experimental and simulation results on phase separated, multi-component thin films are presented. Chapter 2 describes the experimental design and methods used to address the scientific challenge of designing new thin film morphologies that limit plastic flow localization. A discussion on homogeneous phase separation, or phase separation with one length scale, that led to the synthesis of bicontinuous interfaces in three dimension is presented for multiple element combinations in Chapter 3. Chapter 4 introduces novel heterogeneous thin film geometries in which several length scales of phase separation was observed. Comparison of the Cu-Mo phase separated films is then made to other FCC-BCC co-deposited thin films in Chapter 5. A unique deposition technique that alters the kinetic energy of arriving adatoms during film deposition is then presented in Chapter 6. Finally, Chapter 7 highlights the mechanical properties of these bicontinuous thin film morphologies.

1.1 Microstructure Development in Single Phase Thin Films

Physical vapor deposition (PVD) is a ubiquitously utilized processing technique to synthesize a wide variety of thin film materials [19]. The technique is relatively simple, but offers a number of tunable processing parameters to adjust the atomic growth of materials. These parameters include, but are not limited to, deposition temperature, substrate selection, depositing sequence, process gas pressure, atomic

peening rate (i.e. substrate bias), and deposition rate [4]. The PVD sputtering process is analogous to an electronic diode with a metal target material in the position of the cathode and a substrate at the anode. Charged species travel in one direction towards the target while species from the target material travel oppositely towards the substrate. Much research has gone into understanding how the deposition conditions during PVD alter the energetics of arriving species and in turn change the microstructure of the resultant film.

The seminal work linking microstructural development in thin films as a function of deposition conditions is the work done by Movchan and Demchishin [20]. These authors evaporated a number of metals (e.g. nickel) and oxides (e.g. aluminum oxide) at a range of substrate temperatures. Each deposited film showed similar morphology features as a function of deposition temperature. These morphologies were schematically represented in a structural zone diagram (SZD), which depicted common micro-structural features as a function of substrate temperature. This diagram has largely been useful in predicting film structures for relatively thick, single phase films. The authors defined a non-dimensional homologous temperature as their plot axis. This deposition parameter was defined as the film growth temperature normalized by the melting temperature of the film material (both in Kelvin),

$$T_h = T/T_m. \tag{1.1}$$

This parameter can be thought of as the kinetic energy given to a condensing

adatom on the growing film [21]. Movchan and Demchishin determined that three distinct structural zones could be established based on the many empirical data collected. [21]. Homologous temperature is low in Zone I, so constituent adatom mobility is also low. At such low substrate temperatures, condensing species tend to stick where they land on the substrate surface and continued nucleation events are prominent. This occurs when $T_h < 0.3$ and results in fibrous grains that are relatively small in diameter and point in the direction of the arriving material flux. The resultant microstructure is highly porous and contains a large number of lattice defects. These empirical results have since been supported by molecular dynamics (MD) [22] and Monte Carlo simulations [23].

When the deposition temperature is increased, surface diffusion of the arriving adatoms is activated and a more uniform columnar structure results [20]. In Zone II, or when $0.3 < T_h < 0.5$, grains extend through the film thickness and grain size increased with increasing substrate temperature. Theoretical simulation data show much agreement with this experimental data [23]. Srolovitz and colleagues showed similar microstructural development and a transition temperature between Zones I and II that agreed with Movchan and Demchishin's experiments using a Monte Carlo simulation method [23].

Finally, bulk diffusion is activated when $T_h > 0.5$. This activation induces grain recrystallization events that densify the film. The grains in this zone, Zone III, tend to be equiaxed and large in size [20].

With the onset of a film deposition technique known as magnetron sputtering another parameter needed to be included in the structure zone diagram, the process pressure. The seminal work considering this parameter was introduced by Thornton [24]. The results presented by Thornton *et. al.* were generally consistent with the previous research done by Movchan and Demchishin. The two axes used in the SZD presented by Thornton are the process pressure and the homologous temperature [4]. This figure is reproduced in Fig. 1.3.

The primary effect of changing the process gas pressure during deposition is where each zone begins. At relatively low gas pressures, a sputtered atom has several keV of kinetic energy. This is because the sputtered atoms encounter few collisions with the process gas as they travel to the substrate [25]. Additional process gas molecules act as scattering points and reduces the energy of arriving adatoms at higher process gas pressures [21]. As such, a broadened Zone I is observed at higher process pressures [4]. Unintentionally, Thornton described a parameter for kinetic energy effects on film growth by [21], namely the process gas pressure.

Thornton also observed a transition zone between Zones I and II, Zone T [24]. In this region, grains boundaries are present, but their structure is not columnar [26]. The Thornton Zone Diagram has been valuable as a morphology map for single phase films in which one simply need to know what morphology is desired to determine the requisite deposition parameters to use during processing and apply them.

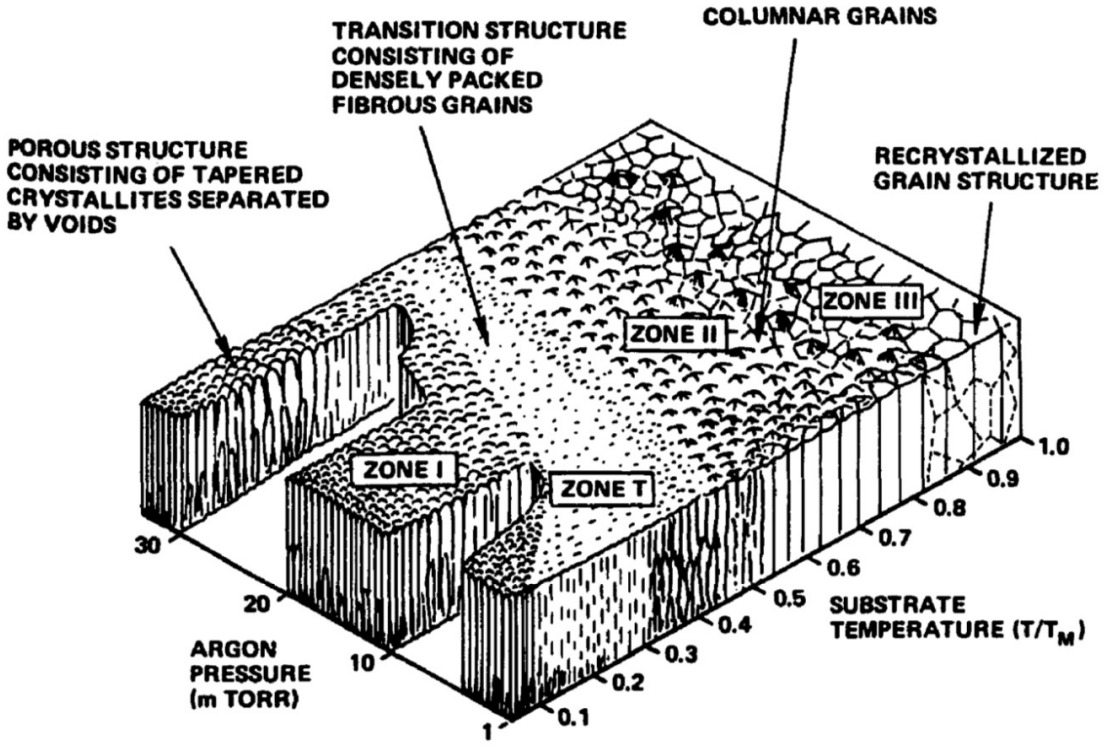

Figure 1.3: Structural Zone Diagram showing the effects of substrate temperature and argon process gas pressure on the microstructure of single phase metallic films. From [24].

1.2 Microstructure Development in Multi-Phase Thin Films

The preceding section demonstrated the close linkage between deposition conditions and the resultant thin film morphology in single phase materials. It essentially describes atomic motion over very short, lattice-sized, spacing [27]. Unfortunately, this single phase morphology maps provide little predictive capability for films that contain two or more phases such as that presented in Fig. 1.4. This shows two phases, yellow and blue, co-existing in a single film. In fact, little research has been done in synthesizing thin films with architectures as shown in Fig. 1.4 without complex annealing steps. A scientific challenge is being able to predict how deposition conditions manipulate the structure of these phase separated thin film geometries.

The connection between deposition conditions and phase separating materials has yet to be fully explored and remains an outstanding scientific challenge [28].

Using the thermodynamic property of immiscibility, we hypothesize that phase separation during thin film processing will result in morphologies like that shown in Fig. 1.4. Given adequate kinetic conditions, immiscibility in alloy systems allows for phase separation in a material that can create chemically sharp interfaces between two or more constituent elemental regions [29].

In the following sections, an introduction to phase separation in bulk materials – where the reaction front is determined by the system – is followed by a discussion on phase separation in thin film processing – where the reaction front is governed by the deposition parameters.

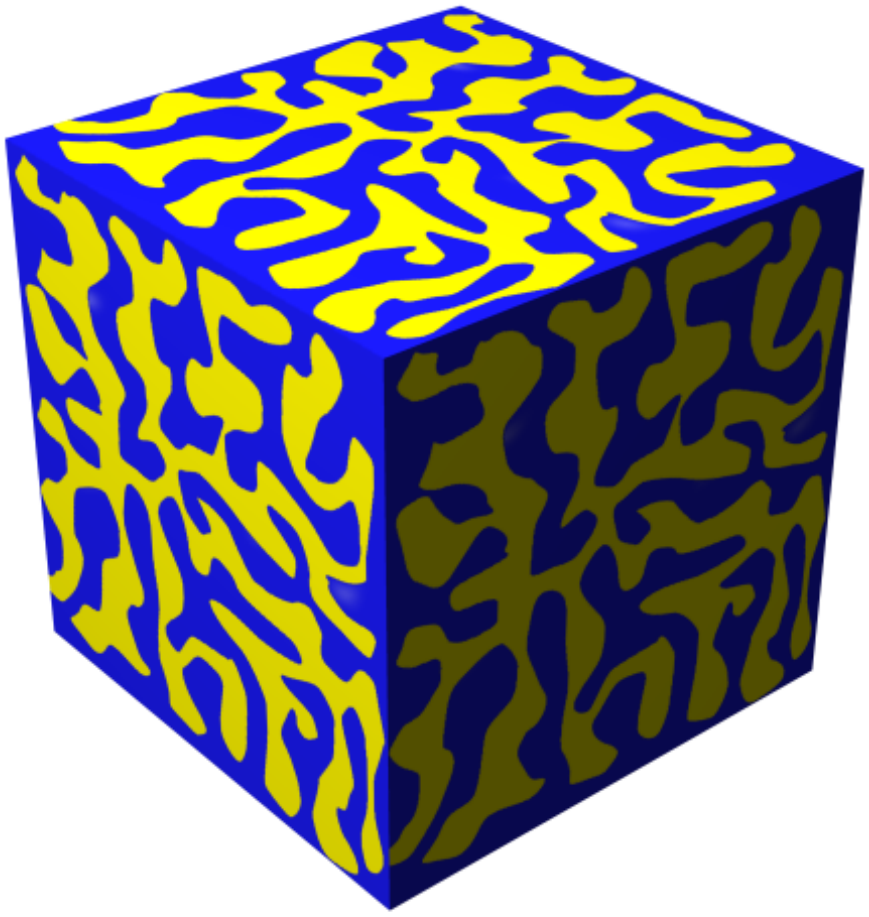

Figure 1.4: Schematic drawing of phase separated thin film morphology characterized with bicontinuous interfaces extending in three dimensions. The blue and yellow colors represent two phases within the material.

1.3 Phase Separation

The process of phase separation involves unnmixing two or more components in a homogeneous mixture [30]. In regions of the equilibrium phase diagram where more than one phase is stable, a homogenous mixture evolves towards phase separation as long as adequate kinetic conditions exist. There exist many paths for the system to relax to a new equilibrium state. These pathways were delineated by how large the activation barrier is to induce phase separation [31].

A nucleation and growth process occurs when the driving force is large. In this case the energy required to form new, incoherent interfaces during decomposition of a homogenous mixture is high. When decomposition requires no additional energy (i.e. zero activation energy), the system de-mixes via spinodal decomposition. Both of these processes have been well studied for bulk materials. We explore these two processes in turn.

1.3.1 Eutectoid Decomposition

When an activation energy barrier exists for phase separation to occur, nucleation and growth is the mechanism for decomposition [27]. One such pathway for nucleation and growth is eutectoid decomposition. Take a homogenous alloy with composition, c_0, as shown in Fig. 1.5(b). The free energy of the system can be reduced from G_1 by forming two new phases, α and β. However, Fig. 1.5(b) shows a positive curvature in the Gibbs free energy curve and any small changes in the composition results in a free energy increase. Thus, the initial alloy with composition,

c_0, is metastable with respect to $\alpha + \beta$. If the system can spontaneously form α and β phases with c_α and c_β, respectively, the free energy of the system would be at a global minimum. This process costs free energy (i.e. activation energy barrier), as it would require the creation of discontinuous interfaces between the two phases.

In most cases, the morphology of a system having undergone eutectoid decomposition is described by alternating lamellae of α and β phases [32]. Subject to kinetic restraints, the lamallae spacing is determined by the length that ultimately lowers the Gibbs free energy of the system. Cahn noted that the segregation reaction during eutectoid phase separation is system dependent and is limited to the interface between the decomposing homogeneous alloy and the products [31]. As such, the decomposition products will be supersaturated.

1.3.2 Spinodal Decomposition

Consider the Gibbs free energy curve for a homogeneous solution presented in Fig. 1.5(a).

As Cahn argued in his seminal work on the subject [31], at the homogenous composition of, c_0, the curvature of the free energy is negative. Symbollically, this is the same as writing $\partial^2 G/\partial c^2 < 0$ within the composition range between c_1 and c_2. Any small composition fluctuation of say, Δc, causes one part of the system to become more concentrated at the expense of another. This will lower the Gibbs free energy per mole of solution from G_1 to G_2 for the inhomogeneous alloy. Accordingly, the system is unstable to small compositional fluctuations and spontaneous decom-

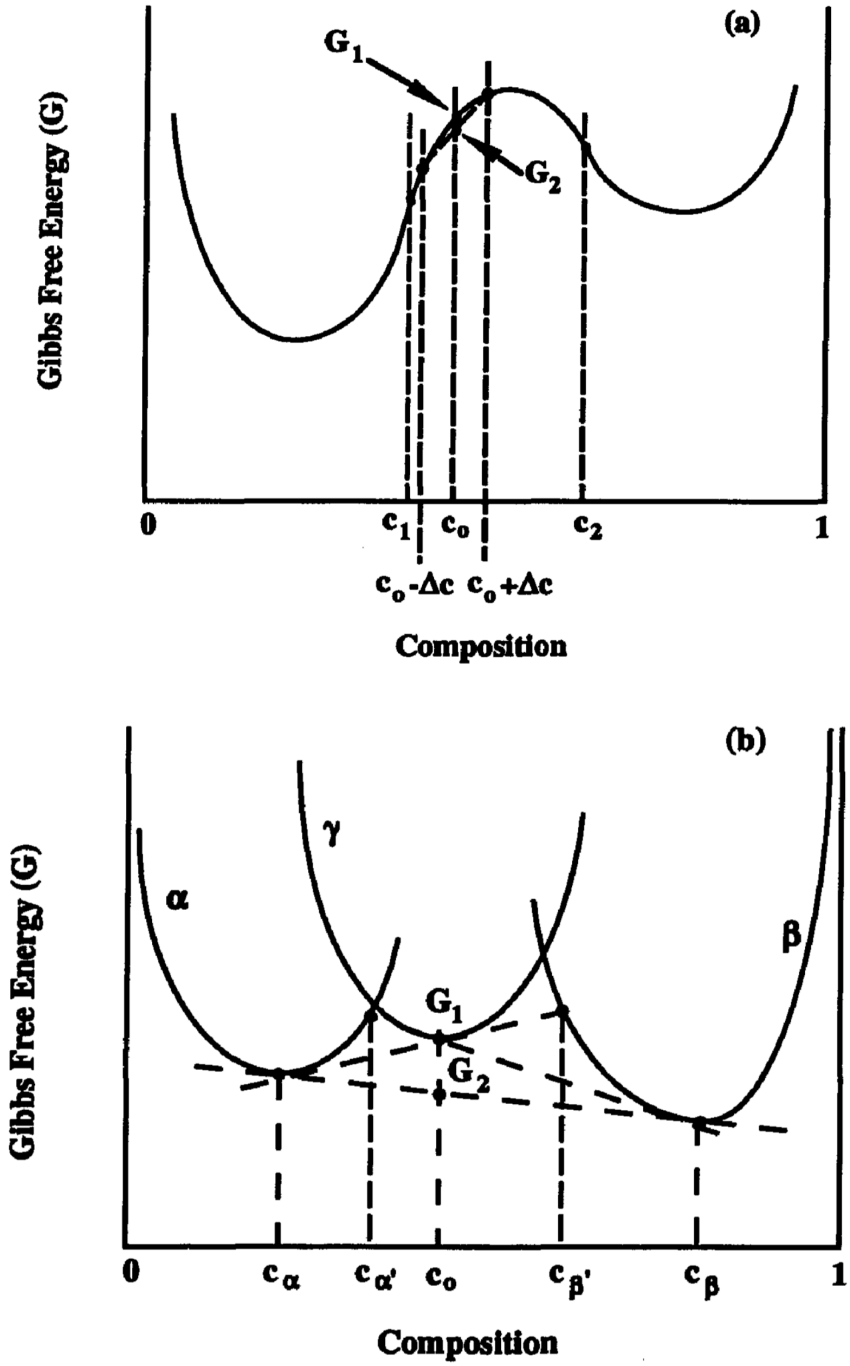

Figure 1.5: (a) A Gibbs free energy-composition diagram for a system undergoing spinodal decomposition. (b) A Gibbs free energy-composition diagram for a system undergoing eutectoid decomposition. In both cases, the systems' composition tends towards that which lowers the free energy. From [27].

position will occur through uphill diffusion (i.e. negative chemical interdiffusivity) throughout the material until the terminal composition is achieved [27].

The morphology of a sample during the early stages of spinodal decomposition is characterized by a dominant wavelength proportional to the chemical variation across the sample [33]. Coherency strains begin to develop at later stages of spinodal decomposition and eventually incoherent precipitates form making the final morphology indistinguishable from a material having decomposed via nucleation and growth.

1.4 Phase Separation in Thin Films

A review of the literature suggests two processing routes to achieve a phase separated thin film morphology, such as the one depicted in Fig. 1.5.

Low temperature deposition of a homogeneous alloy will phase separate if exposed to post-deposition annealing [34–37]. In almost all cases, this results in randomly oriented concentration modulations of two or more phases [37]. Muller and coworkers showed that post-deposition annealing of a Cu-Ta system results in phase separation similar to the bulk phase separation processes described in Sec. 1.3 [37]. The high annealing temperature in these studies suggests that phase separation is simply a result of bulk diffusion and that the reaction front is identical to that described by Cahn for spinodal decomposition; i.e. at the interface between the decomposing and homogenous alloy.

In the proceeding discussion, however, phase separation during PVD processes

were discussed in which the system kinetics determined the velocity of the reaction front between the homogenous alloy and the decomposed product [31]. Phase separation in thin films, however, differs from these well-established processes in that how fast species are being added to the growing material is externally imposed [28]. As such, the reaction front is externally determined by the deposition rate.

It has been shown that phase separation *during* thin film co-deposition results in a more diverse range of bicontinuous morphologies [38–41]. While the quantity of material is fixed for phase separation during post-deposition annealing, phase separation during film growth is accompanied by the continuous addition of randomly distributed atoms to the film surface throughout deposition [27].

The seminal theoretical work in this field of phase separation during thin film co-deposition was completed by Cantor and Cahn [42]. These authors described phase separation at low deposition temperatures and defined an interdiffusion distance for each constituent adatom. The distance or time that and adatom could diffuse before being buried into the bulk film is controlled via the deposition rate by the equation,

$$\bar{x} = \left(\frac{2\nu d}{\Gamma}\right)^{1/2} d \exp\left(\frac{-Q_s}{2k_b T}\right), \tag{1.2}$$

where ν is the vibrational frequency of surface adatoms, d the jump distance, Γ the deposition rate, Q_s the activation energy for surface diffusion, and k_B Boltzmann's constant.

A model for phase separation during elevated temperature thin film co-deposition

at elevated temperature was first presented by Atzmon and colleagues in which they described a diffusion equation describing the decomposition during synthesis [28]. Their equation was similar to Eq. 1.2. This work assumes that the diffusion processes are limited to the surface where the deposition rate defines an upper limit to the time an adatom can diffuse on the surface before it is buried by the next layer of material. Therefore, the bulk of a growing film is a temporal history of the morphology. This assumption is referred to as the frozen bulk approximation by Atzmon *et. al.* [28].

The temporal evolution of the compositional field of a thin film growing in the $+z$ direction with velocity, ν, can be written as

$$\frac{\partial c}{\partial t} = \tilde{D}_s \nabla_s^2 c + \frac{\delta}{v}(c_0 - c), \tag{1.3}$$

where $\tilde{D}_s$ is the surface interdiffusion coefficient, $\nabla_s^2 = (\partial^2/\partial x^2 + \partial^2/\partial y^2)_{z=0}$, δ the thickness of the surface interdiffusion layer (of the order of the interatomic spacing), and c_0 the composition of the deposition flux. This equation was applied to a morphology consisting of cylindrical domains dispersed in a matrix of another phase. This idealized structure is presented as a cartoon in Fig. 1.6.

Solving Eq. 1.3 for the composition profiles inside and outside of the cylindrical α domains, Atzmon and coworkers found steady state (i.e. $\partial c/\partial t = 0$) solutions in

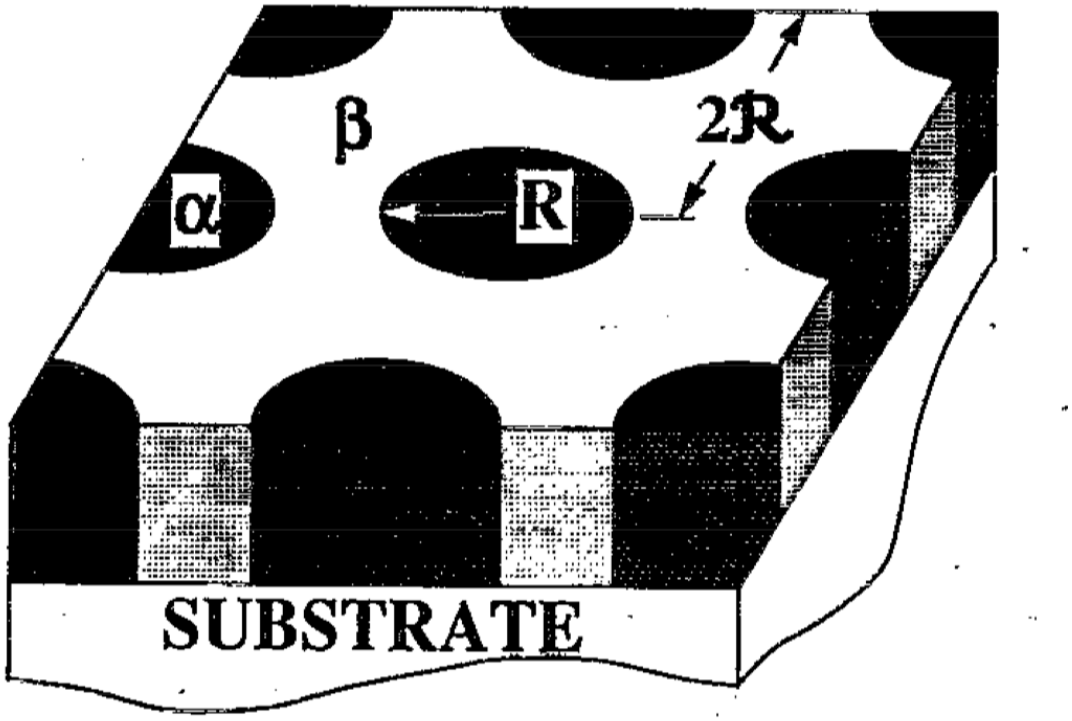

Figure 1.6: Cartoon schematic of laterally phase separated microsctructure used to develop surface interdiffersion theory for phase separation during thin film growth. From [27].

the form of

$$\begin{aligned} c^{\text{inside}}(r) &= A_1 K_0(r/\rho) + A_2 I_0(r/\rho) \\ c^{\text{outside}}(r) &= A_1 K_0(r/\rho) + A_2 I_0(r/\rho) \end{aligned}, \tag{1.4}$$

where $A_{1/2}$ are constants, K_0 and I_0 are modified Bessel functions of order 0 of the first and second kind, respectively, and ρ, the mean surface interdiffusion distance, is given by,

$$\rho = \sqrt{\frac{\tilde{D}_s \delta}{\nu}}, \tag{1.5}$$

where δ/ν is a measure of the time available for an adatom on the surface to diffuse before the film surface advances a distance of δ, and is buried by the next flux of material. It was concluded that the domain size of the cylinders, R, is proportional to the mean interdiffusion distance, ρ.

It can be reasoned from the previous discussion that the process of thin film phase separation is similar to that model presented by Cahn describing eutectoid decomposition. The main difference, however, is that in eutectoid decomposition the interface mobility and free energy change upon decomposition determines the velocity of the reaction rate. In thin film phase separation, the velocity of the reaction front is not determined by the system, but is instead controlled by the externally imposed deposition rate.

Eq. 1.5 shows that the domain size of the phase separated morphology is deter-

mined by the ratio of the surface interdiffusivity, $\tilde{D}_s$, and the deposition rate, ν. The only temperature dependence of this ratio is contained within the $\tilde{D}_s$ term. As such, raising the substrate temperature and lowering the deposition rate will theoretically have the same result on the steady state domain size [43].

The analytical model presented by Atzmon *et. al.* was supported empirically by the work done by Adams and coworkers [27, 39]. These authors co-deposited the immiscible Al-Ge system under a series of deposition temperatures and characterized the resultant morphologies. It was found that the domain structure evolved consistent with the surface interdiffusion model put forth by Atzmon and cowokers. As seen in Fig. 1.7, at low substrate temperatures, the low surface interdiffusion length led to lateral phase separation of Al- and Ge- rich domains with a domain size of approximately 100 nm. When increasing the surface interdiffusion distance by increasing the substrate temperature, the domain size increased significantly to approximately 1 micron in size.

Adams *et. al.* also noted that after a certain thickness of material was deposited, the morphology transitioned from a laterally separated structure like that presented in Fig. 1.6 to a transversely separated film with conentration modulations parallel to the thin film growth direction. The authors noted that this transition was a result of an increase in the Al-Ge interfacial energy to the total free energy of the system as the film thickened. At some film thickness (approximately 300 nm for the co-deposited Al-Ge system), it becomes energetically more favorable for the system to

form a flat interface normal to the film growth direction [43]. This transition depends on the ratio of the bilayer thickness and the domain size. It was concluded that the transverse phase separated film was possible from the beginning of the deposition as long as this ratio was sufficiently small [39].

The surface interdiffusion model provided by Atzmon and colleagues was further supported by more recent work on the immiscible Al-Si system completed by Fukutani *et. al.* [40]. These authors co-deposited the Al-Si system under a number of conditions including, substrate temperature, phase fraction, and deposition rate. Most notably, at increasing deposition rate, the domain size was refined as seen in Fig. 1.8. This domain refinement was also duplicated in the system when decreasing substrate temperature. Additionally, as the phase fraction of Al and Si became more disparate (e.g. $Al_{70}Si_{30}$), the morphology became more randomized and no longer an ideal laterally separated structure like that shown in Fig. 1.6.

Fukutani *et. al.* found good agreement with the frozen bulk approximation and surface interdiffusion model described by Atzmon *et. al.* [28]. Using a modified Cahn-Hilliard formulation, the authors completed a phase field simulation which temporally tracked the concentration of the system as the film was grown. As shown in Fig. 1.9, when the surface interdiffusion length was increased as a function of a non-dimensional deposition rate and temperature, the domain size was simulated to increase. These simulation results are consistent with the empirical results in the same work and that data presented by Atzmon *et. al.* [39].

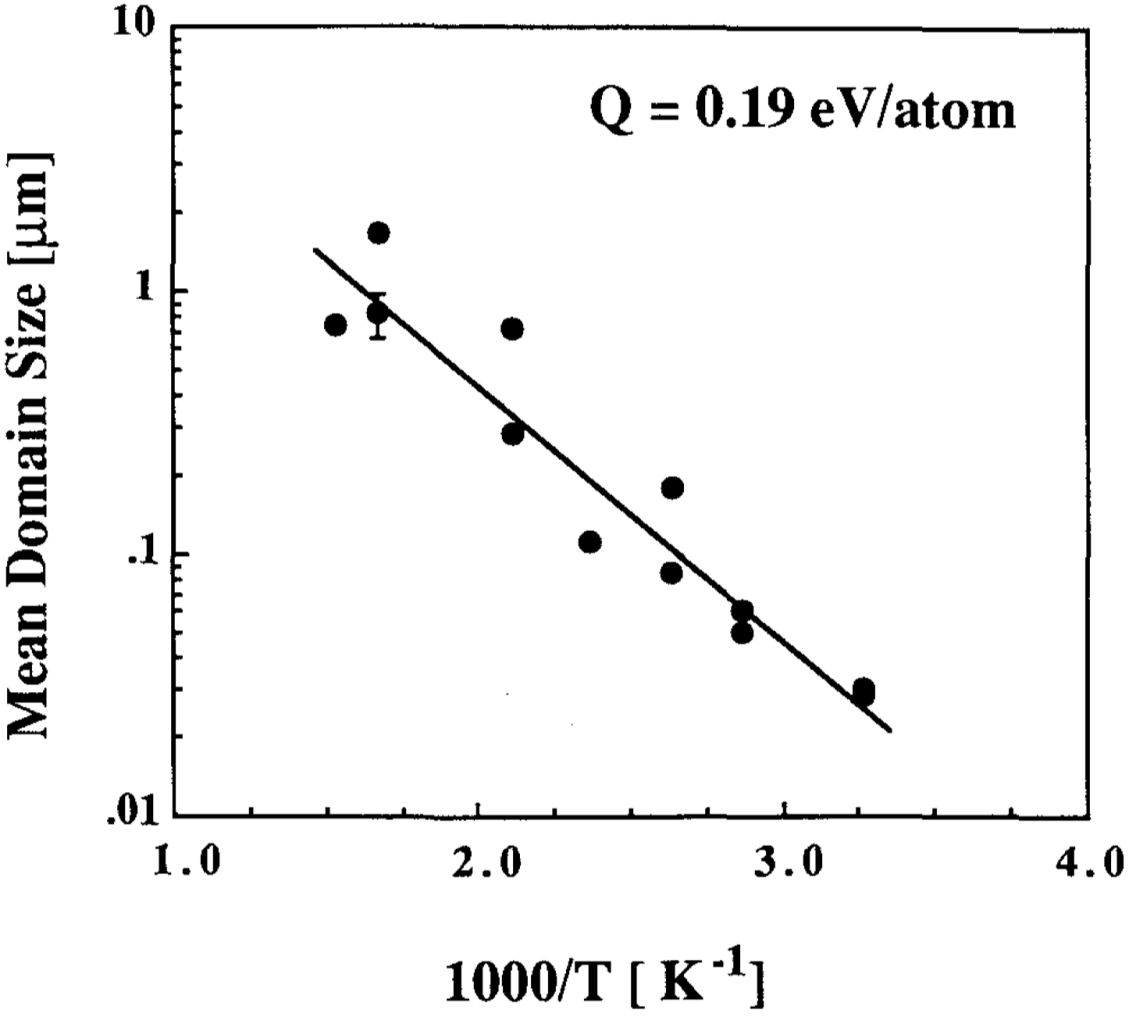

Figure 1.7: Arrhenius behavior of phase separated domains in Al/Ge thin films. It was observed that domain size increased as a function of substrate temperature. From [39].

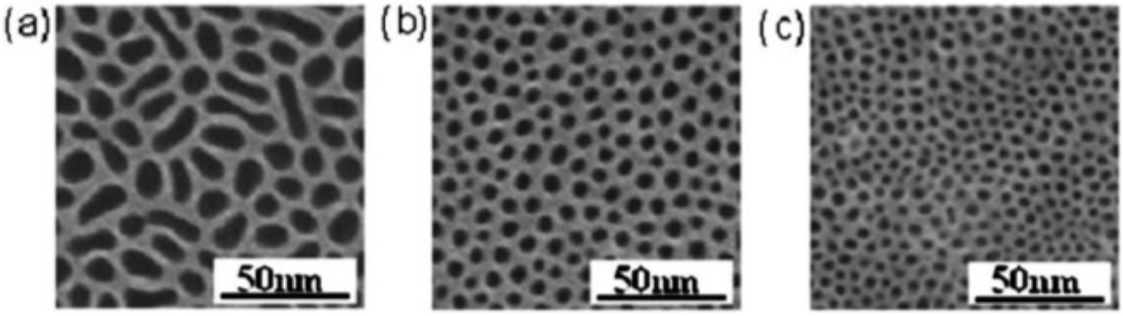

Figure 1.8: Domain refinement in a phase separated Al/Si co-deposited thin film as deposition rate increased. This figure shows SEM images of the the top surface at deposition rates of: (a) 7.5 nm/min, (b) 22.5 nm/min, (c) 46.1 nm/min. From [40].

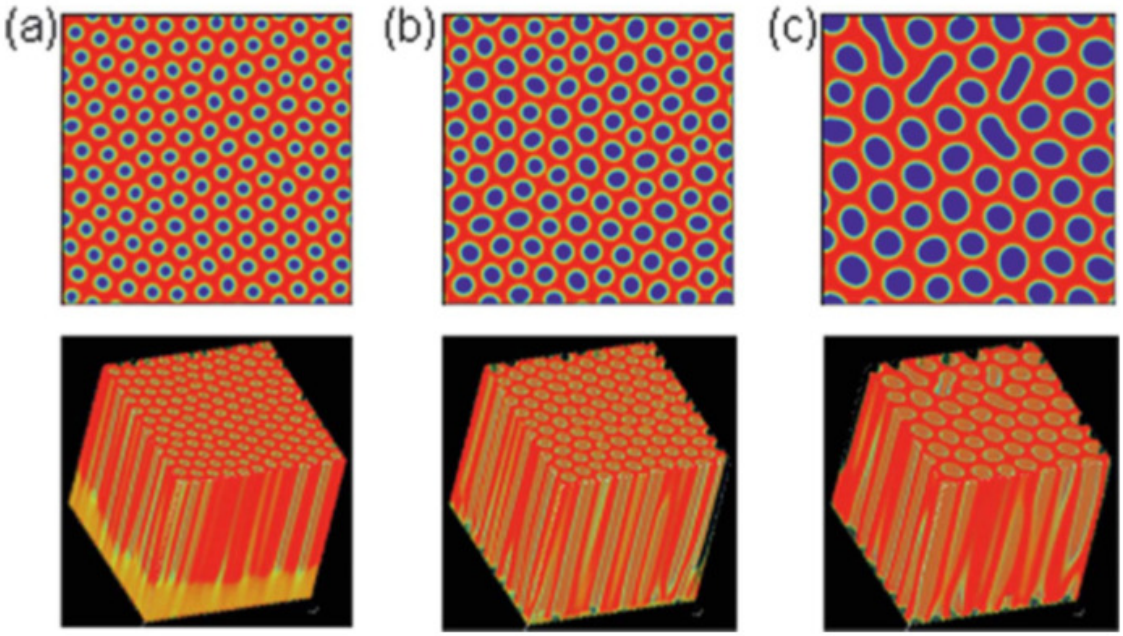

Figure 1.9: As the surface diffusion length (non-dimensionalized) increased from (a) $l_n = 1.0$ to (b) $l_n = 1.5$ to (c) $l_n = 2.5$ the phase separated domain size increased in this phase field simulation. From [40].

Uniquely, Fukutani *et. al.* observed that at the highest surface interdiffusion length simulated in their work, the lateral domains began to interconnect and the morphology was much more randomly oriented as seen in Fig. 1.9(c).

Simulation of phase separated thin films was further expanded upon by Yong *et. al.* whose work used a surface interdiffusion model to formulate a two-dimensional morphology map for binary, immiscible co-deposition [41]. In their work, Yong and coworkers considered an equiatomic A-B binary system with a miscibility gap. The phase field simulation modeled layer-by-layer growth of a film. Each layer would evolve through spinodal decomposition before the next layer would arrive. Deposition rate and phase fraction were the two parameters adjusted to map out resultant morphology.

The authors expanded upon the interdiffusion length model put forth by Atzmon et. al. [28]. They noted that the resultant morphology was a function of the ratio of the deposition rate and the rate of spinodal decomposition [41]. This ratio was modelled in the simulation by comparing the characteristic time for spinodal decomposition and the characterisitic time for deposition. The time needed to deposit a layer thickness of $\lambda_{\max}$ is $\lambda_{\max}/\nu$, where ν is the deposition rate. The time required to develop a concentration modulation with $\lambda_{\max}$ is proportional to $\lambda_{\max}^2/\tilde{D}$. The wavelength of spinodal decomposition that has the maximum growth rate is $\lambda_{\max} = 2\sqrt{2}\pi\sqrt{-\kappa/f''}$, where $\tilde{D}$ is the chemical diffusivity, κ is the gradient energy coefficient, and f'' is the second derivative of the local chemical free

energy, which Yong and coworkers approximated by a double well function (e.g. $f(c) = f_0 c^2(1-c)^2$). Note that $\tilde{D}$ is equivalent to $\tilde{D}_s$ and $\lambda_{\max}$ is equivalent to δ in the Atzmon *et. al.* model [28].

Yong *et. al.* used a ratio between two characteristic (spinodal decomposition and deposition) times to define a normalized deposition rate [41]:

$$\nu^N = \nu/(\tilde{D}/\lambda_{\max}). \tag{1.6}$$

It should be recognized that this equation is a convenient way of describing the competition between phase separation and the deposition rate during thin film growth of immiscible co-deposition. This is largely similar, but inverse, to the equation for surface interdiffusion described by Atzmon *et. al.* [28]. Yong *et. al.* used this parameter as the horizontal axis to form a morphology map for phase separated thin film morphologies as shown in Fig. 1.10 [41].

The study benefited the understanding of phase separated thin films as their morphology map simulated the conditions required to obtain a sample comprised entirely of vertical concentration modulations much like the transverse phase separation noted by Adams *et. al.* [39]. This vertical concentration modulation (VCM) sample was observed to exist at relatively high normalized deposition rates. High normalized deposition rate can be a result of decreasing the process temperature or increase the deposition rate. Like the work done by Adams *et. al.* and Fukutani *et. al.*, Yong and coworkers predicted the formation of lateral concentration modulations

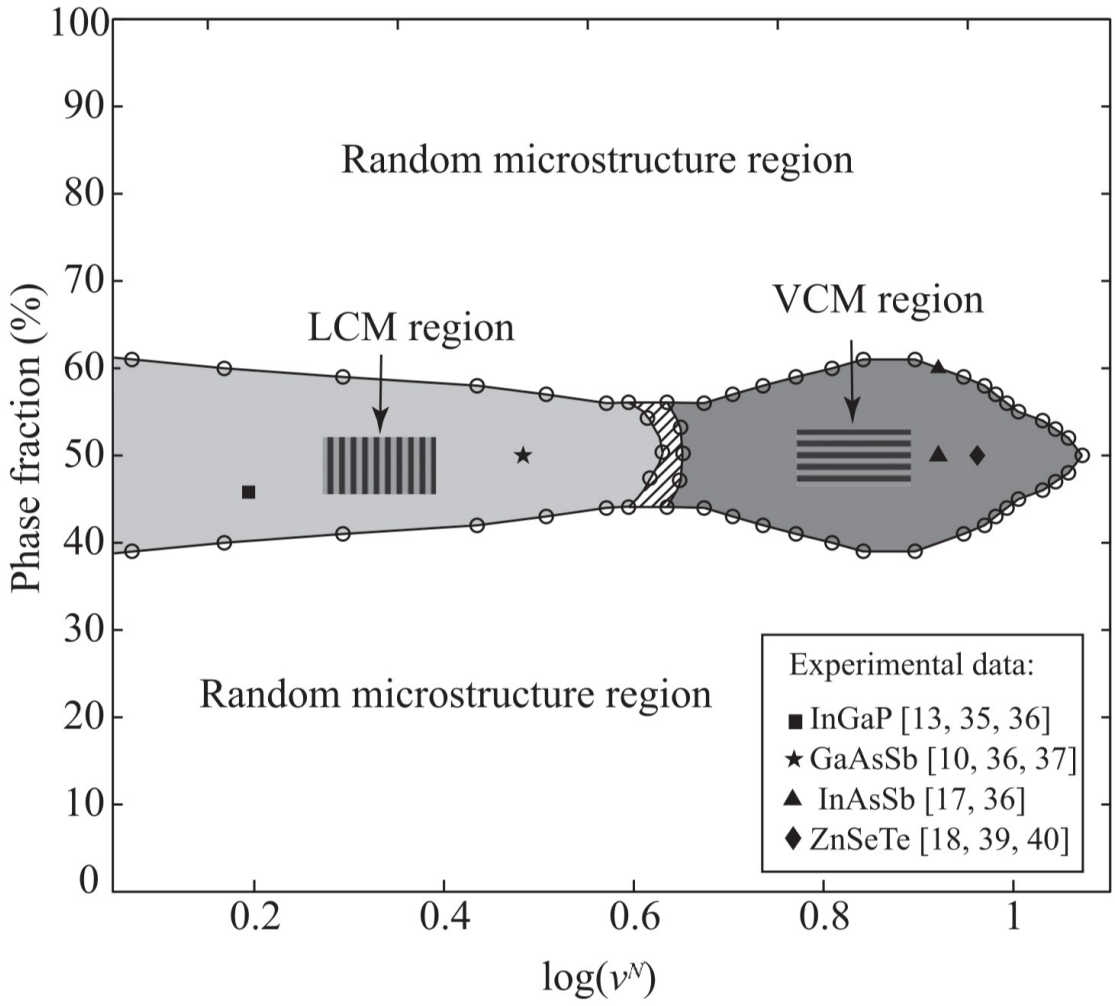

Figure 1.10: Microstructure map for morphological patterns showing dependence of concentration modulations on phase fraction and normalized deposition rate (see text for definition). The open circles are the simulation results and the various solid symbols are from experimental results. From [41] and references therin.

at relatively low normalized deposition rates [27, 40].

1.5 Relevance to the Present Work

The complex, phase-ordering kinetics that drive phase separation in thin film synthesis leads to the development of interesting self-assembled morphologies. This will be the focus of this dissertation.

Microstructual development in single phase thin film has been studied extensively and is largely understood. Structural zone diagrams can be used to guide deposition parameters required to obtain certain film microstructures. While extensive research has started to understand a similar controllability over phase separating thin films, much work is needed. The research literature in this field has elucidated that a competition between the rate of phase separation and the deposition rate is the governing factor over phase separated thin film morphologies. This competition is determined largely by the process temperature and the deposition rate. While individual works have shown *one* of the morphologies predicted by the models, most were not systematic studies on the effect of deposition conditions on the phase separation and able to show the existence of multiple morphologies.

In this dissertation, the results of such a systematic experimental and simulation based study are presented in the subsequent chapters. Experimental observations of phase separation in co-sputtered Cu-Mo and other FCC-BCC thin films is used to test the validity of the surface interdiffusion models aforementioned. The results presented in this work show that they are indeed consistent.

A novel hetergeneous process with many length scales of phase separation process is also described in this work. We reason this heterogeneous phase separation process by accounting for the mobility differences between the constituent species.

Finally, all of these microstructures are tested under mechanical load and irradiation. The unique bicontinuous interfaces contained in these microstructures proved to be mechanically strong and improve the ductility of the material. These same 3D interfaces also exhibited unique He retention behavior.

References

[1] H. Pulker. *Coatings on Glass*, volume 20. Elsevier, 1999.

[2] M.S. Rogers and M.M. Giachino.

[3] H. Tsai and D.B. Bogy. Characterization of diamondlike carbon films and their application as overcoats on thin-film media for magnetic recording. *Journal of Vacuum Science & Technology A: Vacuum, Surfaces, and Films*, 5(6):3287–3312, 1987.

[4] M. Ohring. *Materials Science of Thin Films*. Elsevier, 2001.

[5] N.J. Petch. The cleavage strength of polycrystals. *Journal of the Iron and Steel Institute*, 174:25–28, 1953.

[6] E.O. Hall. The deformation and ageing of mild steel: Iii discussion of results. *Proceedings of the Physical Society. Section B*, 64(9):747, 1951.

[7] N. Hansen. Hall–petch relation and boundary strengthening. *Scripta Materialia*, 51(8):801–806, 2004.

[8] C.A. Schuh, T.G. Nieh, and T. Yamasaki. Hall–petch breakdown manifested in abrasive wear resistance of nanocrystalline nickel. *Scripta Materialia*, 46(10):735–740, 2002.

[9] W.D. Nix. Mechanical properties of thin films. *Metallurgical Transactions A*, 20(11):2217, 1989.

[10] Y. Kang and P.S. Ho. Thickness dependent mechanical behavior of submicron aluminum films. *Journal of Electronic Materials*, 26(7):805–813, 1997.

[11] B.M. Clemens, H. Kung, and S.A. Barnett. Structure and strength of multilayers. *Mrs Bulletin*, 24(2):20–26, 1999.

[12] J.S. Koehler. Attempt to design a strong solid. *Physical Review B*, 2(2):547, 1970.

[13] A. Misra, J.P. Hirth, and R.G. Hoagland. Length-scale-dependent deformation mechanisms in incoherent metallic multilayered composites. *Acta Materialia*, 53(18):4817–4824, 2005.

[14] N.A. Mara, D. Bhattacharyya, P. Dickerson, R.G. Hoagland, and A. Misra. Deformability of ultrahigh strength 5 nm cu/ nb nanolayered composites. *Applied Physics Letters*, 92(23):231901, 2008.

[15] Y-C Wang, A. Misra, and R.G. Hoagland. Fatigue properties of nanoscale cu/nb multilayers. *Scripta Materialia*, 54(9):1593–1598, 2006.

[16] W. Han, M.J. Demkowicz, N.A. Mara, E. Fu, S. Sinha, A.D. Rollett, J.S. Wang, Y.and Carpenter, I.J. Beyerlein, and A. Misra. Design of radiation tolerant materials via interface engineering. *Advanced Materials*, 25(48):6975–6979, 2013.

[17] N.A. Mara, D. Bhattacharyya, J.P. Hirth, P. Dickerson, and A. Misra. Mechanism for shear banding in nanolayered composites. *Applied Physics Letters*, 97(2):021909, 2010.

[18] C.C. Hays, C.P. Kim, and W.L. Johnson. Microstructure controlled shear band pattern formation and enhanced plasticity of bulk metallic glasses containing *in-situ* formed ductile phase dendrite dispersions. *Physical Review Letters*, 84(13):2901, 2000.

[19] K. Seshan. *Handbook of Thin Film Deposition Processes and Techniques*. William Andrew, 2001.

[20] B.A. Movchan and A.V. Demchishin. Structure and properties of thick condensates of nickel, titanium, tungsten, aluminum oxides, and zirconium dioxide in vacuum. *Fiz. Metal. Metalloved.*, 1969.

[21] A. Anders. A structure zone diagram including plasma-based deposition and ion etching. *Thin Solid Films*, 518(15):4087–4090, 2010.

[22] K. Müller. Dependence of thin-film microstructure on deposition rate by means of a computer simulation. *Journal of Applied Physics*, 58(7):2573–2576, 1985.

[23] D.J. Srolovitz, A. Mazor, and B.G. Bukiet. Analytical and numerical modeling of columnar evolution in thin films. *Journal of Vacuum Science & Technology A: Vacuum, Surfaces, and Films*, 6(4):2371–2380, 1988.

[24] J.A. Thornton. Influence of substrate temperature and deposition rate on structure of thick sputtered cu coatings. *Journal of Vacuum Science and Technology*, 12(4):830–835, 1975.

[25] D. Depla and S. Mahieu. *Reactive Sputter Deposition*, volume 109. Springer, 2008.

[26] C.R.M. Grovenor, H.T.G. Hentzell, and D.A. Smith. The development of grain structure during growth of metallic films. *Acta Metallurgica*, 32(5):773–781, 1984.

[27] Christopher D Adams. *Phase Separation During Thin Film Co-Deposition*. PhD thesis, University of Michigan, 1992.

[28] M. Atzmon, D.A. Kessler, and D.J. Srolovitz. Phase separation during film growth. *Journal of Applied Physics*, 72(2):442–446, 1992.

[29] M. Powers, B. Derby, A. Shaw, E. Raeker, and A. Misra. Microstructural characterization of phase separated co-deposited cu-ta immiscible alloy thin films. *Thin Solid Films*, 2020.

[30] R. DeHoff. *Thermodynamics in Materials Science*. CRC Press, 2006.

[31] J. W. Cahn. On spinodal decomposition. *Acta Metallurgica*, 9(9):795 – 801, 1961.

[32] J.W. Cahn. The kinetics of cellular segregation reactions. *Acta Metallurgica*, 7(1):18–28, 1959.

[33] M.K. Miller, J.M. Hyde, M.G. Hetherington, A. Cerezo, G.D.W. Smith, and C.M. Elliott. Spinodal decomposition in fe-cr alloys: Experimental study at the atomic level and comparison with computer modelsi. introduction and methodology. *Acta Metallurgica et Materialia*, 43(9):3385–3401, 1995.

[34] A. Lahav, M. Eizenberg, and Y. Komem. Phase separation in reactions of ni-ta thin films with gaas. *Journal of Applied Physics*, 62(5):1768–1777, 1987.

[35] S.Q. Wang, L.S. Hung, and J.W. Mayer. Reactions of co/mo bilayers and amorphous co50mo50 alloy films with silicon substrates. *Thin Solid Films*, 162:199–207, 1988.

[36] Y.K. Kim, D.A. Baugh, D.K. Shuh, R.S. Williams, L.P. Sadwick, and K.L. Wang. Structural and chemical stability of thin films of pt–ga intermetallic compounds of gaas (001). *Journal of Materials Research*, 5(10):2139–2151, 1990.

[37] C.M. Müller, A.S. Sologubenko, S.S.A Gerstl, and R. Spolenak. On spinodal decomposition in cu–34 at.% ta thin films–an atom probe tomography and transmission electron microscopy study. *Acta Materialia*, 89:181–192, 2015.

[38] C.D. Adams, M. Atzmon, Y-T Cheng, and D.J. Srolovitz. Transition from lateral to transverse phase separation during film co-deposition. *Applied Physics Letters*, 59(20):2535–2537, 1991.

[39] CD Adams, Michael Atzmon, YT Cheng, and DJ Srolovitz. Phase separation during co-deposition of al-ge thin films. *Journal of Materials Research*, 7(3):653–666, 1992.

[40] K. Fukutani, K. Tanji, T. Saito, and T. Den. Phase-separated al–si thin films. *Journal of Applied Physics*, 98(3):033507, 2005.

[41] Y. Lu, C. Wang, Y. Gao, R. Shi, X. Liu, and Y. Wang. Microstructure map for self-organized phase separation during film deposition. *Physical Review Letters*, 109(8):086101, 2012.

[42] B. Cantor and R.W. Cahn. Metastable alloy phases by co-sputtering. *Acta Metallurgica*, 24(9):845 – 852, 1976.

[43] C. D. Adams, D. J. Srolovitz, and M. Atzmon. Monte carlo simulation of phase separation during thinfilm co–deposition. *Journal of Applied Physics*, 74(3):1707–1715, 1993.

CHAPTER II

Experimental and Simulation Methods

This chapter is divided into three sections. The first details the experimental methodology of co-depositing model face-centered cubic (FCC) and body-centered cubic (BCC) immiscible thin film combinations at elevated temperature. The second section details a novel technique for depositing phase separated thin films known as High Powered Impulse Magnetron Sputtering (HiPIMS). Next, the associated characterization methods of these phase separation morphologies are detailed. This is followed by a description of the mechanical and irradiation testing that was completed on these bicontinuous, phase separated films. Finally, a brief explanation of the phase field simulation used to predict these phase separated morphologies in three dimensions is included.

2.1 Binary FCC/BCC Thin Film Synthesis using DC Magnetron Sputtering

Model systems comprised of Cu-X (where X is a body centered cubic (BCC) group V or VI transition metal) alloys are ideal to synthesize bicontinuous interfaces. Each

combination is nearly completely immscible [1] across a wide composition and temperature range. If the right kinetic conditions exist, self-assembly of phase separated regions of pure face-centered cubic (FCC) and BCC phases will result.

In the previous chapter, a hypothesis concerning how to deposit and develop predictive capability over phase separating thin films was outlined. We hypothesized that depositing immiscible species at changing deposition conditions would result in changes to the direction of phase separation. To test this hypothesis introduced in the previous chapter, FCC-BCC thin films with a nominal composition of 45 at.% Cu were co-deposited onto oxidized Si substrates by DC magnetron sputtering [2]. Nominally equi-atomic composition was chosen to create bicontinuous morphologies of separating phases and avoid discrete particle formation of a minority phase. The starting materials were at least 99.95% pure. Base pressure in the chamber prior to deposition was less than 2.7×10^{-5} Pa. Ar was used as the process gas and was maintained at a pressure of 0.4 Pa during deposition. Two-inch diameter targets oriented confocally above a rotating substrate with governable DC power to control the deposition rate were used for the depositions. Films approximately 1000 nanometers thick were deposited at substrate temperatures between 400 °C and 800 °C to induce phase separation during deposition. Substrate temperature was monitored with a thermocouple between the substrate and the substrate heater. A schematic of the physical vapor deposition chamber is shown in Fig. 2.1.

Substrate temperature remained constant throughout the deposition. The nom-

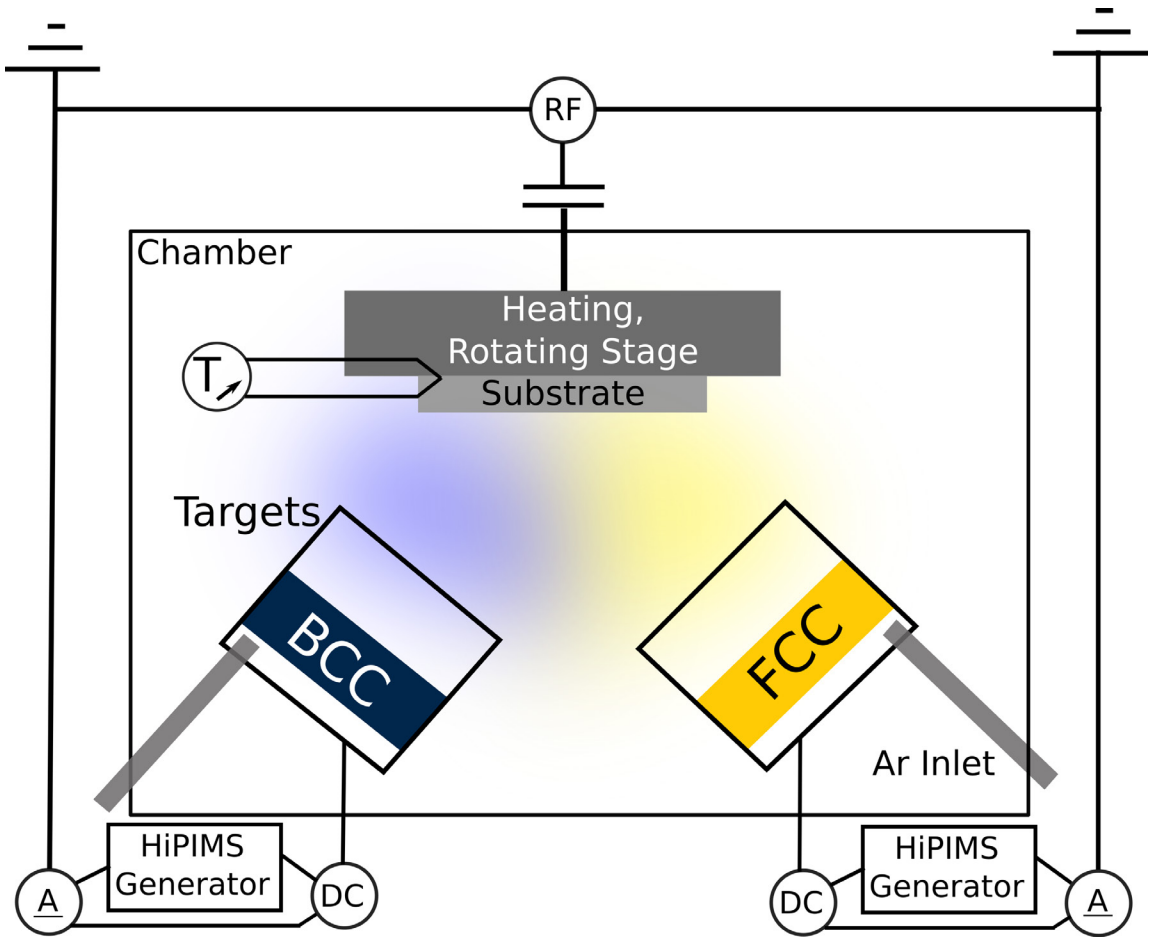

Figure 2.1: A schematic drawing of the PVD sputtering equipment used in this work with a general FCC/BCC metal target combination. From [2].

inal Cu and Mo deposition rate was held at 0.06, 0.41, and 0.70 nanometers per second for each constituent for a total deposition time of 5060, 1230, and 715 seconds, respectively. A matrix of the samples deposited is shown in Table 2.1.

2.1.1 Novel Ternary FCC/BCC Thin Film Co-Deposition

All of the previous work in this field of phase separating films have focused on immiscible binary systems. At the end of this dissertation, we present preliminary results on the co-deposition of three mutually immiscible elements: Cu, Mo, and Ag. This system was deposited at the the three deposition temperatures listed in Table 2.1 and at total deposition rate of 2.1 nanometers/second.The work on this system will continue in future studies.

2.2 Cu-Fe Co-sputtering at Elevated Temperature Using High Power Impulse Magnetron Sputtering

High-power impulse magnetron sputtering (HiPIMS), a relatively new introduction to the sputtering community, is an energetic deposition technique during which a highly ionized flux condenses on the substrate surface [3].

High power densities during HiPIMS ionizes the target material in the plasma. These ionized metallic species are highly energetic and induce ion etching during sputtering [4]. The benefit of using of metal ions instead of process gas ions used in radio frequency (RF) biasing of the substrate, is that metal inclusions do not lead to detrimental gaseous voids, which are composed of trapped process gas species [5].

While the HiPIMS technique has been extensively studied for single phase mate-

	Deposition Temperature (°C)		
Total Deposition Rate (nm/s)	400	600	800
0.12	X	X	X
0.82	X	X	X
1.4	X	X	X

Table 2.1: Matrix of the film substrate temperatures and deposition rates. An X marks samples that are shown in this work. From [2].

rials, a fundamental understanding of how adding kinetic energy through HiPIMS to co-sputtered immiscible metals such as Cu and Fe influences the phase separated morphology remains outstanding. It is hypothesized that the added energy supplied by HiPIMS will result in nanoscale morphology changes when compared to depositing the same system using DC magnetron sputtering (DCMS). In this work, we test this hypothesis by co-depositing a Cu-Fe model system under a specific set of deposition conditions. We then apply the same deposition conditions to the Cu-Fe system but instead use a HiPIMS power supply and compare the resultant morphologies.

Table 2.2 shows the four samples studied in this work. Cu-Fe thin films with a nominal equal atomic fraction of each constituent were deposited using both DC magnetron sputtering (DCMS) and high-power impulse magnetron sputtering (HiPIMS). Figure 2.2 shows the setup of the physical vapor deposition chamber used. To isolate the effects of HiPIMS on the resultant morphology no RF bias was applied to the deposited films. Future experiment will include the effect of RF bias on the film microstructure.

The starting materials were 99.999% pure Cu and 99.99% pure Fe. Nominally equiatomic composition was chosen to create bicontinuous morphologies of separating phases and avoid discrete particle formation of a minority phase. Base pressure prior to deposition was less than 3.06×10^{-6} Pa. 2-inch targets oriented confocally above a rotating substrate with governable DC power to control the deposition rate were used for the depositions. Films approximately 1000 nm thick were deposited at

Table 2.2: Table of deposition conditions for the Cu-Fe HiPIMS study.

Sputtering Method	Substrate Temperature [°C]	Ion Current [Amps]		Deposition Rate [Ang./s]		Phase Fraction [at.%]	
		Fe	Cu	Fe	Cu	Fe	Cu
DCMS	300	–	–	2.4 ± 0.1	2.4 ± 0.1	49.5 ± 2.2	50.5 ± 2.2
HiPIMS	300	1	0.1	1.8 ± 0.1	1.7 ± 0.1	50.4 ± 2.5	49.6 ± 2.5
HiPIMS	300	5	2	1.5 ± 0.2	2.1 ± 0.2	42.5 ± 3.1	57.5 ± 3.1
HiPIMS	300	18	2	1.2 ± 0.1	1.5 ± 0.1	44.3 ± 1.8	55.7 ± 1.8

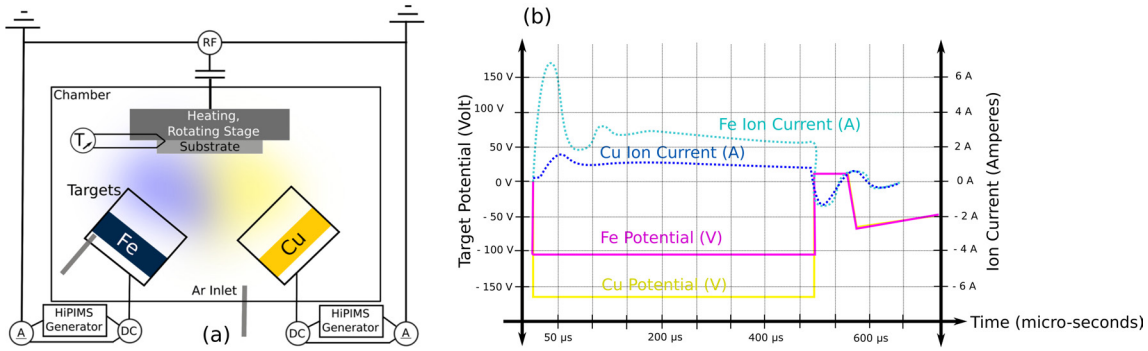

Figure 2.2: (a) Deposition system schematic including the HiPIMS generator that can pulse power at high potential and current (i.e. high power) for short time durations on the order of hundreds of micro-seconds on a maximum of two targets. While our chamber is capable of RF bias, no bias was used for this experiment to isolate the effects of HiPIMS on the phase separated morphology. (b) Ammeters inside the HiPIMS unit allow for the measurement of metal ion current as a function of time for two materials.

a substrate temperature of 300 °C to induce phase separation during deposition. Substrate temperature was monitored with a thermocouple between the substrate and the substrate heater. Substrate temperature remained constant throughout the deposition. The nominal Cu and Fe deposition rates for each sample are listed in Table 2.2. Deposition rates tend to be lower while using HiPIMS due to two factors: the increased gas pressure (approximately 2 Pa) needed to maintain a plasma in HiPIMS and the higher return probability of the sputtered positive ions back towards the target cathode. Gas pressure for DCMS was kept stable at 0.4 Pa and 2 Pa for HiPIMS. The target-to-substrate distance was measured to be 5.0 inches.

The variable of interest in this study is the ion current provided by the HiPIMS technique. Pulse width, pulse frequency, DC power, and gas pressure determine the number of ionized species (i.e. current) during HiPIMS. These factors were all governable with the Kurt J. Lesker Company / Starfire Industries HIPIMS IMPULSE supply used in this study. These parameters were adjusted to obtain a steady current for the Fe and Cu target during deposition. Ammeters in the HiPIMS unit allow for current to be measured at the substrate during deposition. The current and potential waveform was observed using a oscilliscope during deposition. An example of the waveform can be seen in Fig. 2.2b. The HiPIMS unit connected to the Cu target was slaved to the HiPIMS unit pulse connected to the Fe such that material was deposited at the same time. As such, pulse frequency and width were the same for the Fe and Cu target. The currents during deposition for each target are listed

in Table 2.2.

2.3 Characterization

Chemical and microstructural characterization was used to link the deposition conditions to the final film morphology.

2.3.1 Microstructural Characterization - X-Ray Diffraction

X-ray diffraction measurements were made on a Rigaku Ultima III diffractometer that uses fine-line sealed Cu tube Kα ($\lambda = 1.5406$) X-rays with a one-dimensional D/teX Ultra detector that provides up to 100$\times$ the intensity gain compared to conventional 0D scintillation counters [2]. The generator is a D/MAX Ultima series with a maximum power of 3 kW. The samples were mounted on a thin-film stage that was aligned for maximum sample height and X-ray intensity. Data were collected in continuous scan mode in parallel beam slit geometry over the 2-theta range from 30° to 90° with a step size of 0.0167° and a scanning speed of 1.5 °/min. The Divergence slit was set to (1/4)°, the Divergence H.L. Slit 4 was set at 10 mm, and the Scattering and Receiving Slits were set to open. All data are shown unprocessed as no background subtraction or Kα_2 elimination was carried out.

2.3.2 Microstructural Characterization - Scanning Transmission Electron Microscopy

Scanning/transmission electron microscopy (S/TEM) foils were prepared using a focused ion beam (FIB) technique in an FEI Helios 650 nanolab SEM/FIB. The foils were attached and thinned on a silicon TEM half grid to prevent any compositional

background from the TEM grid. Samples were plasma cleaned for 300s prior to insertion into the S/TEM. A JEOL 3100R05 double-Cs corrected S/STEM with a point-to-point resolution of 0.055 nm was used to collect HAADF images of the samples. The convergent angle for all image collection was set to 111 degrees at a camera length of 8 centimeters for true HAADF imaging. Compositional maps were collected using a JEOL SDD X-ray detector with an active area of 60 mm^2 capable of detecting elements with $Z > 5$ [6].

2.4 Testing Bicontinuous Films in Extreme Environments

2.4.1 Mechanical Behavior Testing

A diamond Berkovich tip was used to make indentations to a depth of 150nanometers. The average value from 25 indents was reported. Hysitron PI 85 and PI 95 Picoindenters were used as platforms to conduct nanopillar compression tests in the SEM and TEM respectively. The compression tests were performed using diamond flat-punch indenters in displacement control mode to maintain a fixed strain rate of $2 \times 10^3/s$. The TEM and nanopillar samples were prepared using focused ion beam (FIB) in FEI Helios Nanolab DualBeam SEM. To minimize FIB damage, the final beam current was 50pA. At this current, minimal surface amorphization was detected in the TEM foils fabricated by FIB. Ion softening of the nanopillars was thus considered negligible in our study. During nanopillar fabrication process, the final thinning step was done within 300milliseconds to reduce 20nanometers of the pillar diameter, minimizing the taper angle of the pillar to 2.2°. This small extent of

tapering in inevitable in nanopillars fabricated by FIB and generally not considered a problem for crystalline materials. Strain hardening would offset the effect of tapering that causes higher stress state at the top of the pillar. For each nanocomposite, at least four pillar compression tests were performed to ensure the reproducibility of the data.

2.4.2 Irradiation Testing

To understand the morphology of He precipitates in these metal composites with domains bounded by heterophase interfaces, we introduced He into these samples using an isotope ^{3}He+ ion beam implantation perpendicular to the sample surface [2]. These implantation experiments were completed with the help of Dr. Yong Wang at the Center for Integrated Nanotechnologies at the Los Alamos National Laboratory. The selected beam energy (20 keV) yields a peak implanted He concentration centered just below the surface of each film as determined by a Stopping and Range of Ions in Matter (SRIM) calculation. The ^{3}He+ isotope was chosen so its retention in the sample can be sensitively measured by detecting high energy protons from a deuterium induced nuclear reaction analysis (NRA), ^{3}He(d,p)^4 He [7]. The implantation was conducted at 250 °C to accelerate the nucleation and growth of He precipitates. The temperature was measured using a thermocouple underneath the sample holder. To isolate the He retention as a function of fluence, four different fluences ^{3}He implantation fluences were performed: 3.0×10^{15}, 7.0×10^{15}, 1.5×10^{16}, and 3.010^{16} ions/cm^2. A fluence of 1.0×10^{17} ions/cm^2 using a 20 keV ^{4}He+ beam was also

used at 250 °C in order to study microstructure evolution and the nanomechanical properties of these nanocomposites at higher damage conditions.

Following implantation of all samples, NRA was completed to determine the He retention in each of the three morphologies for every fluence. The energy of 475 keV for the 2D+ beam was chosen so the reaction ^{3}He(d,p)^{4} He has an optimal sensitivity to detect the implanted ^{3}He atoms at the most probable depth as predicted by SRIM.

We conducted a SRIM [8] simulation to determine the implantation yield as a function of sample thickness. The simulated profile is shown in Fig. 2.3 in the Supplementary material. The simulated material was a 45 at.% Cu (55 at.% Mo) sample with a thickness of 1000 nanometers and a density of 9.7 g/cm3 (an average of the Cu and Mo densities). The implantation profile shows that the greatest concentration of He ions were present at approximately 80 nm below the film surface. The profile shows that an insignificant number of He atoms are close enough to the surface to escape before becoming trapped at defects in the material. The diffusion coefficient was not determined.

The homologous temperature during implantation for each constituent was: $(\mathrm{T}_H)_{\mathrm{Cu,He}} = 0.38$; $(\mathrm{T}_H)_{\mathrm{Mo,He}} = 0.18$. At this temperature, He atoms diffuse on interstitial sites until they are trapped by a defect in this structure [9].

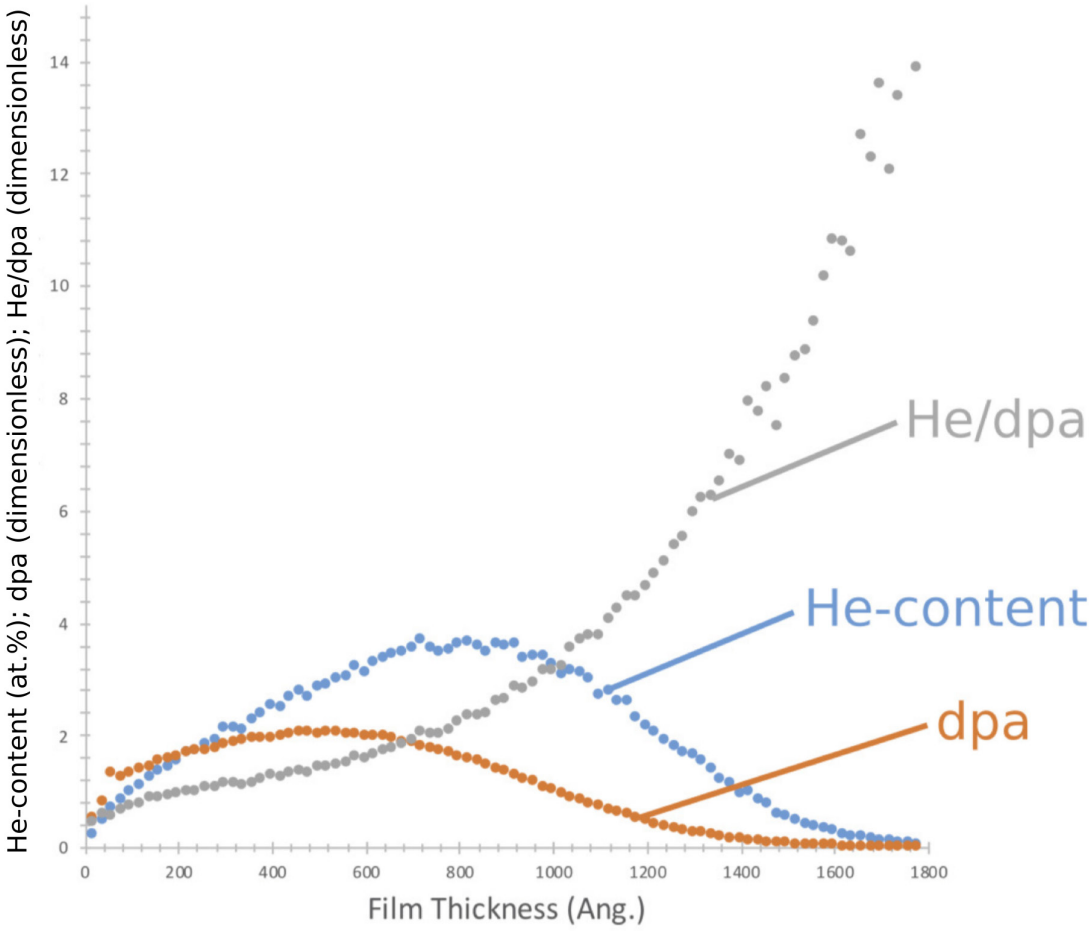

Figure 2.3: A SRIM calculated implantation yield versus film thickness implantation profile. The greatest concentration of He ions was centered at a thickness of approximately 80 nm below the film surface. dpa stands for displacements per atom. From [12].

2.5 Simulation Model

2.5.1 Phase Field Model in Three Dimensions to Simulate Phase Separated Morphologies

Previous phase field models have been limited to two dimensions. To fully capture the synthesis physics of phase separation during thin film growth, we extended a phase field model into the third dimensions. The following methodology is from the following reference: [10]. For our simulations, we use a similar Cahn-Hilliard model as was previously described by Lu *et al.* except that implemented in three-dimensions [11]. The total free energy of the system, F, is expressed as

$$\frac{F}{k_B T} = \int_V \left\{ \underbrace{\psi^2(1-\psi)^2}_{F_{\text{bulk}}} + \underbrace{\frac{\kappa}{2}|\nabla\psi|^2}_{F_{\text{interface}}} \right\} dV, \tag{2.1}$$

where $\psi(r,t)$ is an order parameter that denotes the local concentration difference between the two components, $\psi_A - \psi_B$. F_{bulk} represents the bulk-free energy that accounts for two stable phases $\psi = \{0,1\}$ below the critical point, and T is the deposition temperature. κ is the gradient energy coefficient that penalizes gradients in the order parameter.

The kinetic evolution of the conserved order parameter ψ follows Cahn-Hilliard dynamics,

$$\frac{\partial\psi}{\partial t} = \nabla \cdot M\nabla\mu, \tag{2.2}$$

where M is mobility and μ is the chemical potential,

$$\mu = \frac{\delta F}{\delta \psi}. \tag{2.3}$$

We nondimensionalize the model parameters described above by selecting characteristic energy scale $F' = k_B T$, length scale $L' = \Delta x$, and time $t' = L'^2/M$. Here, Δx is the spacing between integration grid points.

We use a three-dimensional simulation domain with a maximum of $300 \times 300 \times 300$ integration points. Periodic boundary conditions are applied along x- and y-axes. Since the Cahn-Hilliard equation is 4th order, two boundary conditions are required along the surfaces perpendicular to the z-axis. The conditions we use impose zero flux in the order parameter through these surfaces as well as 90° contact angles in the z-axis. Contact angles are the resultant of surface tension balance at the triple junction of an interface between two phases and the free surfaces of those phases. Therefore, this force balance may be accounted for in phase-field simulations using an appropriate Neumann-type boundary condition, as described in [13]

We solve Eq. 2.3 using an explicit finite-difference method, where the spatial derivatives are discretized using the central difference. This method is second-order accurate in space. Temporal discretization is implemented using the first-order Euler technique. The deposition is simulated by adding a layer of integration points with uniform initial composition $\psi_0 = 0.5$ on top of the pre-existing simulation domain, as shown in Fig. 2.4.

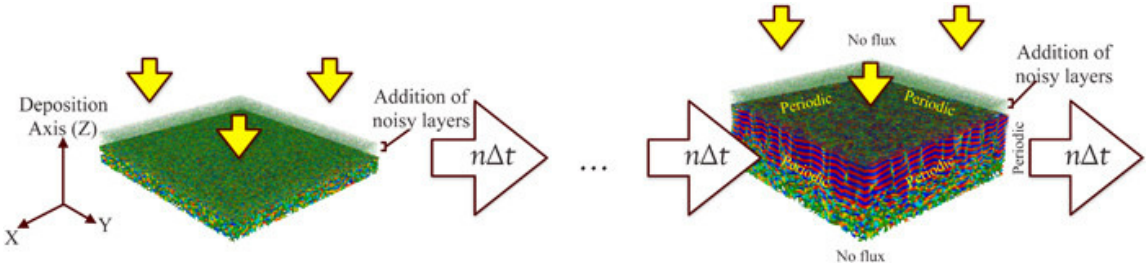

Figure 2.4: Schematic diagram illustrating how vapor deposition is incorporated into the phase-field model. From [10].

The thickness of this layer equals one grid point (Δx) and is kept fixed, while the time interval $n\Delta t$ between successive depositions is adjusted to obtain the desired deposition rate, $R = \Delta x = n\delta t$. Here, Δt is the dimensionless time step for numerical integration and n is the number of time steps between the deposition of consecutive layers. Concentration fluctuations in the freshly deposited layers are incorporated via a Langevin noise term. These composition fluctuations provide a perturbation to the initial composition, which (at 50 at.% Cu and 50 at.% Mo) would otherwise correspond to an equilibrium point (albeit an unstable one) in our model. No modification to the field equation [Eq. 2.2] is needed to incorporate these fluctuations into our simulations. Moreover, there is no systematic effect of the random number generator seed on the morphological evolution of the deposited layers.

The simulation starts with a film thickness of $z = 2\Delta x$ and ends with a film thickness of $z = 300\Delta x$. In all the simulations, Δx and Δt are chosen to be 0.1 and 10^6, respectively. The dimensionless gradient energy coefficient is chosen to be 1.0. We performed simulations at nondimensional deposition rates of $0.05 \leq R \leq 1.0$ and mobilities of $0.01 \leq M \leq 1$. To inspect the internal structure of the models, we visualize isosurfaces with $\psi = 0.5$ representing interfaces between Cu- and Mo-rich domains. At any given location, the isosurfaces are colored by the value of the z-component of the unit vector that lies parallel to the gradient of the order parameter at that location. Thus, interfaces colored in red or blue in Fig. 2.4 are oriented perpendicular to the z-axis, while interfaces colored in green are parallel

to it. We studied how microstructure in the film changes with time by employing a time-dependent structure factor. We measured the average domain size, S, by calculating the inverse of the first moment, $k_1(t)$, which in turn is obtained from the structure factor, $s(k,t)$ as

$$k_1(t) = \frac{\sum_{\mathbf{k}} \mathbf{k}(t) s(\mathbf{k},t)}{\sum_{\mathbf{k}} s(\mathbf{k},\mathbf{t})}, \tag{2.4}$$

where $\mathbf{k}$ is the wave vector. Please note that $\mathbf{k}$ is not a basis vector in our analysis. It is a component of the Fourier expansion of the phase field. Since the phase field depends on time, so do all $\mathbf{k}$'s. Eq. 2.4 gives the expectation value of $\mathbf{k}$ weighted by the structure factor of the phase field (expressed as a function of $\mathbf{k}$). The average domain size, S, was then plotted as a function of film thickness, d, to obtain a profile of the domain size along the deposition axis. All the phase-field simulations reported in this work corresponds to PVD of film that has an equimolar composition of 50 at.% Cu and 50 at.% Mo. It should be noted that the phase-field simulations of PVD in this work do not explicitly account for the vapor phase or any influence it may have on the evolution of phase-separated domains.

We want to conclude this section by making special indication of how diffusion processes are being modeled. The phase field method inherently accounts for diffusion throughout the entire system, including bulk and interfaces, so our simulations naturally include both forms of transport. In reality, mobility values may differ depending on whether transport is through the bulk or through interfaces. Our sim-

ulations use a uniform mobility value regardless of transport mode. However, this may be easily modified in future simulations, if needed. Furthermore, in the Cahn-Hilliard equations used to model the morphological evolution, the atomic diffusion (coefficient given by D) is incorporated through the leading mobility term (M). By choosing various forms of M, one can model interfacial diffusion in addition to the one in bulk. See for example: Eq. 8 in [14]. M and D are related, see for example Eq. 2 in [15]. However, please note that this relation is valid only for an ideal solution, which Seol et al. might have ignored. For regular solutions, an additional term related to the logarithm of activity coefficient (gamma) should be multiplied to the atomic mobility.

Temperature dependence of mobility was not modeled in our simulations. That is because data on the temperature dependence of mobility in these systems is not currently available. Rather, we simply observe that increasing temperature results in higher mobilities and use that to make qualitative observations on the effect of higher mobility on microstructure morphology evolution.

2.5.2 Density Functional Theory to Measure Energetics of Pseudormorphic Phases

Density Functional Theory (DFT) was utilized to better understand the energetics of metastable phase formation in these novel heterogeneous morphologies presented in Chapter 4 [6]. The ATAT package [16] was used to explore the entire composition space, calculating the energies of formation for each configuration, relative to the pure end members, Cu and Mo (in the FCC or BCC states, respectively), through DFT

calculations using the VASP software package [17]. All configurations investigated were allowed to completely relax, i.e. volume, shape and atomic coordinates were all allowed to relax to the local equilibrium state. Cluster expansion (CE) was carried out until the error between the predicted energies of formation of arbitrary configurations and those calculated through the DFT code converged approximately within less than approximately 10 meV/spin.

This calculated error is the formation energy difference between cluster expansion (CE) and the formation energy calculated by DFT. These are two different things. CE is essentially bond-counting and provides a fast way of calculating formation energies without having to do DFT. However, it has many parameters, which need to be chosen by fitting to a database of atom clusters with known formation energies. These databases almost inevitably come from DFT. Here we are increasing the size of the DFT database and determining when the CE predicts energies that are within 10 meV/spin of the DFT values.

2.5.3 Author Contributions

Benjamin K. Derby conceived, planned, and carried out the experiments, including the all physical vapor deposition, X-ray diffraction, X-ray fluorescence spectroscopy, and electron microscopy. The physical vapor deposition was completed at the Center for Integrated Nanotechnologies at Los Alamos National Laboratory. The X-ray diffraction and X-ray fluorescence spectroscopy was completed at the University of Michigan Van Vlack Laboratory. The electron microscopy was completed at

the Michigan Center for Materials Characterization and the Center for Integrated Nanotechnologies at Los Alamos National Laboratory. Benjamin K. Derby carried out sample preparation for all experiments, interpreted the results, and took the lead in writing the published works.

References

[1] M. Powers, B. Derby, E. Raeker, and A. Champion, N.and Misra. Hillock formation in co-deposited thin films of immiscible metal alloy systems. *Thin Solid Films*, 693:137692, 2020.

[2] B. Derby, Y. Cui, J.K. Baldwin, and A. Misra. Effects of substrate temperature and deposition rate on the phase separated morphology of co-sputtered, cu-mo thin films. *Thin Solid Films*, 647:50–56, 2018.

[3] A. Anders. A structure zone diagram including plasma-based deposition and ion etching. *Thin Solid Films*, 518(15):4087–4090, 2010.

[4] J. Alami, J.T. Gudmundsson, J. Bohlmark, J. Birch, and U. Helmersson. Plasma dynamics in a highly ionized pulsed magnetron discharge. *Plasma Sources Science and Technology*, 14(3):525, 2005.

[5] D. Lundin and K. Sarakinos. An introduction to thin film processing using high-power impulse magnetron sputtering. *Journal of Materials Research*, 27(5):780–792, 2012.

[6] B. Derby, Y. Cui, J.K. Baldwin, R. Arróyave, M.J. Demkowicz, and A. Misra. Processing of novel pseudomorphic cu–mo hierarchies in thin films. *Materials Research Letters*, 7(1):1–11, 2019.

[7] V.K. Alimov, M. Mayer, and J. Roth. Differential cross-section of the d (3he, p) 4he nuclear reaction and depth profiling of deuterium up to large depths. *Nuclear Instruments and Methods in Physics Research Section B: Beam Interactions with Materials and Atoms*, 234(3):169–175, 2005.

[8] J.F. Ziegler and J.P. Biersack. The stopping and range of ions in matter. In *Treatise on heavy-ion science*, pages 93–129. Springer, 1985.

[9] G.S. Was. *Fundamentals of Radiation Materials Science: Metals and Alloys*. springer, 2016.

[10] K. Ankit, B. Derby, R. Raghavan, A. Misra, and M.J. Demkowicz. 3-d phase-field simulations of self-organized composite morphologies in physical vapor deposited phase-separating binary alloys. *Journal of Applied Physics*, 126(7):075306, 2019.

[11] Y. Lu, Y. Wang, C.and Gao, R. Shi, X. Liu, and Y. Wang. Microstructure map for self-organized phase separation during film deposition. *Physical Review Letters*, 109(8):086101, 2012.

[12] B.K. Derby, J.K. Baldwin, M.J. Wang, Y.and Demkowicz, A. Misra, and N. Li. Influence of metal nanocomposite morphology on helium implantation response. *Scripta Materialia*, 177:229–233, 2020.

[13] P. Yue and J.J. Feng. Wall energy relaxation in the cahn–hilliard model for moving contact lines. *Physics of Fluids*, 23(1):012106, 2011.

[14] A. Mukherjee, K. Ankit, R. Mukherjee, and B. Nestler. Phase-field modeling of grain-boundary grooving under electromigration. *Journal of Electronic Materials*, 45(12):6233–6246, 2016.

[15] D.J. Seol, S.Y. Hu, Y.L. Li, J. Shen, K.H. Oh, and L.Q. Chen. Computer simulation of spinodal decomposition in constrained films. *Acta Materialia*, 51(17):5173–5185, 2003.

[16] A. Van De Walle, M. Asta, and G. Ceder. The alloy theoretic automated toolkit: A user guide. *arXiv preprint cond-mat/0212159*, 2002.

[17] J. Hafner. Ab-initio simulations of materials using vasp: Density-functional theory and beyond. *Journal of Computational Chemistry*, 29(13):2044–2078, 2008.

CHAPTER III

Homogeneous Phase Separation in Binary,Cu-Mo Thin Films

Nanostructured thin films are of great importance to a wide variety of technological fields. Whether serving mechanical, chemical, optical, or electronic functions, the physical and electronic properties of these films depend on their structure and morphology [1]. Numerous studies have linked thin film morphology to the deposition conditions imposed during processing [2–5]. The relationship between deposition conditions and thin film morphology remains essential to their functional implementation.

3.1 Introduction

Early work connecting thin film morphology to the deposition conditions was done by Movchan and Demchishin [2]. This was later improved upon by Thornton [4] and resulted in a zone diagram for the morphology of single phase thin films as a function of homologous deposition temperature and the chamber pressure during processing. While the Thornton diagram is applicable to single-phase films, many

modern technologies rely on two-phase films for their functionality. Many functional devices still depend on monolithic, multilayer designs, but *in situ* phase separation provides an accessible route to new and unique morphologies that can be used to increase efficiency for future devices [6, 7]. Unfortunately, a systematic understanding and linkage between deposition conditions and film morphology in phase separating, multi-component thin films is lacking.

In any material system, the current and equilibrium thermodynamic states determine the conditions for phase separation [8]. The system is thermodynamically unstable if the free energy of the system can be decreased continuously with an internal change. Thus, a system's energy differences upon transformation determine the requisite conditions for spontaneous phase transformation. Gibbs classified all phase transformations into two broad categories: continuous phase transformations and discontinuous phase transformations.

Whereas continuous transformations smoothly evolve over the entire system, discontinuous transformation occur abruptly in a small region of the sample (e.g. nucleation and growth) [9]. In the case of multi-component systems, when the Gibbs free energy of a phase goes through a maximum in some portion of the composition range, there exists a miscibility gap where two or more phases co-exist. The system will reduce its free energy through a continuous transformation (e.g. spinodal decomposition) or discontinuously by a nucleation and growth mechanism [10–12].

In both cases, phase separation in equilibrium, multicomponent systems where

pressure and temperature are clearly defined involves a reaction at the interface of the decomposed and decomposing solid and is well documented [13]. Thin films, however, are grown under non- equilibrium conditions with high kinetic energies and short growth duration [14]. As such, dynamics are constrained to occur only along the growing surface as long as bulk diffusion is negligible at relatively low deposition temperatures.

For thin film growth, the kinetic "route" taken regulates the final kinetically determined state [14]. The major kinetic constraints on phase separation during thin film growth is the ratio between the adatom mobility and the growth rate [15, 16]. This inherently determines the diffusion length an adatom can travel before being buried by the incoming flux. During PVD sputtering, external control over the temperature and deposition rate will affect this ratio and thus influence the resultant phase separated morphology [16].

To understand the effects of these externally imposed conditions on the kinetics during thin film growth, we have performed an empirical study of phase separation in a co-sputtered, immiscible Cu-Mo thin film system. The complete immiscibility over a wide temperature and composition range make Cu-Mo an ideal binary system to study the effects of deposition conditions on *in situ* phase separating film morphology. This is shown in the Cu-Mo phase diagram as presented in Fig. 3.1 [17]. This degree of immiscibility is expected to lead to phase separation during co-sputtering at elevated temperature provided the requisite kinetic conditions ex-

ist [18]. The microstructure of the as-deposited films were studied using scanning transmission electron microscopy. X-ray and electron diffraction were used for phase identification. Compositional analysis of the films was determined by X-ray flouresscence spectroscopy and energy dispersive X-ray spectroscopy. The results of the synthesis will be followed by a discussion of the physical mechanisms on their formation during PVD co-sputtering. The observed transitions in morphologies were interpreted using an inter-diffusional model. The mechanical behavior of these bicontinuous morphologies are also presented. A 3-dimensional phase field model showing the same progression of thin film morphologies based on deposition conditions is presented at the end of this chapter.

3.2 Experimental Observations

Phase separation was observed in all of the deposited films, except for those deposited at 400 °C where a coherent matrix of (Cu)-BCC and (Mo)-BCC was observed. Fig. 3.2 shows the XRD profiles of the samples deposited at 400, 500, 600, 700, and 800 °C, respectively.

The Cu- and Mo-rich terminal phases were the only identifiable phases at all temperatures. Beginning at 400 °C, a small but distinguishable Cu (111) peak emerged from a broad X-ray amorphous background. The peak lying between the Cu FCC (111) and Mo (110) BCC lines indicate a nanograined (Mo) and (Cu) BCC solid solution, which was observed in high resolution shown in Fig. 3.3.

At deposition temperatures 500 °C and above, the broad peaks between the Cu

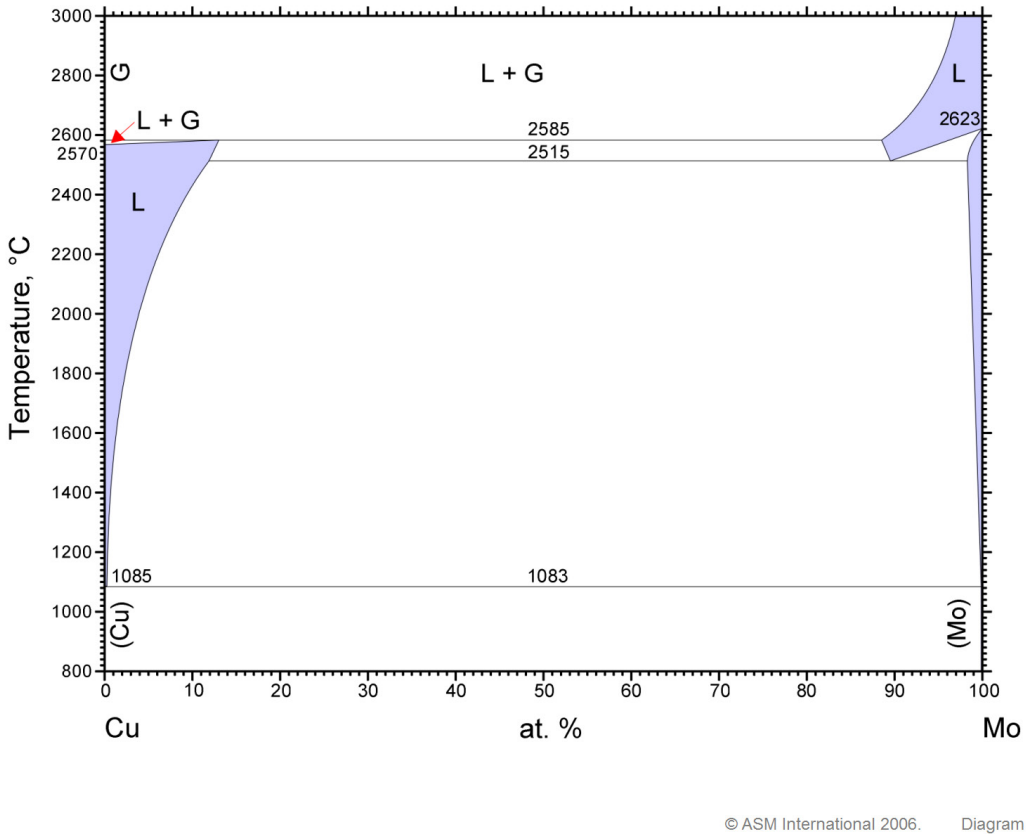

Figure 3.1: Equilibrium phase diagram for the Cu-Mo system. From Ref. [17].

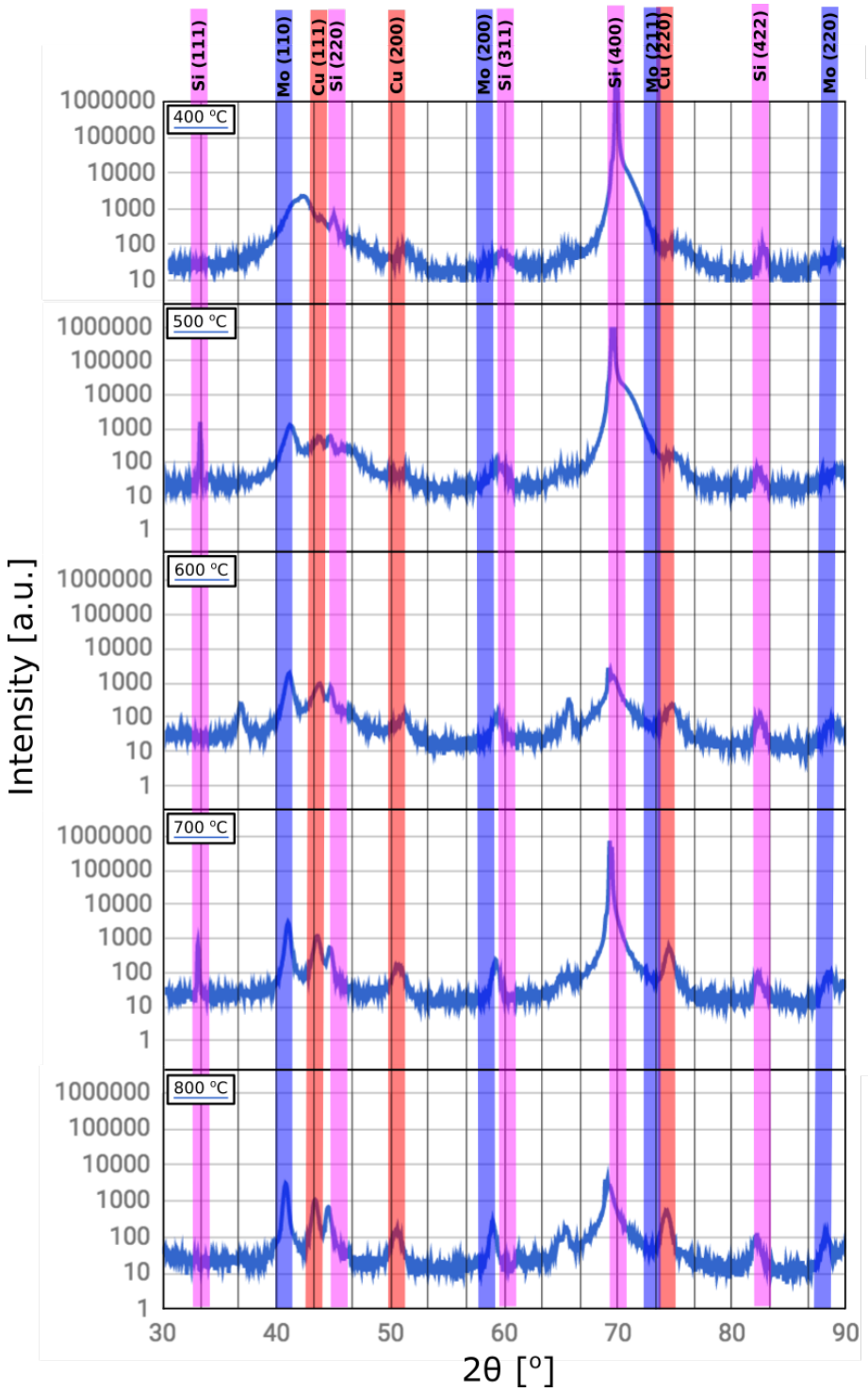

Figure 3.2: θ - 2θ X-ray diffraction patterns for Cu-Mo films deposited at 400, 500, 600, 700, and 800 °C. At 400 °C a small but definite Cu-rich phase phase crystallizes with (111) texture. Crystallization of a second phase with Mo structure begins at 500 °C; (110) and (200) peaks are most prominent; the (220) peak is only observed beginning at 600 and 700 °C. Silicon substrate peaks are labeled. There are unidentifiable peaks in the 600 °C and 800 °C samples. From Ref. [19].

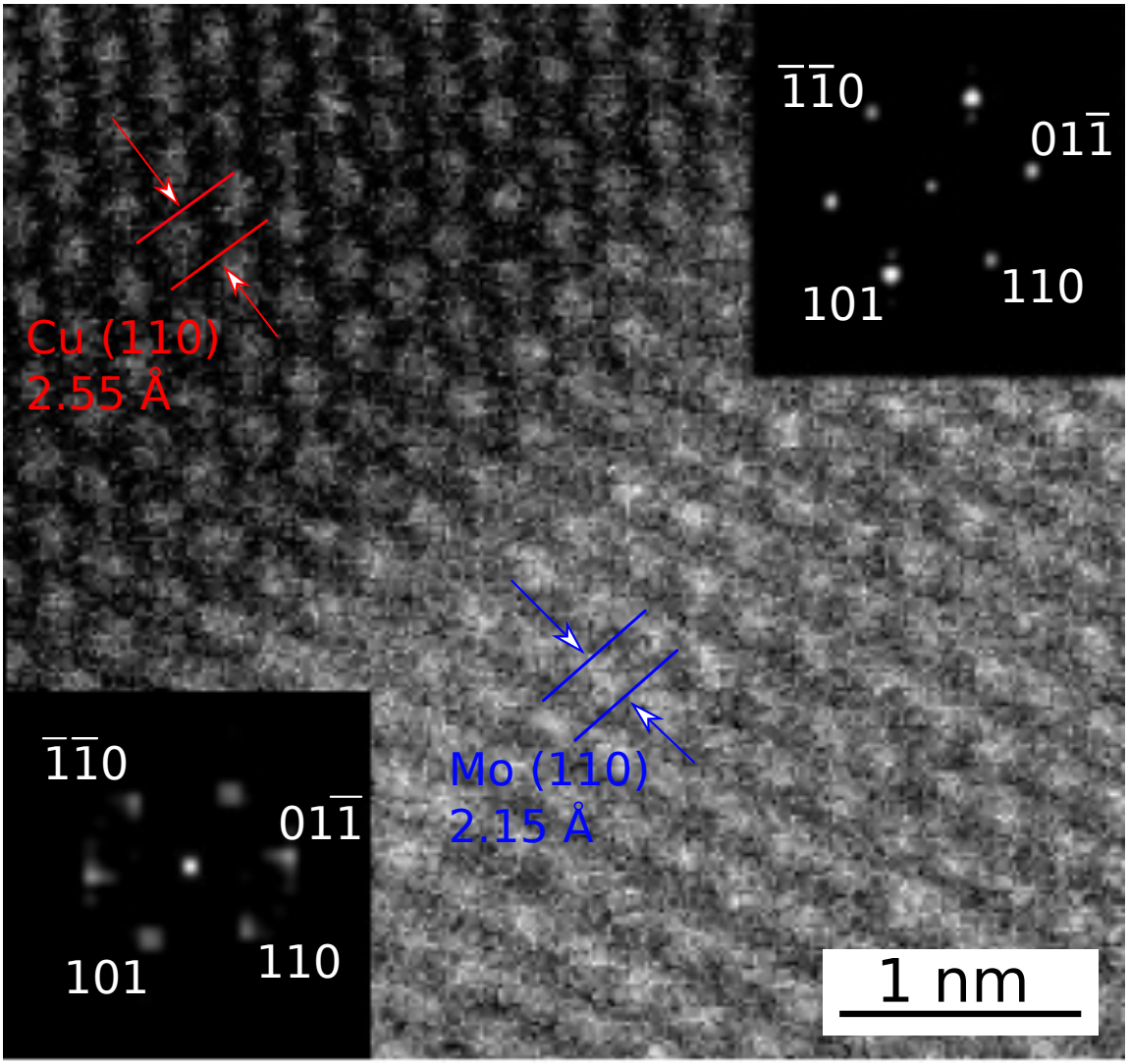

Figure 3.3: HAADF images of the sample deposited at 400 °C viewed in atomic resolution. A coherent (Mo) and (Cu) BCC solid solution is observed. The inset power spectra (bottom left taken from the upper right Cu region and vice-versa) exhibit the same FFT pattern with a B = [-111] zone axis. The interface is parallel to the (110) plane indicating the coherent structure. From Ref. [19].

FCC and Mo BCC split as several Mo BCC and Cu FCC peaks characteristic began to appear. These peaks became more prominent at higher deposition temperatures.

3.2.1 Vertical Concentration Modulations

S/TEM analysis of the sample deposited at 400 °C presented in Fig. 3.4 exhibited composition modulations perpendicular to the deposition direction when viewed in cross-section.

The vertically-oriented concentration modulations (VCM) are roughly 10 nm in wavelength and extend the entire 1000 nm film thickness. Careful observation reveals that there is slight lateral directionality within each Cu-Mo band. Viewing the same specimen in plan-view shows that the Cu-Mo phases extend into the thickness of the film in a random, bicontinuous path. The broadening observed in the selected area diffraction patterns (SADP) shown in the upper insets of Fig. 3.4 and Fig. 3.5 indicates a nanograined Cu-Mo structure and Fig. 3.3 indicates that the interfaces are coherent similar to the results obtained by Harzer and coworkers in their study of Cu-Cr films [20]. Additionally, Fig. 3.3 is a high-resolution HAADF image that showed one-to-one atomic plane matching at the interface, as expected for coherent interface.

The SADP shows the locations of the Cu-FCC (111) and Mo-BCC (110) planes. The electron diffraction peaks laying in between these indicated peaks indicates a (Mo) and (Cu) solid solution similar to those results found for Cu-Mo bimetallic nanoparticles. This coherent structure is confirmed in the high-resolution image of

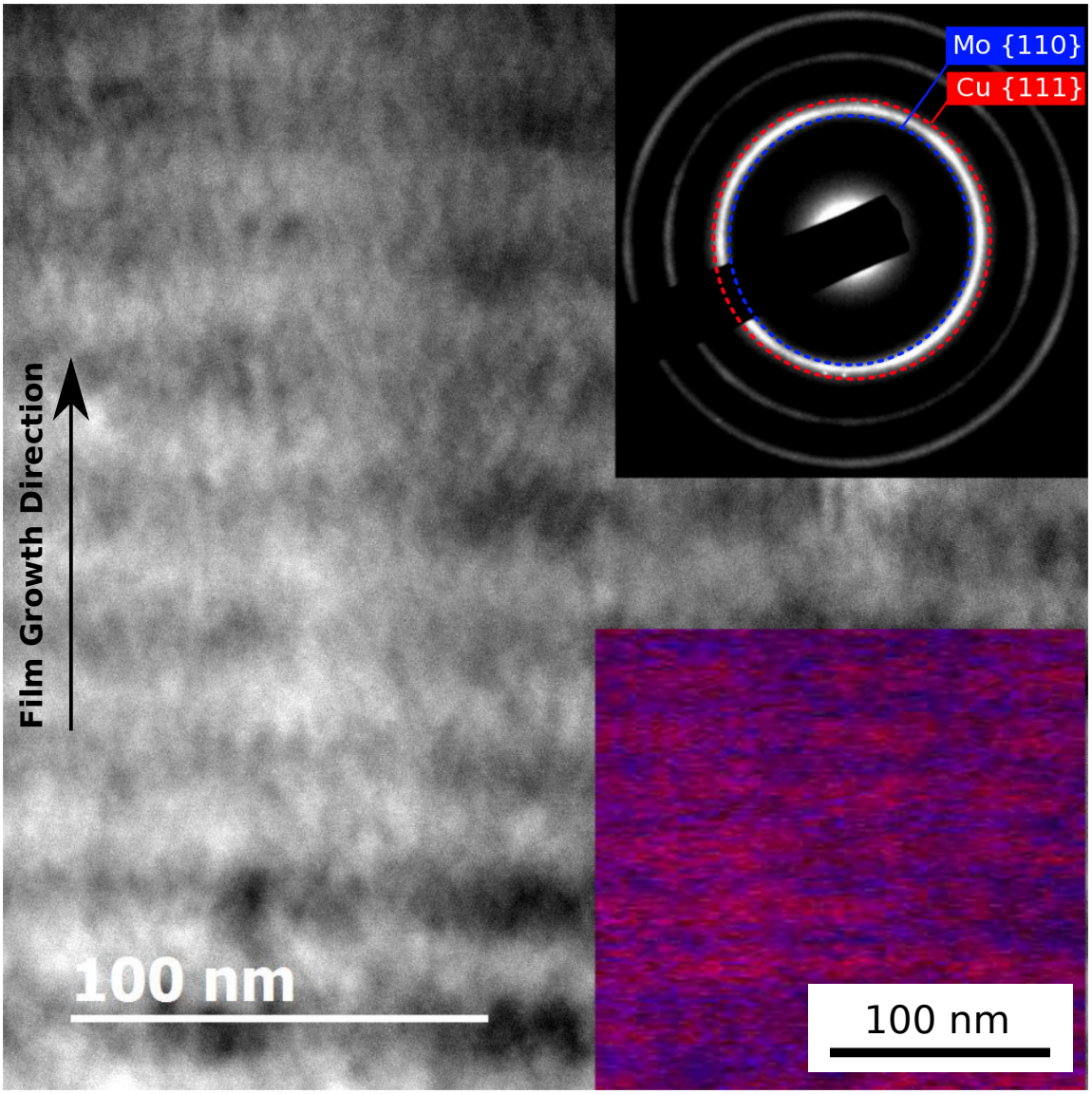

Figure 3.4: HAADF images of the sample deposited at 400 °C viewed in cross-section. The Cu-Mo domains are oriented vertically with respect to the substrate as shown in the bottom right EDXS map inset. In these maps, Cu is highlighted blue and Mo, red. The film growth direction is as indicated, from bottom to top. There does exist some lateral character to the Cu-Mo phases with a frequency of approximately 4 nm. The inset SADP shows peak broadening from a nano-grain structure with a coherent interface as shown in Fig. 3.3. The markings in the SADPs illustrate the locations of the Cu-FCC and Mo-BCC rings to guide the eye. A single peak located in between these two planes is observed at this deposition temperature. From Ref. [19].

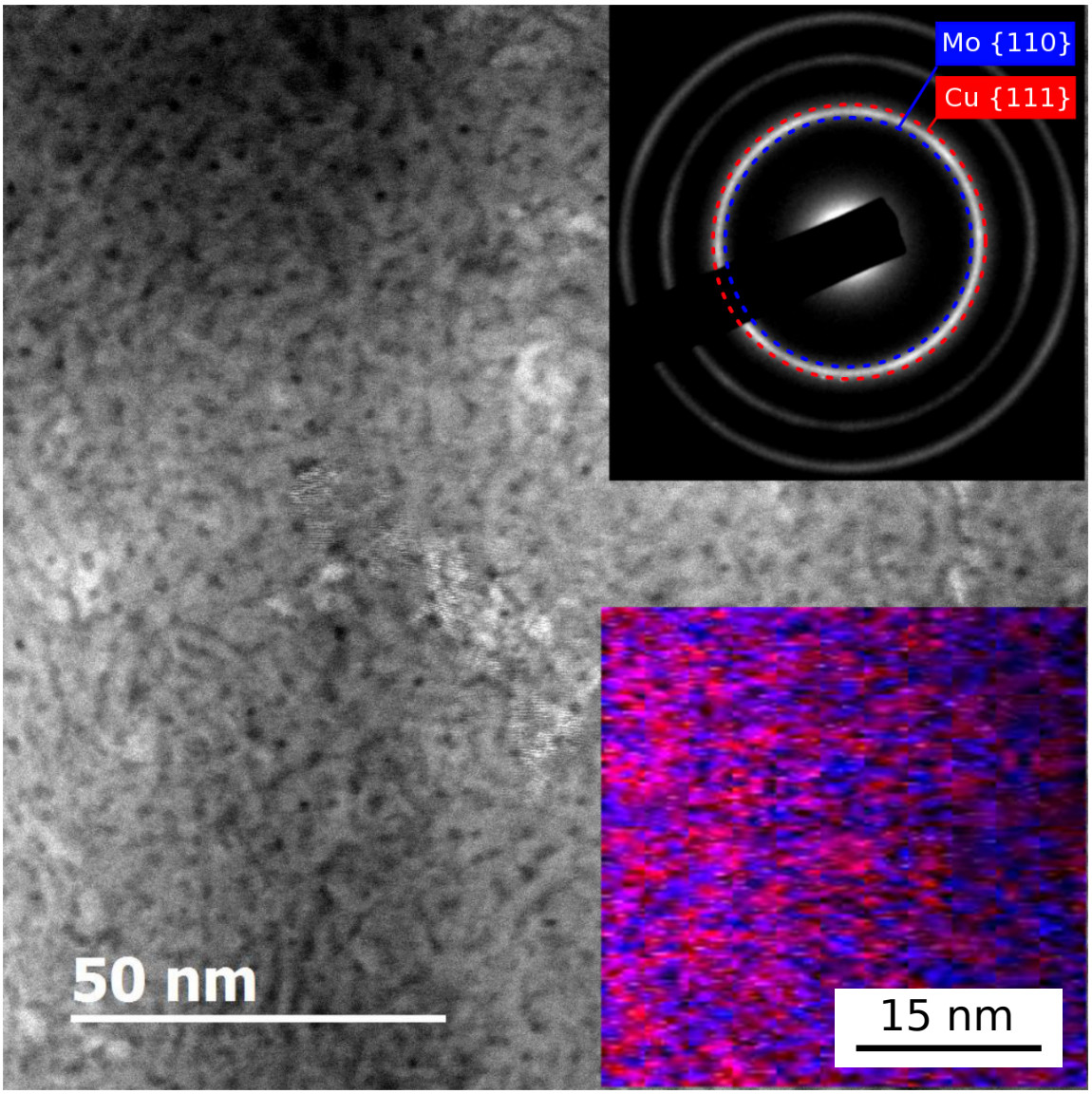

Figure 3.5: HAADF images of the sample deposited at 400 °C viewed in plan-view. The Cu and Mo phases are observed to extend in a bicontinuous morphology in plan-view. This is confirmed using EDXS mapping shown in the bottom right EDXS map inset. In these maps, Cu is highlighted blue and Mo red. The inset SADPs show peak broadening from a nano-grain structure. The markings in the SADPs illustrate the locations of the Cu-FCC and Mo-BCC rings to guide the eye. A single peak located in between these two planes is observed at this deposition temperature. From Ref. [19].

the sample shown in Fig. 3.3. This shows a high-resolution HAADF image of the interface between the (Mo) and (Cu) taken from the plan-view sample. The inset power spectra from each region (bottom left is from upper left Cu region and vice-versa) show the same FFT pattern for each phase. At this deposition temperature, the sample was observed to be in a (Mo) and (Cu) solid solution.

3.2.2 Lateral Concentration Modulations

Increasing the substrate temperature to 600 °C led to a contrasting morphology from the VCM structure exhibited in Fig. 3.4 to lateral concentration modulations (LCM) as shown in Fig. 3.6.

The Cu and Mo domains have phase separated perpendicular to the growth direction as shown in Fig. 3.6. The EDXS mapping inset also shows this lateral domain character. While these lateral domains extend for most of the film thickness, nearest to the substrate, a randomly-oriented structure was observed roughly 50 nm in thickness before transitioning to the LCM structure. The increased temperature has led the Cu and Mo domains to coarsen twofold to approximately 16 nm in bilayer thickness. As shown by the inset SADP, Cu grains exhibited an FCC structure in the sample deposited at 600 °C and preferred orientation, Cu 111 // Mo 110, was observed oriented perpendicular to the growth direction. All of the grains were oriented within 18° of this direction. The separable Cu (111) and Mo (110) peaks in the inset SADPs indicate phase separation of the Cu-Mo domains into Cu-FCC and Mo-BCC. The sample exhibited a similar behavior to the 400 °C sample in that the Mo-BCC

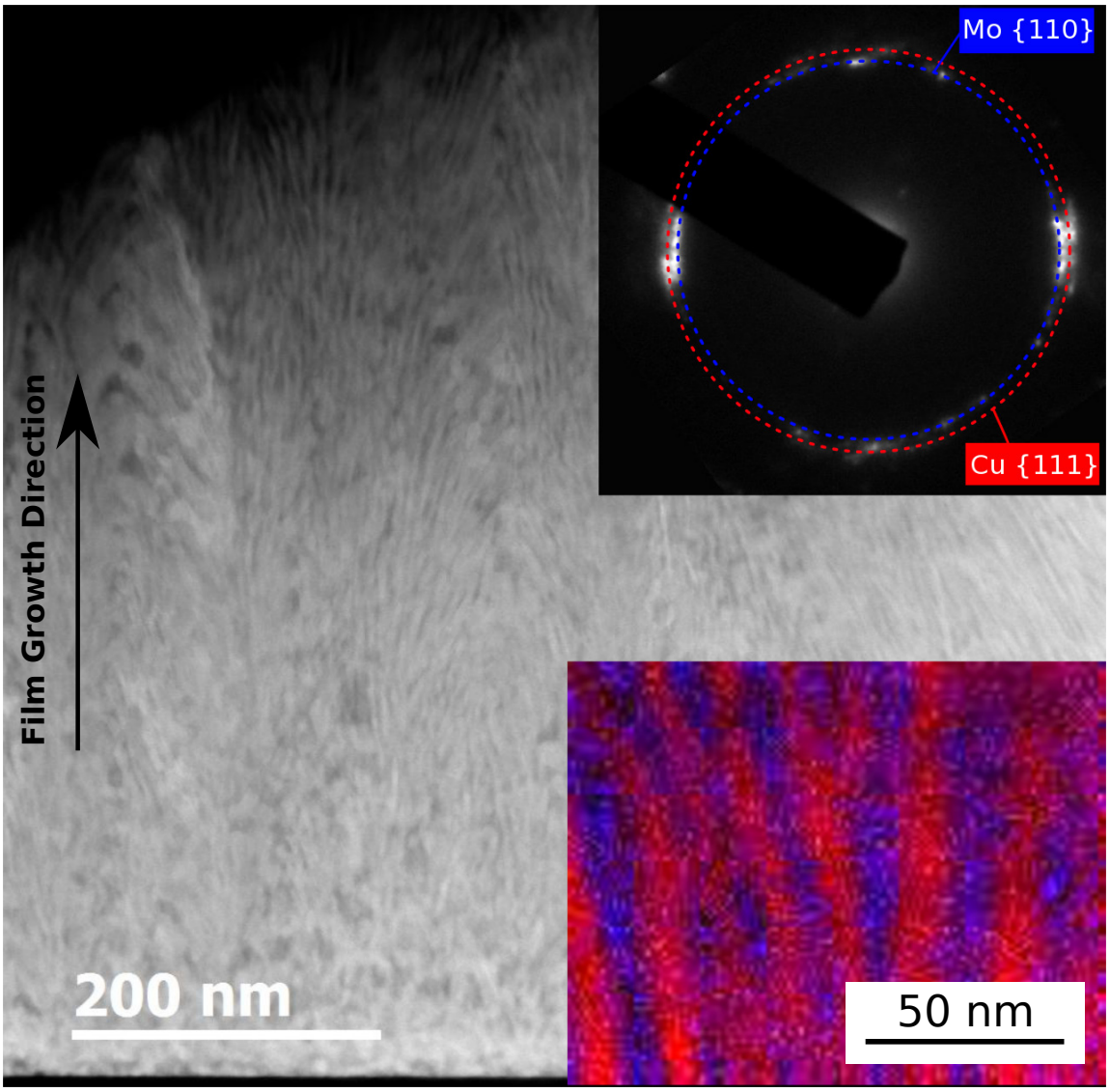

Figure 3.6: HAADF images of the sample deposited at 600 °C viewed in cross-section. The Cu-Mo domains have evolved such that they are oriented laterally with respect to the substrate as shown in the bottom right EDXS composition map inset. The film growth direction is as shown from bottom to top. The SADP shows a phase separated Cu-FCC and Mo-BCC domains in this structure. The film exhibits preferred orientation, Cu 111 // Mo 110, oriented perpendicular to the growth direction. From Ref. [19].

and Cu-FCC phases extend randomly in an interweaving, bicontinuous pattern into the thickness of the film while observing the sample in plan-view as shown in Fig. 3.7.

3.2.3 Random Concentration Modulations

A coarser structure was observed when the substrate temperature was increased to 800 °C and is shown in Fig. 3.8. When viewing the sample in both cross-section and in plan-view, the Cu and Mo domains were oriented more randomly with respect to the film growth direction as compared to the sample deposited at 600 °C. The domains are organized in such a morphology for the entire thickness of the film. The bilayer thickness also coarsened to roughly 32 nm in dimension as measured using the intercept method used for grain size calculations [21]. Similar to the sample deposited at 600 °C, the Cu and Mo domains were observed to be interweaving and bicontinuous, but in this case both in plan-view and cross-section as shown in Fig. 3.9. No preferred orientation of the Mo and Cu crystals was observed as is shown in the inset SADPs, but local texture with Cu 111 // Mo 110 was observed.

3.2.4 Summary of Experimental Results

No transition in morphology was directly observed when keeping the substrate temperature constant and varying the deposition rate. Instead, a refinement of the structure was observed with increasing deposition rate. Fig. 3.10 shows samples deposited at constant substrate temperature of 800 °C at different combined deposition rates as indicated in the center inset.

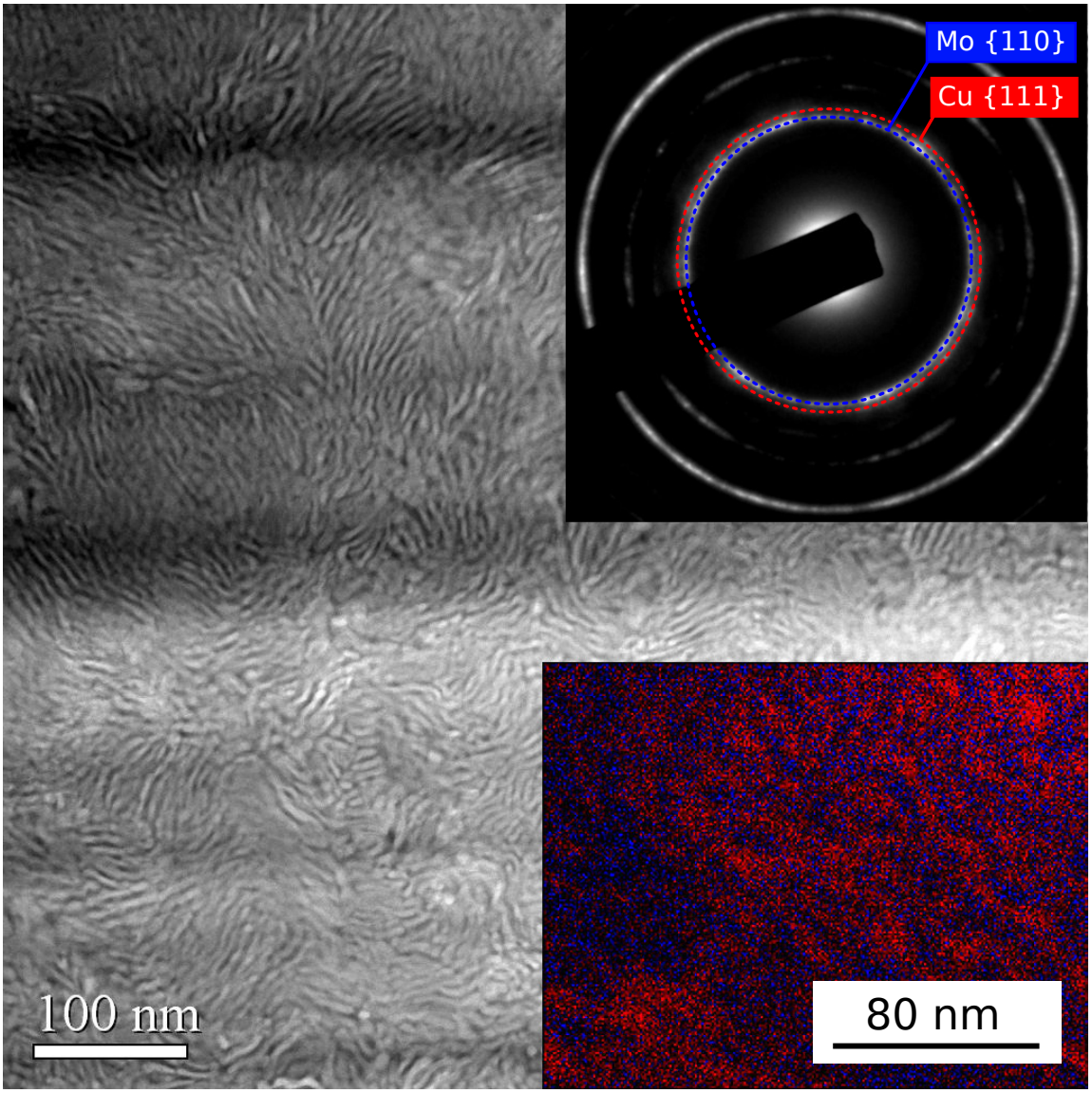

Figure 3.7: HAADF images of the sample deposited at 600 °C viewed in plan-view. A similar bicontinuous morphology of interweaving Cu-Mo phases was observed here as compared to Fig. 3.5, but with a slightly coarser structure. In this case, the increase in substrate temperature led to a phase separated structure with separable Cu-Mo peaks in the SADP. From Ref. [19].

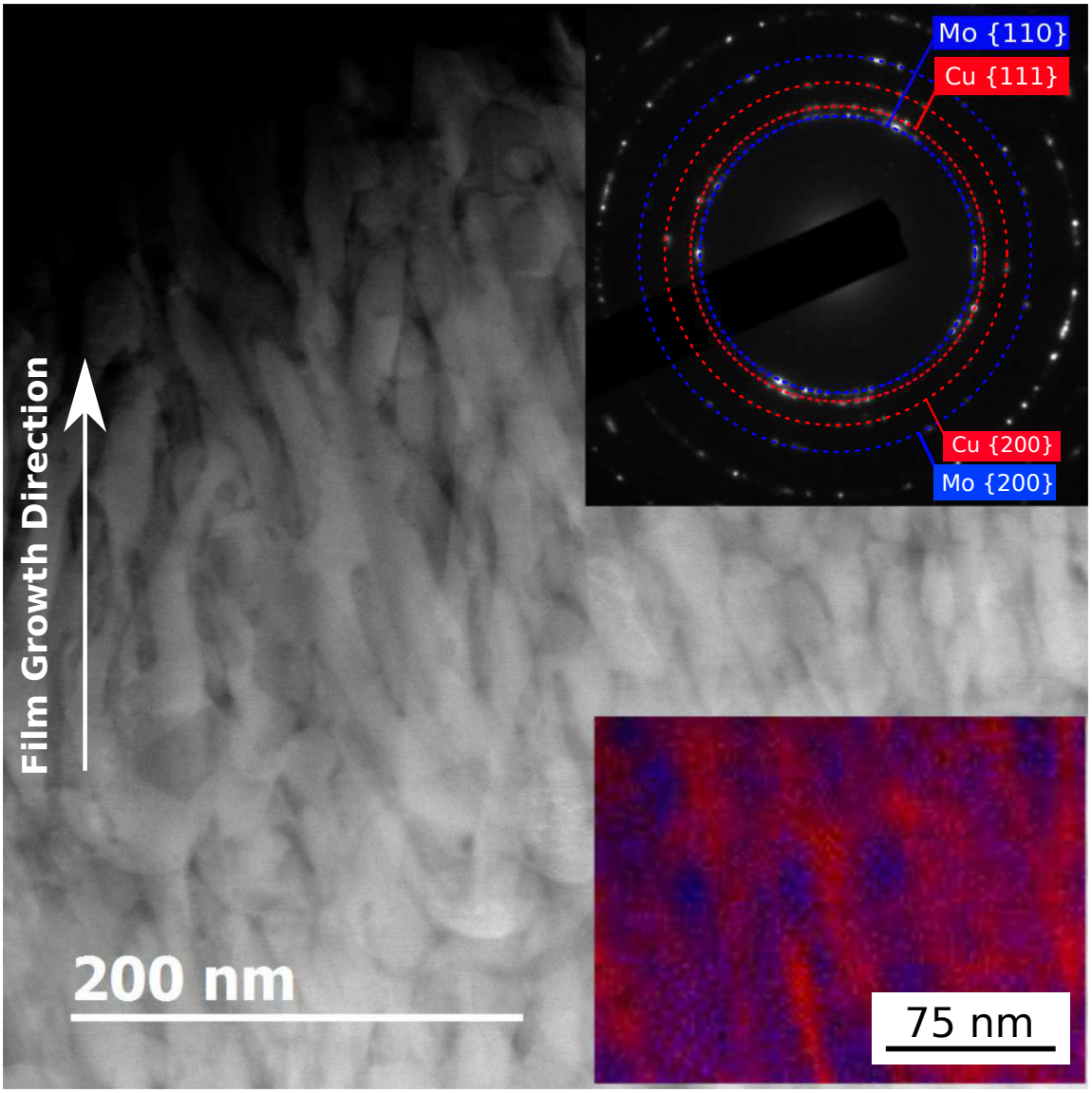

Figure 3.8: HAADF images of the sample deposited at 800 C viewed in cross-section. The Cu-Mo domains are oriented randomly with respect to the film growth direction as compared to the sample deposited at 600 °C.The film growth direction is from bottom to top. The SADP insets show FCC Cu and BCC Mo domains in this structure. From Ref. [19].

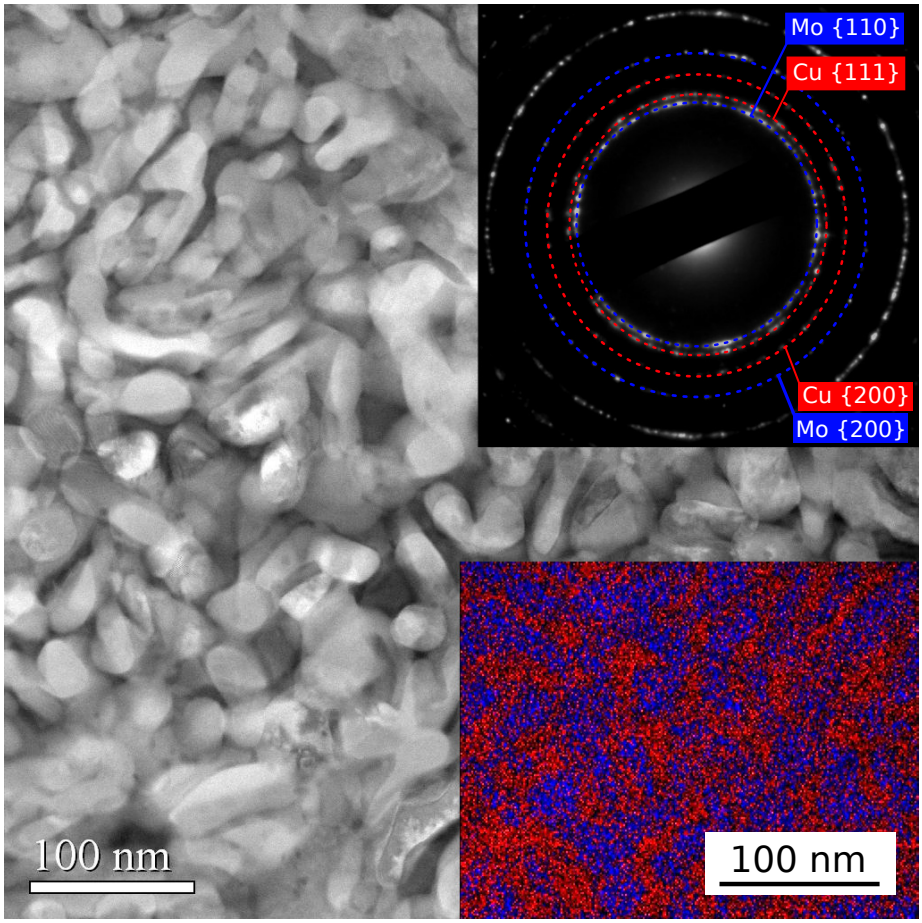

Figure 3.9: HAADF images of the sample deposited at 800 °C viewed in plan-view. The Cu-Mo domains are oriented more randomly than the sample deposited at 600°C and with respect to the substrate as shown in the EDX mapping inset. The SADP insets show FCC Cu and BCC Mo domains in this structure. From Ref. [19].

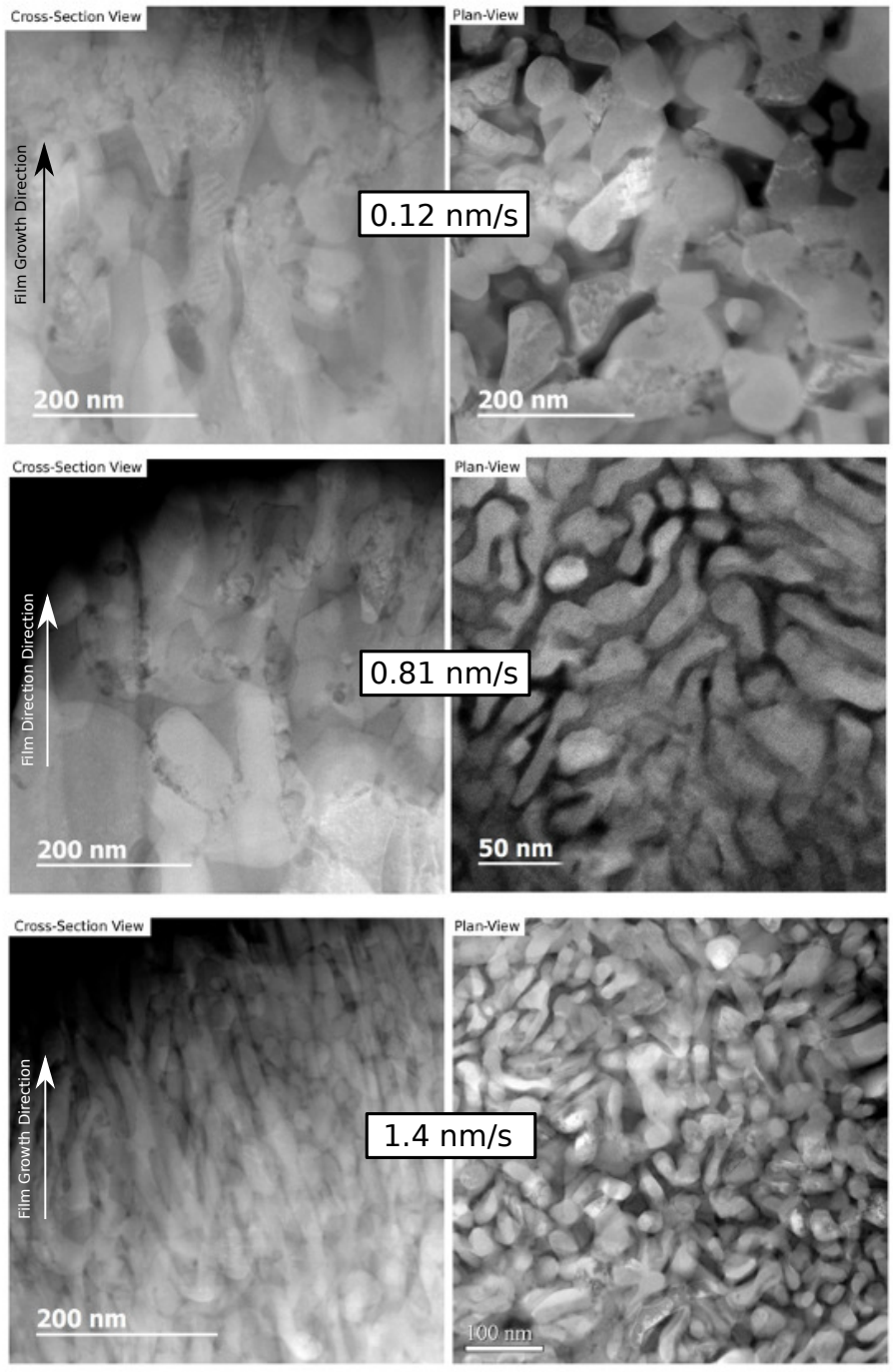

Figure 3.10: HAADF images of co-deposited Cu-Mo samples deposited at 800 °C at varying deposition rates as viewed both in cross-section and plan-view. The corresponding deposition rates are displayed as the center inset. A refinement in bilayer (Cu+Mo phase) length was observed at increasing deposition rate. Concentration modulation wavelength is plotted in Fig. 3.11. From Ref. [19].

At all deposition rates, a bicontinous morphology of interweaving Cu-Mo phases was observed. As the deposition rate was increased, a refinement of the Cu-Mo domains was observed ranging from 72 nm at the lowest deposition rate of 0.12 nm/s to 32 nm at the highest deposition rate of 1.4 nm/s. A similar behavior was observed for the films exhibiting the LCM structure deposited at 600 °C. These measurements are plotted in Fig. 3.11. We observed a domain size fit of approximately $1/\sqrt{\nu}$, where ν is the deposition rate.

In summary, we have shown that at increasing substrate temperatures, the morphology of these Cu-Mo films evolves from a VCM structure to an LCM structure followed by an interweaving architecture when viewed in cross-section. All of the samples presented an interweaving, bicontinuous structure when viewed from top-down. The increase in substrate temperature also led to a coarsening of the Cu-Mo bilayer dimension from 10 nm at 400 °C to approximately 32 nm at 800 °C. The effect of increasing deposition rate at constant substrate temperature was observed to be a refinement of the domain sizes with no change in morphology observed.

3.3 Phase Separation Mechanism

Mutual solubility is extremely limited in the Cu-Mo system and thus thermodynamics favor phase separation at equal atomic fractions and at all temperatures up to the melting temperature of Mo. The Mo-Cu system has a heavily positive enthalpy of formation $\Delta H \approx 28$ kJ mol^{-1} and is completely immiscible in its bulk form [17]. The deposition conditions established kinetics during our depositions such that

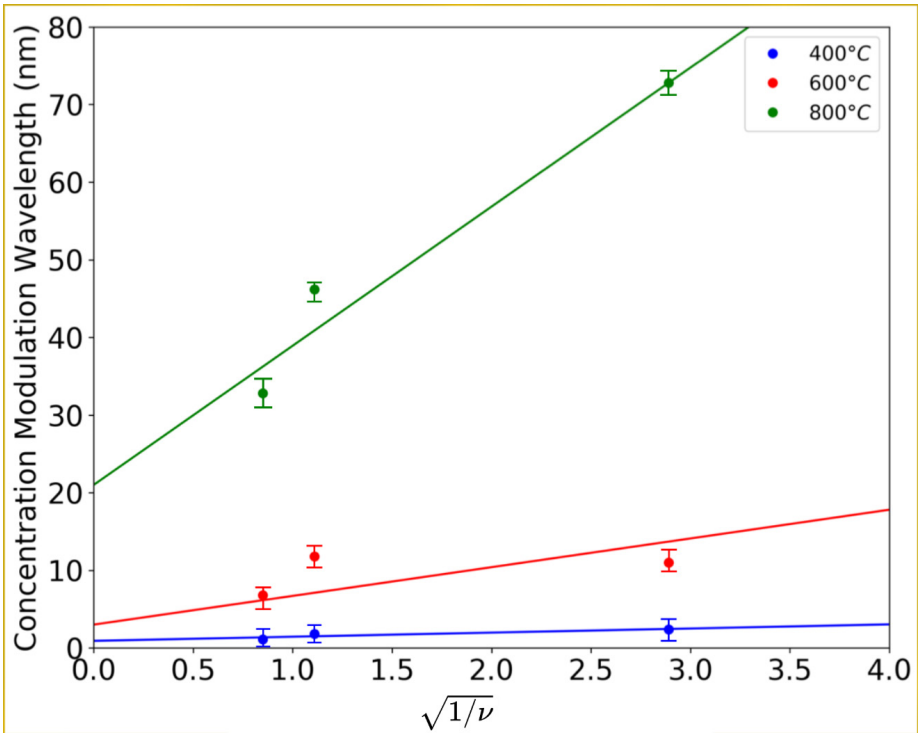

Figure 3.11: A plot of the average concentration modulation wavelength (Cu+Mo phase) length as a function of the inverse square root of the deposition rate. An average of 20 measurements were made for each sample as viewed both in cross section and plan-view. It can be observed that in the case of the sample deposited at 800 °C, the domain size decreases approximately at a rate of $\sqrt{1/\nu}$. From Ref. [19].

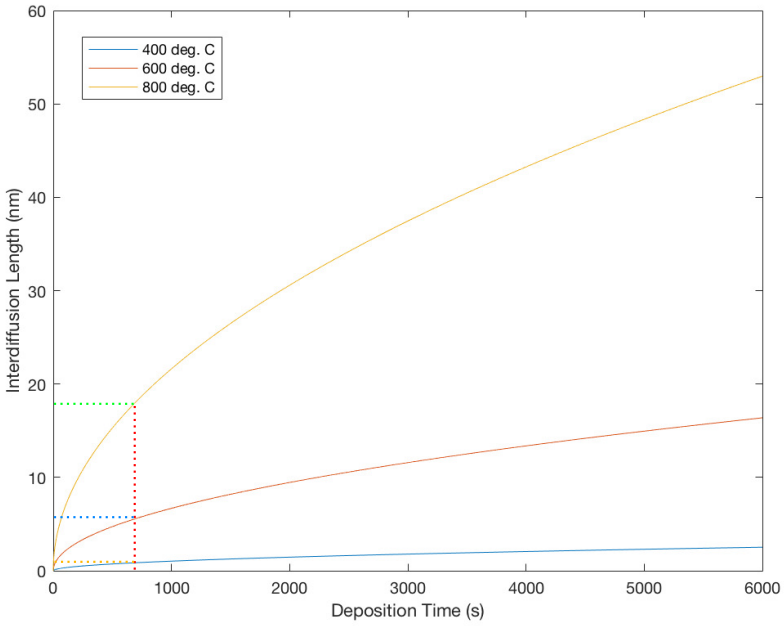

Figure 3.12: Interdiffusion length in nanometers as a function of deposition time for the Cu-Mo system at each of the substrate temperatures studied in this experiment. Vertical red line marks the deposition time for the films used in this study. From Ref. [19].

phase-separated morphologies were observed at all substrate temperatures, except at those films deposited at 400 °C where a non-homogeneous (Mo) and (Cu) solid solution was observed.

At the temperatures and total deposition times reported here, surface interdiffusion is the dominant kinetic process controlling the morphology of the film and the limiting factor of the interfacial free energy written as

$$\sigma = N_v \int_{-\infty}^{\infty} \left[f_0 + \kappa(\nabla c)^2 c + \mu_B(e) - (c-1)\mu_A(e) \right] dx, \tag{3.1}$$

where N_v is the number of molecules per unit volume, f_0 is the free energy per molecule of a solution of uniform composition, $\kappa = [\partial^2 f/\partial c \partial \Delta^2 c]_0 + [\partial^2 f/\partial |\Delta c|^2]_0$ and represents a tensor reflecting the crystal symmetry, c is the concentration as a function distance, $\mu_i(e)$ is the chemical potential per molecule of constituent i [22].

This can be reasoned by a calculation of the bulk interdiffusion distance achievable during the deposition time. The bulk interdiffusion coefficient for Cu-Mo - using $D_0 = 1.32 \times 10^{-14}$ m^2/s and $Q = 0.948$ eV/atom [23] - is 1.05×10^{-21} m^2/s is calculated and plotted for the various substrate temperatures used in this study in Fig. 3.12.

At 400 °C for example, the bulk interdiffusion distance $[x = (Dt)^{1/2}]$ is 0.9 nm at a deposition time of 715 s, which is less than 1% of the average domain diameter for the VCM sample. This is the case for each respective temperature and morphology. Thus, bulk interdiffusion of each constituent can be assumed negligible (at least for

800 °C), and surface interdiffusion can be reasoned as the dominant kinetic factor during deposition.

The mechanism of phase separation, whether a continuous or dis-continuous transformation, for these thin films is difficult to determine while depositing at elevated temperature. This is because most diffusion is happening strictly at the surface and then subsequently frozen in place by the incoming flux as reasoned by Adams *et. al.* [15]. This is known as the frozen bulk approximation. As shown by Atzmon et. al., it must be mentioned that the limitation of the frozen-bulk equation that the composition profile is underdetermined [15]. In their work, the authors concluded that the composition profile in the film below the surface reflects the history of the composition profile at the film surface. This implies that the composition profile in the film below the surface reflects the history of the composition profile at the film surface [15].

Considering that the deposition rate is an externally imposed parameter in thin film deposition, the phase separation mechanism during growth does not fit the classical definitions of spinodal decomposition or nucleation and growth as described by Cahn [11].

The combined deposition rate for these samples was 1.4 nm/s. Thus, after every second, the layer of material previously deposited is buried by a new flux of 1.4 nm of material. Using the plot shown in Fig. 3.12, we see that at even at the highest deposition temperature, 800 °C, the interdiffusion distance is 0.68 nm for 1 second

of deposition. As such, it can be assumed that the adatoms arriving on the growing surface can travel 0.68 nm at most before being frozen in place by the incoming flux. In other studies, e.g., Muller et al. [24], Cu-Ta films were deposited at room temperature to produce a chemically homogeneous amorphous film. Post-deposition annealing at relatively low temperatures was re-ported to produce spinodally decomposed Cu and Ta phases. However, in our study, elevated temperature co-deposition is presumably resulting in phase separation at time scales comparable to the deposition time for film growth. From this, and the analysis done on laterally separating Al-Ge films [15], we conclude that in these samples, the film phase separates into Mo- and Cu- rich domains, which coarsen through surface interdiffusion during deposition. At some time during growth, the surface interdiffusion distance, which is temperature dependent, contributes to determining the steady-state compositional domain size. However, the surface interdiffusion distance does not uniquely determine the domain size since there is still one degree of freedom: the supersaturation will increase with the increase of the domain size.

3.3.1 Morphology Evolution

For phase separation to occur throughout deposition, thermodynamics must favor this process. This is the case for the Cu-Mo system in which the mutual solid solubilities are extremely limited [17]. Additionally, sluggish kinetics may prevent the formation of phase-separated microstructures consisting of the equilibrium phases [15]. Our deposition conditions established kinetics such that we observed phase

separation in all Cu-Mo films co-sputtered at the substrate temperatures studied here.

To describe the development of these morphologies, we will assess the how the system is being driven towards minimizing the total interfacial energy term contributing to the total free energy. Assuming a one-dimensional composition change across the interface, the interfacial free energy for a binary A-B system that contains a miscibility gap can be written as Eq. 3.1.

Applying Cahn's analysis of temporal evolution of the concentration in eutectoid growth to phase separating films we can write the concentration change over time as

$$\frac{\partial c}{\partial t} = D_s \nabla^2 c + \frac{\nu}{\delta}(c_0 - c), \tag{3.2}$$

where t is the deposition time, D_s is the surface interdiffusivity, ν is the deposition rate, δ is the modulation length, and c_0 is the sputtering flux. Adams and coworkers applied this equation to morphology development in their Al-Ge films [15]. They also showed that from the concentration change written in Eq. 3.2, the surface interdiffusion length can be written as

$$\rho = \sqrt{\frac{D_s \delta}{\nu}}. \tag{3.3}$$

Since D_s has an Arrhenius relationship with respect to temperature, the interdiffusion length increases as a function of substrate temperature. Maintaining a constant deposition rate, the interdiffusion length is strictly controlled through the

substrate temperature.

3.3.2 Substrate temperature effects

Vertical concentration modulations

Films deposited at 400 °C exhibited composition modulations parallel to the growth direction. The films do show the existence of lateral domain character in which localized areas phase separated perpendicular to the film growth direction. The origins of these nano-sized lateral domains will be included in future work as we focus on the larger VCM structure in this report.

Out of the three cases studied, the interdiffusion length is the smallest according to Eq. 3.3 for the sample deposited at 400 °C. Following the argument made by Lu and colleagues, the VCM structure is stable when the rate of phase separation (Eq. 3.1) is slower than the deposition rate [25]. In this case, the system is still within the decomposition region of the free energy diagram and when fresh layers bury previously deposited atoms, A- and B- rich regions absorb newly deposited A and B atoms, respectively via uphill diffusion. As such, a checkerboard structure of A- and B-rich regions initially develops. These regions eventually connect and form concentration modulations that are vertically oriented to form the VCM structure observed here. A schematic view of this process is shown in Fig. 3.13.

We would like to specifically mention, that we cannot rule out the necessity of bulk diffusion to describe the formation mechanism of the VCM morphology. The required bulk diffusion into the previously deposited layers as shown in Fig. 3.13

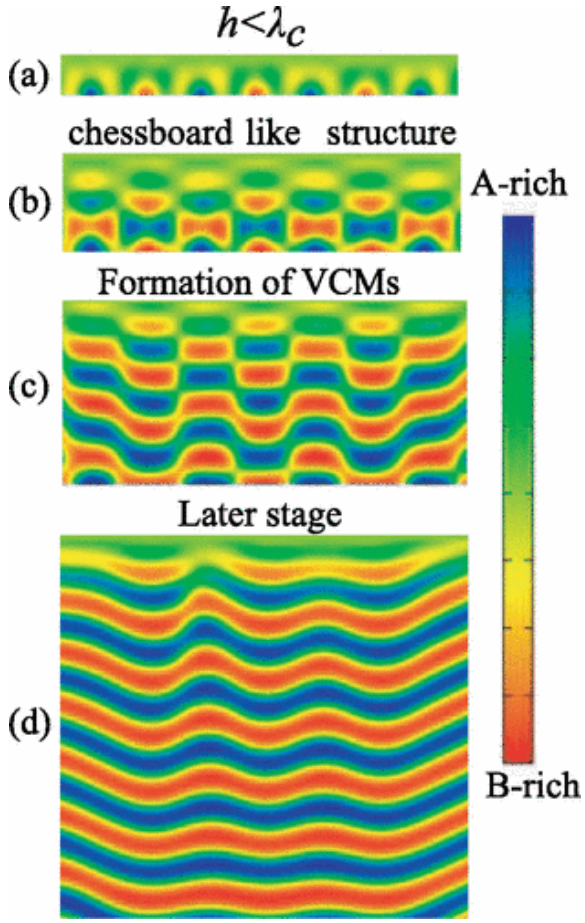

Figure 3.13: A cartoon schematic of VCM development at several time steps during deposition. When the film thickness (h) is smaller than the critical wavelength (λ_c) of spinodal decomposition, the concentration modulation can develop only along the horizontal direction as seen in (a). Because of the relatively fast deposition rate, the concentrations of the A-rich and B-rich regions in the decomposing film are still within the spinodal region. Thus, when a fresh layer is added, the A-rich and B-rich regions beneath simply absorb, respectively, A and B atoms from the freshly deposited layers via uphill diffusion (but down the chemical potential gradient). Then the regions in the freshly deposited layers above the A-rich regions will become A-lean while those above the B-rich regions will become B-lean. As a consequence, a chessboardlike structure is developed, as seen in (b). Then the A-rich islands connect with each other and the B-rich islands connect with each other, and the chessboard structure transforms into wavy strips as seen in (c). During further coarsening, the wavy stripes evolve gradually into horizontal stripes. After the horizontal stripes have developed, if the newly deposited layer is in contact with a B-rich stripe, then the B atoms in the fresh layer will diffuse into the underneath B-rich stripe via the same uphill diffusion mechanism. Because of the loss of B atoms in the fresh layer, a new A-rich stripe forms over the B-rich stripe as seen in (d). As this process repeats, a VCM structure eventually develops. Used with permission from [25].

necessitates bulk diffusion. This mechanism requires further experimentation and analysis and will be explored in future work.

The presence of a (Mo) and (Cu) BCC based solid solution was observed at 400 °C as indicated by the HRTEM image and electron diffraction patterns shown in Fig. 3.2. Similar to the work done on Mo-Cu bimetallic nanoparticles [26], we found that the measured interplanar spacing in two orthogonal directions (110) and (1-10) is $d_{110} = 0.215 \pm 0.05$ nm. This differs significantly with the spacing of pure Mo which is $d_{110} = 0.222$ nm. This deviation coincides with a BCC based solid solution as observed in Fe/Cu multilayers when the thickness of each layers is below a few nanometers in thickness [27]. Using Vegard's Law [28], we can determine the composition of the (Mo) and (Cu) solid solution to be 50 at.% BCC (Mo) and 50 at.% BCC (Cu).

It appears that the sample deposited at 400 °C shows signatures of spinodal decomposition, including a coherent matrix between (Cu)-BCC and (Mo)-BCC shown in Fig. 3.3. For systems with elastic misfit at early stages of spinodal decomposition, lattices are initially coherent and strains are continuous across interfaces [9]. As the domains coarsen, the system relieves the coherency stresses by forming interface misfit dislocations [29] to form semi-coherent interfaces. The XRD pattern shown in Fig. 3.2 also shows similarities to the XRD patterns obtained on the Cu-Ta system by Muller and colleagues and the Al-Si system studied by Fukutani *et. al.* [30]. Muller also observed an emergent Cu (111) peak from an X-ray amorphous background.

However, the separation in random directions and not strictly along elastically soft directions as shown in Fig. 3.4 makes it appear unlikely that the mechanism for these films fits the classical definition of spinodal decomposition.

Lateral concentration modulations

At higher substrate temperatures, the interdiffusion length and the rate of phase separation are larger. For an LCM morphology to develop, the rate of phase separation is faster than the deposition rate. This was the case for the sample deposited at 600 °C shown in Fig. 3.6 in which the Cu-Mo phases decomposed parallel to the film-substrate interface. In this case, as the first atoms are arriving on the substrate, there is enough time for the atoms to completely decompose and form domains on the surface, forming a template. As later flux arrives on the surface, it comes into contact with a well-decomposed layer underneath and each Cu and Mo constituent migrates to their respective domains. With unchanging kinetic conditions, this structure is free to continue until the end of the deposition to form the LCM structure.

Random concentration modulations

As the substrate temperature is increased even further as was the case for the sample deposited at 800 °C, the rate of phase separation becomes very large as compared to the deposition rate. [25]. As will later be shown using phase field simulation, we suspect bulk diffusion has been activated at the highest substrate temperatures explored in this study. The RCM morphology is a result of the interconnection (or breakdown) of the LCM domains due to the increased role of bulk diffusion during

deposition. The formation mechanism of the RCM structure is similar to annealing of a previously homogeneous alloy at high temperature.

Fig. 3.14 shows a 3D schematic of the effects substrate temperature has on morphology of these co-deposited Cu-Mo films. As the substrate temperature is increased, the surface interdiffusion length is increased and a transition from a VCM to RCM structure with an intermediate LCM structure was observed.

3.3.3 Deposition rate effects

Eq. 3.3 exhibits an inverse power relationship between the material flux, ν, and the interdiffusion length. As the rate of material being added to the growing film surface is increased, the time for the constituent atoms to interdiffuse is decreased before the next layer of material buries this material. Similar to the observation made on the Al-Si system presented by Fukutani et al. [30], the domain size in our Cu-Mo structures decreased at increasing deposition rates. The measured Cu-Mo domain sizes approximately follows a $1/\nu$ relationship as shown in Fig. 3.11.

While no change in morphology was observed for the range of deposition rates studied here, Eq. 3.3 suggests that change in morphology can be achieved through changes in the deposition rate. This relationship will be explored in future studies.

3.4 Mechanical Behavior of Bicontinuous Cu-Mo Thin Films Under Compression

The nanostructure of metallic thin films determines how they respond in extreme environments, including mechanical deformation [31]. For extensive information on

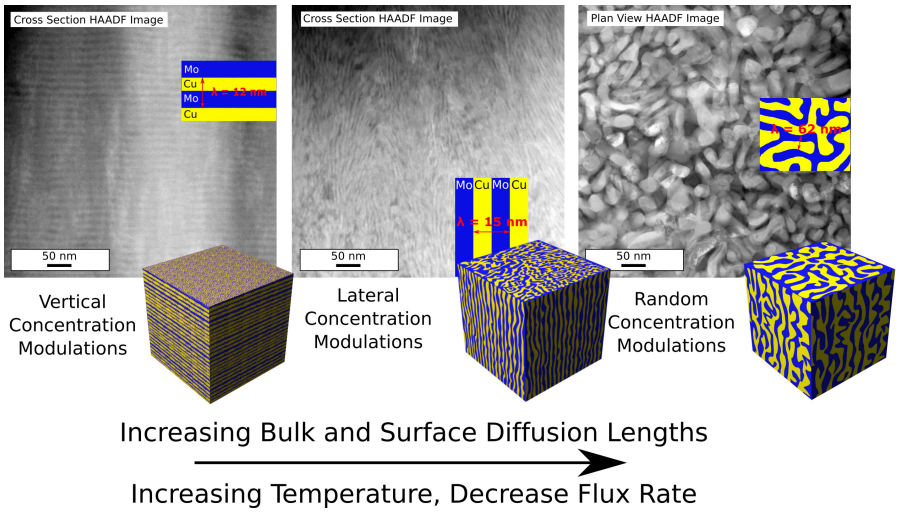

Figure 3.14: A 3D schematic of the evolution in morphology as a result of increasing interdiffusion length as a result of increasing substrate temperature. The co-deposited Cu-Mo system was observed to transition from the VCM to the LCM to the RCM structure as drawn.

the mechanical behavior of the thin films studied in this work please refer to the following studies: [32] and [33]. A summary of the mechanical response of the thin films described in this chapter follows.

Fig. 3.15 shows the true stress-strain curve for the three Cu-Mo nanocomposite morphologies. The methodology used to complete these mechanical experiments is described in Chapter 2.

The black curve shown in Fig. 3.15 represents the true stress and true strain for the Cu-Mo VCM morphology. High strength of approximately 3 GPa was observed in the sample under compression. Very limited ductility was observed in the sample as it failed suddenly like a brittle material. The VCM's mechanical response was very similar to the findings on the brittle-like behavior in multilayer thin films [34].

The LCM response to compressive loading is shown in the red curve of Fig. 3.15. Considerable hardening and ductility was observed with this morphology due to the short interface spacing and the bicontinuous Cu and Mo domains [32]. Yuchi *et. al.* remark that the initial load drop is due to the formation of a kink band in the sample. The enhanced ductility relative to the VCM morphology is due to the rotation of the Cu and Mo layers increasing the Schmid factor along the interfaces. This facilitates interfacial sliding and strain non-localization.

The blue curve in Fig. 3.15 represents the mechanical response of the RCM structure. This morphology exhibited a good combination of ultra-high hardness and significant ductility as compared to the VCM morphology. The enhancement

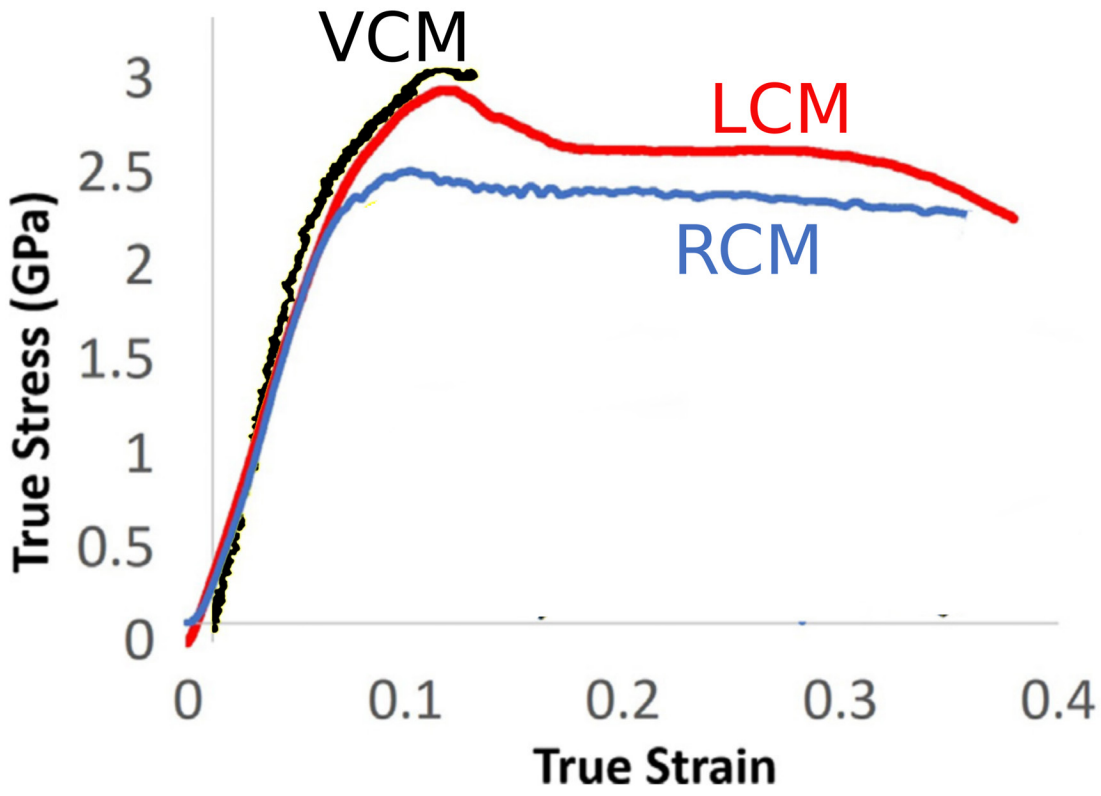

Figure 3.15: True stress-plastic strain curves measured from the nanopillar compression test. From Ref. [32].

in ductility is due to the tortuous topography of the interfaces [32]. Slip along the interface plane could only advance short distances before it encountered the Cu or Mo phases, where the Burgers vector must change in magnitude and oftentimes in direction [32].

3.5 3-D phase field simulations of self-organized composite morphologies in physical vapor deposited phase separating binary alloys

The proceding section is reproduced by permission from Professor Ankit Kumar from Ref. [35]. These simulations were conducted by Professor Ankit Kumar at The Arizona State University.

There have been several previous efforts to model the self-organization of microstructure morphology in vapor-deposited materials. Investigating co-deposition in Al-Ge films, Atzmon et al. [36] and Adams et al. [15] showed that the phase separation during film growth is regulated by a kinetic interplay of adatom mobility and deposition rate, which determines the distance an adatom can diffuse before being buried by the incoming atom flux. The authors also highlighted the importance of total interfacial energy in facilitating the LCM to VCM transition with increasing film thickness. One limitation of this work is that atomic mobility is non-zero only along the film surface. This "frozen bulk" approximation is reasonable for low substrate temperatures, where subsurface diffusion is limited. As mentioned before, the limitation of the frozen-bulk equation that the composition profile is underdetermined. However, at higher temperatures, the possibility that bulk diffusion may

modulate morphological self-assembly cannot be ruled out.

Lu et al. [25] performed 2D phase-field simulations to elucidate the influence of deposition rate and composition on phase separation as a function of both mobility and deposition rate. They did not adopt the frozen bulk approximation. In their study, a change from templated growth to uphill diffusion was suggested to be the primary mechanism by which the LCM to VCM transition occurs. However, their work could not reproduce RCM morphologies as these are inherently 3D structures and, therefore, cannot be captured by a 2D model. It is also not clear to what extent the structure of and transitions between LCM and VCM morphologies depend on the missing, third spatial dimension.

Similar to Lu et al. [25], we also adopt a phase-field model based on the classical Cahn-Hilliard equation16 to study the morphological evolution in cosputtered Cu-Mo. Simulated morphologies are compared to scanning and transmission electron microscopy (SEM and TEM) images obtained from co-deposited films. Morphological transitions from LCM to VCM are interpreted based on the lowering of total interfacial energy. The emergence of mixed morphologies that combine the characteristics of both LCM and VCM is reported. Deposition conditions under which compositionally enriched domains form RCM morphologies are also explored.

3.5.1 Results

Our simulations revealed four classes of distinct composite morphologies.

Lateral composition modulations (LCMs)

The LCM morphology was observed to evolve at low deposition rates, around $R = 0.1$ and $M = 0.5$. Film nanostructures exhibiting this morphology feature phase-separating domains that are Cu-rich or Mo-rich with domain boundaries aligned perpendicular to the flat substrate or parallel to the deposition axis (Z). This is demonstrated in Fig. 3.16 by the green isosurfaces, which indicate that the z-component of their normal vector is near zero and, therefore, parallel to that axis.

Cross-sectioning the simulated nanostructure perpendicular to the deposition axis reveals a lateral phase separation that imparts bicontinuous attributes along the x-y plane, as shown in Fig. 3.17. This implies that due to the slow deposition rates, every new layer is deposited well after the preceding layers have phase separated into Cu-rich and Mo-rich regions.

Consequently, the phase-separated morphology in each succeeding layer mimics that of the preceding layer, which may be viewed as acting as a template. The LCM morphology, as observed in our simulations, is validated by microstructural evidence of similar features observed in PVD Cu-Mo films, deposited at 1.2 nm/s and temperature of 600 °C as shown in Fig. 3.6.

To better understand how the feature size changes along the deposition axis, we plotted S as a function of the film thickness d in Fig. 3.17. We observed that the average feature size rapidly reaches a maximum value and then decreases with increasing film thickness. Thus, coarsening occurs in the lower layers as new layers

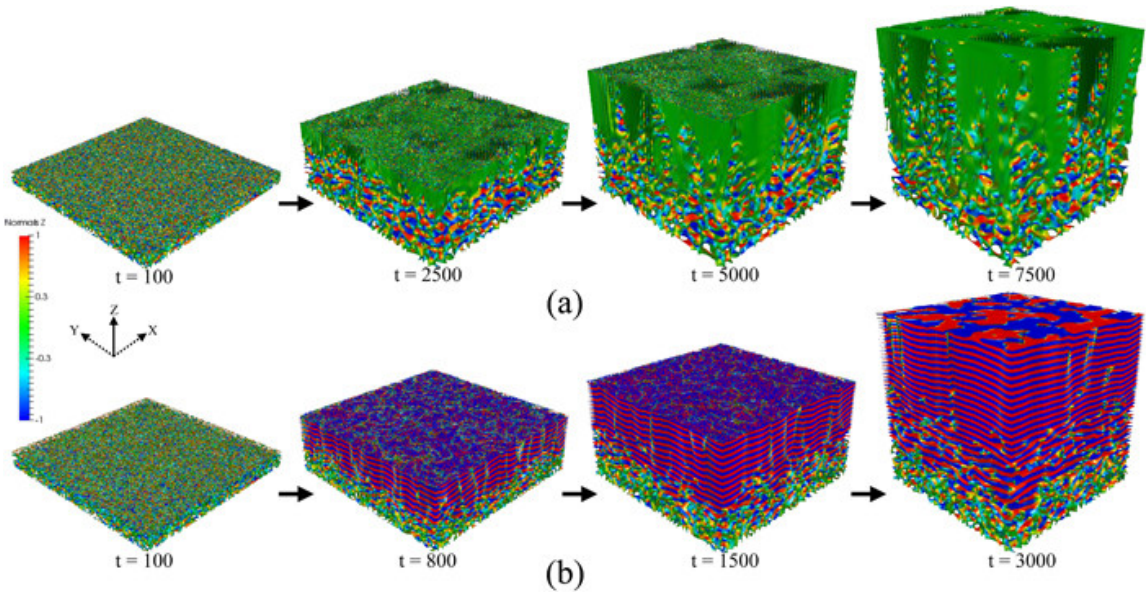

Figure 3.16: Morphological evolution of Cu-Mo films deposited at (a) $R = 0.1$ and (b) $R = 0.3$ starting from a random seed layer. Isosurfaces with $\psi = 0.5$ are shown colored by the z-component of the unit vector parallel to the gradient of the order parameter. Thus, surfaces that are colored in blue or red are perpendicular to the z-axis, while green ones are parallel to the z-axis. From Ref. [35].

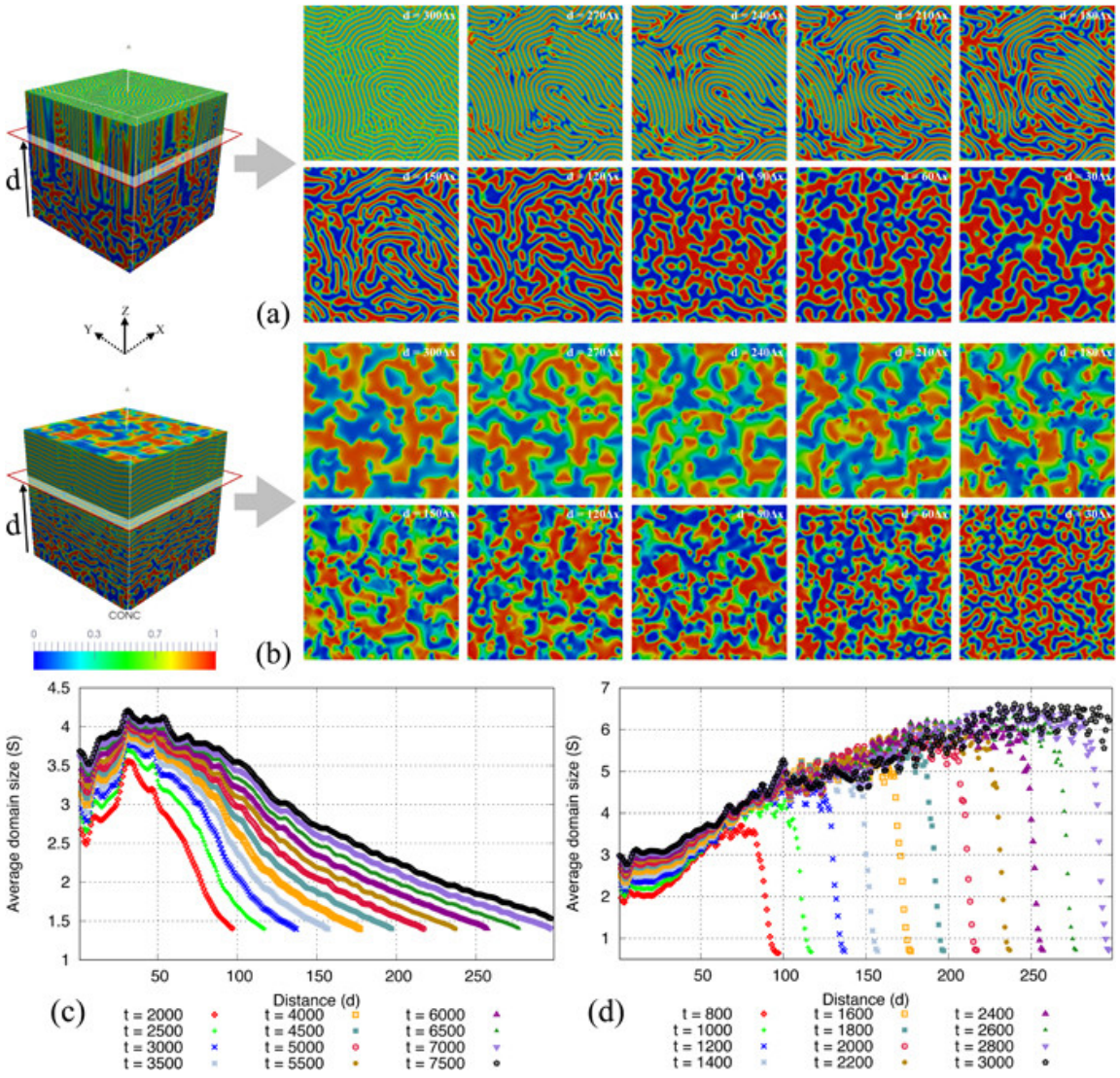

Figure 3.17: Variation of feature size visualized as a function of thickness, d, in the computationally deposited films with (a) LCM and (b) VCM, the temporal evolution of which is shown in Fig. 3.16. Average domain size, S, plotted as a function of d during the deposition of films with (c) LCM and (d) VCM. From Ref. [35].

are being deposited on the surface. Indeed, coarsening is observed at all locations within the film. However, the depth at which the peak value of S was observed remains constant with time.

Vertical composition modulations (VCMs)

At an increased deposition rate, around $R = 0.3$ and $M = 0.5$, the VCM morphology is found to be prevalent. Here, film nanostructures are characterized by phase-separating domains of Cu-rich and Mo-rich phases that are layered and modulate vertically along the deposition axis. The blue and red isosurfaces of a VCM morphology [Fig. 3.16] indicate that the domain boundaries are perpendicular to the deposition axis. Cross-sectioning the simulated nanostructure perpendicular to the deposition axis reveals alternating periodic layers of Cu-rich and Mo-rich phase domains. Experimental results of a layered morphology [Fig. 3.4] in a Cu-Mo physical vapor film deposition at 400 °C and deposition rate of 1.2 nm/s closely resemble the VCM morphology observed in our simulations.

The plot of feature size vs the film thickness [Fig. 3.17] showed that the average size of the Cu-rich and Mo-rich domains increased gradually and saturated to a maximum value. The maximum value corresponds to two uniformly spaced layers of the alternating phase domains. A steep decline near the top edge of the film is due to a very small feature size detected in an unseparated, freshly deposited layer.

In experiments, at a deposition rate of 1.2 nm/s, LCM to VCM transition occurs as the temperature is increased from 400 to 600 °C as shown in 3.2.2. Our phase-

field simulations for a range of deposition rates reveal a similar transition if mobility is increased. For example, under a constant deposition rate, $R = 0.2$, a decrease in the mobility from $M = 0.5$ to $M = 0.3$ leads to a change in the simulated film nanostructure from LCM to VCM.

Mixed morphology

At $R = 0.25$ and $M = 0.5$, the simulated nanostructures evolved to form a mixed morphology that exhibits attributes of both LCMs and VCMs. A cross-sectional view of the nanostructure perpendicular to the deposition axis, as shown in Fig. 3.18, displays an initial tendency to form VCMs, with a gradual transition to an LCM near the top.

Although mixed morphologies have not been observed experimentally, they are shown to exist, through simulations, all along the transition region between LCMs and VCMs, if M is not too low (i.e., > 0.1). The plot of mixed morphology in Fig. 3.18 showed an initial steep rise fol- lowed by saturation of domain size, indicating that the Cu-rich and Mo-rich phases form domains, mirroring the pattern found in VCMs. However, this was followed by a gradual drop in the domain size, which is due to the existence of unseparated layers close to the surface.

Random composition modulations (RCMs)

At smaller values of mobility $M(< 0.6)$, increasing the deposition rate beyond an M-dependent critical value led to the evolution of random composition modulations (RCMs). These are essentially a network of phase-separated Cu-rich and Mo-rich

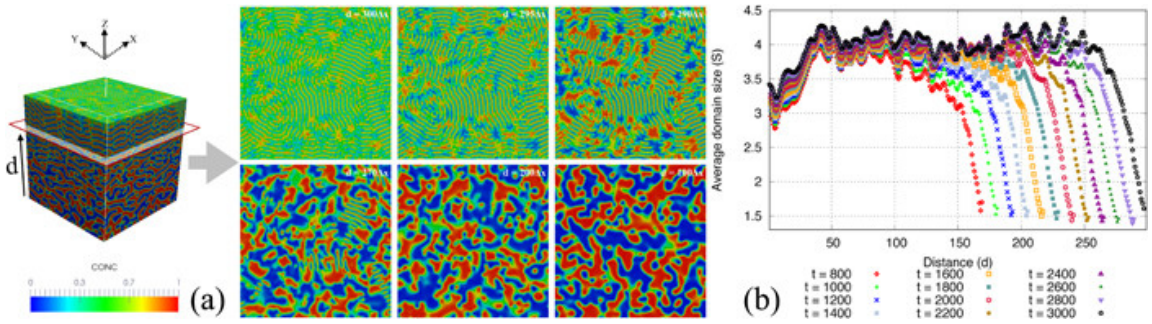

Figure 3.18: (a) Variation of feature size visualized as a function of thickness, d, in the computationally deposited films with a mixed morphology. (b) Average domain size, S, plotted as a function of d during the deposition of films with a mixed morphology. From Ref. [35].

domains that are bicontinuous and do not resemble either the LCMs or the VCMs, as shown in Fig. 3.19.

The reason why the Cu- and the Mo-rich phase-separated domains are unable to self-organize into a vertically- or laterally- aligned pattern may be attributed to a high value of R, which buries partially phase-separated morphologies before they are able to further re-organize. Plotting S vs. d shows an initial increase in the RCM characteristic length followed by a gradual decrease, as shown in Fig. 3.19. This is followed by a sharp decline in feature size when d approaches 260, signifying that the layers above this region are yet to decompose into Cu- and Mo- rich regions. Because the critical value of R, beyond which the deposited film failed to self-assemble into either of the LCM or VCM structures, was found to vary with M, the transition from VCM to an RCM morphology was simulated for a range of M.

3.5.2 Morphology maps

Based on the characterization of the physical vapor-deposited films, we developed an empirical morphology map as shown in Fig. 3.20.

The chosen axes are the two experimental levers used in this study, the deposition rate and the substrate temperature. The homologous temperature for each constituent is also indicated. It can be seen from the map that at a constant deposition rate of 1.2 nm/s the morphology transitions from VCM to LCM and finally to RCM at the highest substrate temperature, 800 °C. Isolated Cu grains are found to evolve at low temperature and deposition rate, while the feature size coarsens at

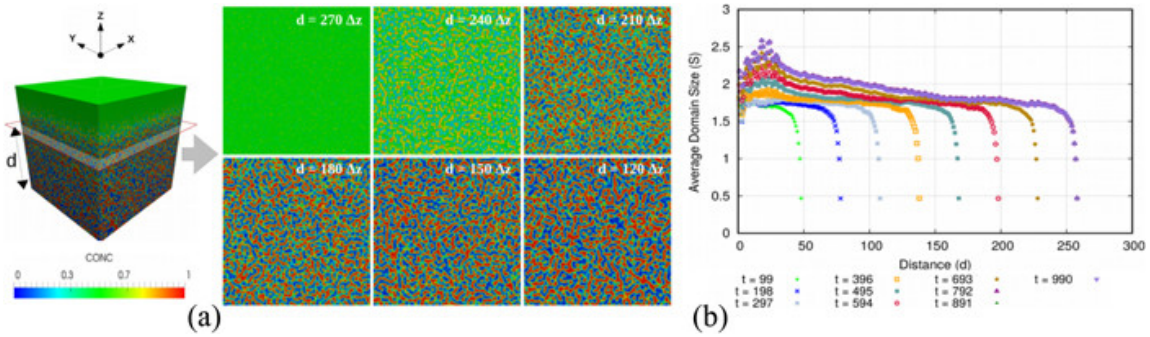

Figure 3.19: (a) Variation of feature size visualized as a function of thickness, d, in the computationally deposited films with random modulations (RCM). (b) Average domain size, S, plotted as a function of d during the deposition of films with RCM morphology. From Ref. [35].

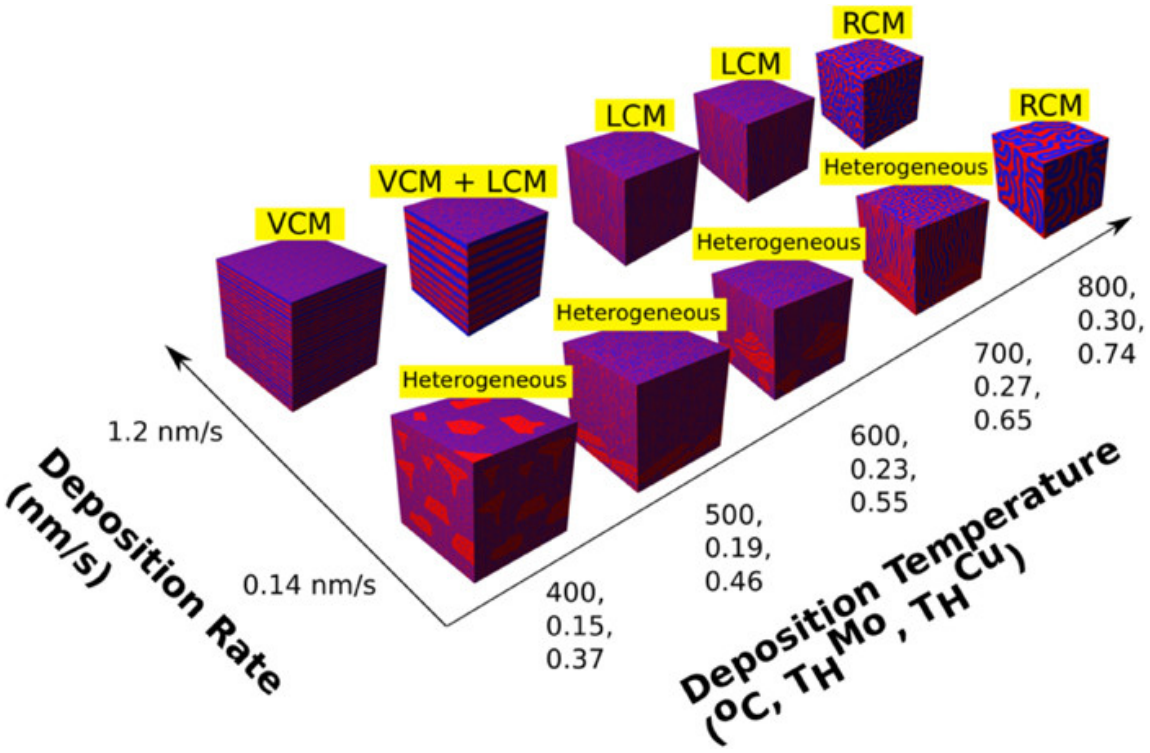

Figure 3.20: An empirical morphology map based on the data presented in Fig. 3.16 through Fig. 3.19 . The red regions represent concentrations of Cu and blue regions represent concentrations of Mo. The vertical axis is the combined (Cu + Mo) deposition rates used in this study. The substrate temperature horizontal axis includes the deposition temperature in relative Celsius scale and the homologous temperature of Mo and Cu, respectively. From Ref. [35].

higher temperatures. Heterogeneous microstructures are observed at low deposition rates, and the constituents on each length scale in this morphology also coarsened as the deposition temperature increased.

We now compare the observed morphological transitions with those simulated using the phase-field method. Phase-field simulations, unlike experiments, allow for a more extensive exploration of the deposition parameters and their influence on the film morphologies. Based on the simulations corresponding to various combinations of the deposition rate, R, and mobility, M, which increases monotonically with increasing substrate temperature, we were able to identify the processing parameters where VCMs, LCMs, RCMs, and the mixed morphology evolve. Our findings are summarized in the morphology map plotted in Fig. 3.21.

The formation of LCMs are favored at small R and M. Upon increasing R, the morphological transition into VCM is observed. However, there is a region sandwiched between VCM and LCM where the evolution of a mixed morphology is observed. Sharp transitions from LCM to VCM and VCM to RCM are observed at low temperature, but at higher temperatures, the transition to RCM occurs at larger R.

In comparing the simulated morphology map to the corresponding experimental results, we rely on the fact that mobility increases monotonically with increasing temperature. A quantitative mapping between mobility and temperature is not currently available for the Cu-Mo system. At constant temperature or mobility, and increasing deposition rate, the experiments did not reveal a transition in morphology,

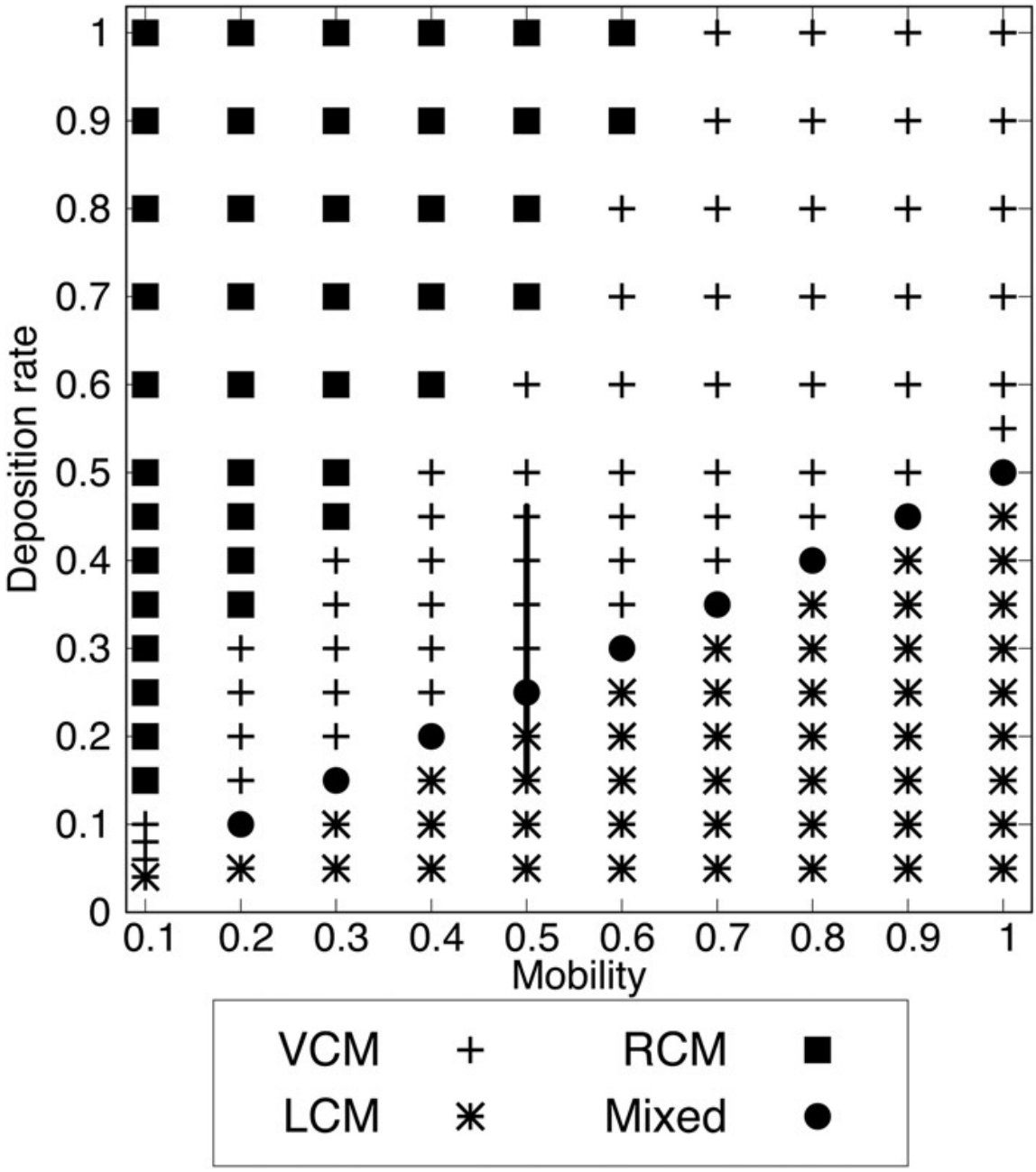

Figure 3.21: Morphology map generated by analyzing the computationally simulated binary film morphologies. The LCM to RCM transition that occurs upon anneal- ing at M = 10.0 is not shown on this map. The vertical line at M = 0.5 shows the range of deposition rates referenced in Fig. 12. From Ref. [35].

but instead a refinement in the length scale of the morphology. This is likely a result of experimental constraints as the range of deposition conditions is limited and a transitioning to a new morphology as deposition rate changes might not be within these limits. However, at constant deposition rate and changing mobility, or deposition temperature, we did observe the simulated transitions from the VCM to the LCM morphology with a mixed microstructure in between.

Our simulations predict RCM microstructures at high deposition rates and low mobilities. These microstructures are absent in the high deposition rate and low-temperature limit of our experiments. As before, we ascribe this discrepancy to the limited range of deposition rates accessible to us in this study. On the other hand, experiments did reveal the RCM morphology at the highest deposition temperature while the simulations did not. However, we find that the simulations do exhibit a transition from LCM to RCM morphology when the mobility and total simulation time are further increased. To demonstrate this transition, we simulated the evolution of an LCM microstructure over an extended time ($t = 80,000$) and under elevated mobility of $M = 10.0$. This simulation may be thought of as being analogous to a long-time, high-temperature annealing of a deposited film. The outcome, shown in Fig. 3.22, reproduced the LCM to RCM transition observed in experiments. As such, we reason this transition to an RCM morphology during deposition as an increase in contribution from bulk diffusion during processing. The necessarily high mobility in the phase field simulation required to form the RCM morphology

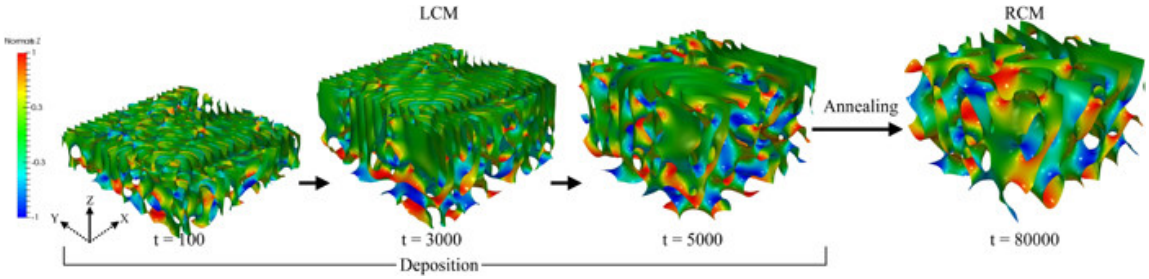

Figure 3.22: The first three images from the left show the evolution of the LCM morphology at R = 0.4. A subsequent extended simulation at elevated mobilitywhich may be seen as analogous to high-temperature annealingleads to the progressive breakup of the LCM morphology and the emergence of the RCM structure shown in the right- most image. From Ref. [35].

indicates this activation of bulk diffusion that is occurring during experimentation.

A similar transition was observed in the Al-Si system by Fukutani et al. [30]. Thus, we believe that the formation of RCM microstructures at high deposition temperatures occurs by the capillarity-driven breakup of the LCM morphology.

3.5.3 Self-organization mechanisms

In all LCM nanostructures that have been reported above, the interface between the phase-separated domains was found to be oriented parallel to the direction of deposition. For these cases, the vapor deposition rates were sufficiently slow such that by the time a fresh layer was deposited, the layer underneath had already phase-separated. Under such conditions, there is no scope for the concentration modulations to evolve along the direction of deposition as the unseparated freshly deposited layer is confined between the vacuum and the bulk film. Thus, the only possible diffusional pathway that remained was the top, unseparated surface of the film. Our findings based on phase-field simulations of LCMs are, therefore, in agreement with the frozen bulk approximation proposed by Atzmon *et al.* [36] and Adams *et al.* [15]. However, it is worth reiterating that this approximation was not assumed in any of our phase-field calculations.

To elucidate the mechanism of the LCM to VCM transition, we plotted the total interfacial volume fraction extracted from film nanostructures that were simulated at different R values for $M = 0.5$, as shown in Fig. 3.23.

It is apparent that as R is increased the interfacial energy of the evolving LCM

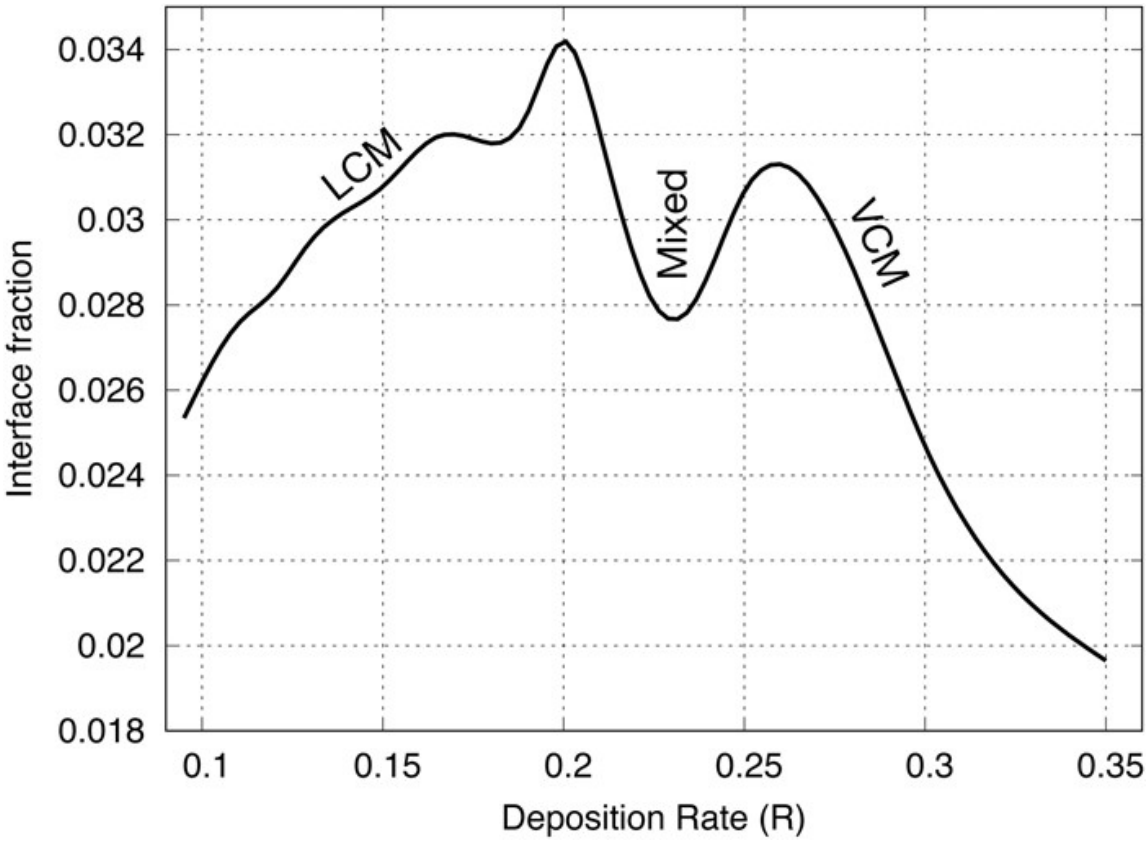

Figure 3.23: Interfacial volume fraction plotted as a function of deposition rate, R, corresponding to computationally simulated films for $M = 0.5$, along the vertical line in Fig. 3.22. To compute the interfacial volume fraction, the total number of grid points belonging to the diffuse interfaces that correspond to $\psi \in (0:01, 0:99)$ was normalized by the total number of grid points in the model, i.e., $300 \times 300 \times 300$. Peaks at $R = 0.2$ and 0.26 indicate the LCM-to-mixed and mixed-to-VCM transitions. From Ref. [35].

structure initially increases. Increasing the value of R further while preserving the LCM structure would require a further increase in the interfacial energy. As an alternative, the film self-assembles to a mixed morphology that enables a sudden drop in the interfacial energy, thereby rendering the LCM-to-mixed transition thermodynamically favorable. Upon further increasing R, the interfacial energy again increases before resuming a downward trend once the transition to VCM is complete. The VCM morphology has comparatively low interface energy, because the total interfacial area enclosed within the simulated domain is lower as compared to that of competing morphologies.

3.6 Conclusions

We observed concentration modulations in all of the deposited Cu-Mo films co-sputtered at elevated temperatures, with three different morphologies that are temperature-dependent. At the lowest temperature sampled, a nano-grained film exhibited vertical concentration modulations perpendicular to the substrate-film interface. At the intermediate temperature of 600 °C, the Cu and Mo exhibited semi-coherent FCC/BCC interfaces and exhibited lateral domains oriented along the film growth direction. At the highest temperature tested, the film developed into a fully random structure in which the phases displayed little organization. At constant substrate temperature and increasing deposition rate, the particular morphologies were maintained, but the domain dimensions were refined. We show that this evolution in morphology should be expected considering the competition between the surface

interdiffusion length and the rate of phase separation.

Our work has shown that the stress-strain response of a metallic nanocomposite can be tailored by manipulating its structure at nanoscale [32]. The three nanocomposites were observed to have a high strength above 2GPa [32]. A three-dimensional nanoscale bicontinuous morphology with semi-coherent interfaces exhibits high plastic deformability due to the ability of the structure to de-localize deformation [32].

References

[1] DOE. *Challenges at the Frontiers of Matter and Energy: Transformative Opportunities for Discovery Science*. United States. Dept. of Energy. Office of Basic Energy Sciences, 2015.

[2] B.A. Movchan and A.V. Demchishin. Structure and properties of thick condensates of nickel, titanium, tungsten, aluminum oxides, and zirconium dioxide in vacuum. *Fiz. Metal. Metalloved. 28: 653-60 (Oct 1969).*, 1969.

[3] D.P. Tracy and D.B. Knorr. Texture and microstructure of thin copper films. *Journal of Electronic Materials*, 22(6):611–616, 1993.

[4] J.A. Thornton. Influence of substrate temperature and deposition rate on structure of thick sputtered cu coatings. *Journal of Vacuum Science and Technology*, 12(4):830–835, 1975.

[5] N. Saunders and A.P. Miodownik. Phase formation in co-deposited metallic alloy thin films. *Journal of Materials Science*, 22(2):629–637, 1987.

[6] C.D. Adams, M. Atzmon, Y-T Cheng, and D.J. Srolovitz. Transition from lateral to transverse phase separation during film co-deposition. *Applied Physics Letters*, 59(20):2535–2537, 1991.

[7] S. Zhang, L. Ye, and J. Hou. Breaking the 10% efficiency barrier in organic photovoltaics: Morphology and device optimization of well-known pbdttt polymers. *Advanced Energy Materials*, 6(11):1502529, 2016.

[8] J.W. Gibbs. On the equilibrium of heterogeneous substances. *American Journal of Science*, 1(96):441–458, 1878.

[9] R.W. Balluffi, S.M. Allen, and W.C. Carter. *Kinetics of materials*. John Wiley & Sons, 2005.

[10] J.W. Cahn. On spinodal decomposition. *Acta Metallurgica*, 9(9):795–801, 1961.

[11] J.W. Cahn and J.E. Hilliard. Spinodal decomposition: A reprise. *Acta Metallurgica*, 19(2):151–161, 1971.

[12] C-K Wu. Lattice imaging and mechanical properties of a cu-ni-cr spinodal alloy. *escholarship.org*, 1976.

[13] J.W. Cahn. The kinetics of cellular segregation reactions. *Acta Metallurgica*, 7(1):18–28, 1959.

[14] J.A. Venables and G.D.T. Spiller. Nucleation and growth of thin films. In *Surface Mobilities on Solid Materials*, pages 341–404. Springer, 1983.

[15] C.D. Adams, M. Atzmon, Y.T. Cheng, and D.J. Srolovitz. Phase separation during co-deposition of al–ge thin films. *Journal of Materials Research*, 7(3):653–666, 1992.

[16] J. Grandidier, D.M. Callahan, J.N. Munday, and H.A. Atwater. Light absorption enhancement in thin-film solar cells using whispering gallery modes in dielectric nanospheres. *Advanced Materials*, 23(10):1272–1276, 2011.

[17] P.R. Subramanian and D.E. Laughlin. The cu-mo (copper-molybdenum) system. *Bulletin of Alloy Phase Diagrams*, 11(2):169–172, 1990.

[18] C.D. Adams. *Phase Separation During Thin Film Co-deposition*. PhD thesis, University of Michigan, 1992.

[19] B. Derby, Y. Cui, J.K. Baldwin, and A. Misra. Effects of substrate temperature and deposition rate on the phase separated morphology of co-sputtered, cu-mo thin films. *Thin Solid Films*, 647:50 – 56, 2018.

[20] T.P. Harzer, S. Djaziri, R. Raghavan, and G. Dehm. Nanostructure and mechanical behavior of metastable cu–cr thin films grown by molecular beam epitaxy. *Acta Materialia*, 83:318–332, 2015.

[21] H. Abrams. Grain size measurement by the intercept method. *Metallography*, 4(1):59–78, 1971.

[22] J.W. Cahn and J.E. Hilliard. Free energy of a nonuniform system. i. interfacial free energy. *The Journal of Chemical Physics*, 28(2):258–267, 1958.

[23] Y. Yen, Y. Kuo, J. Chen, C. Lee, and C. Lee. Investigation of thermal stability of mo thin-films as the buffer layer and various cu metallization as interconnection materials for thin film transistor–liquid crystal display applications. *Thin Solid Films*, 515(18):7209–7216, 2007.

[24] C.M. Müller, A.S Sologubenko, S.S.A Gerstl, and R. Spolenak. On spinodal decomposition in cu–34 at.% ta thin films–an atom probe tomography and transmission electron microscopy study. *Acta Materialia*, 89:181–192, 2015.

[25] Y. Lu, C. Wang, Y. Gao, R. Shi, X. Liu, and Y. Wang. Microstructure map for self-organized phase separation during film deposition. *Physical Review Letters*, 109(8):086101, 2012.

[26] G. Krishnan, M.A. Verheijen, H. Gert, G. Palasantzas, and B.J. Kooi. Tuning structural motifs and alloying of bulk immiscible mo–cu bimetallic nanoparticles by gas-phase synthesis. *Nanoscale*, 5(12):5375–5383, 2013.

[27] Y. Chen, Y. Liu, C. Sun, K.Y. Yu, M. Song, H. Wang, and X. Zhang. Microstructure and strengthening mechanisms in cu/fe multilayers. *Acta Materialia*, 60(18):6312–6321, 2012.

[28] A.R. Denton and N.W. Ashcroft. Vegards law. *Physical Review A*, 43(6):3161, 1991.

[29] R.J. Livak and G. Thomas. Loss of coherency in spinodally decomposed cu-ni-fe alloys. *escholarship.org*, 1973.

[30] K. Fukutani, K. Tanji, T. Saito, and T. Den. Fabrication of well-aligned al nanowire array embedded in si matrix using limited spinodal decompositon. *Japanese Journal of Applied Physics*, 47(2R):1140, 2008.

[31] M. Ohring. *Materials science of thin films*. Elsevier, 2001.

[32] Y. Cui, B. Derby, N. Li, and A. Misra. Design of bicontinuous metallic nanocomposites for high-strength and plasticity. *Materials & Design*, 166:107602, 2019.

[33] Y. Cui, B. Derby, N. Li, N.A. Mara, and A. Misra. Suppression of shear banding in high-strength cu/mo nanocomposites with hierarchical bicontinuous intertwined structures. *Materials Research Letters*, 6(3):184–190, 2018.

[34] A. Misra, J.P. Hirth, and R.G. Hoagland. Length-scale-dependent deformation mechanisms in incoherent metallic multilayered composites. *Acta Materialia*, 53(18):4817–4824, 2005.

[35] K. Ankit, B. Derby, R. Raghavan, A. Misra, and M.J. Demkowicz. 3-d phase-field simulations of self-organized composite morphologies in physical vapor deposited phase-separating binary alloys. *Journal of Applied Physics*, 126(7):075306, 2019.

[36] D.A. Atzmon, M.and Kessler and D.J. Srolovitz. Phase separation during film growth. *Journal of Applied Physics*, 72(2):442–446, 1992.

CHAPTER IV

Heterogeneous Phase Separation in Binary, Cu-Mo Thin Films

4.1 Introduction

Abrupt changes in the external conditions can force systems into nonequilibrium states. These systems kinetic relaxation pathways are often complex and involve phase transitions that may lead to multiple metastable phases. Understanding phase-ordering kinetics is central to controlling the way in which phases organize in a number of material systems [1], particularly in vapor deposited thin films where control of grain [2] or multi-phase [3] morphology is crucial to obtaining novel and enhanced functionalities for technological application [4].

Given the unique governability over the deposition temperature and rate, physical vapor deposition (PVD) has often been the synthesis technique of choice to study phase separation in immiscible systems [5–8]. Furthermore, unlike bulk phase separation in which the systems bulk thermodynamics dictates the rate of phase separation, PVD allows external control over the rate of separation through the deposition rate,

at a given temperature [9]. In this article, we report on a novel PVD synthesis route that dictates dramatic differences in constituent mobilities of Cu and Mo during co-sputtering and results in far-from-equilibrium, metastable, multimodal architectures during deposition.

Normally, there are two processing routes that can be used to create and study multi-phase morphologies using PVD sputtering: low temperature deposition to produce an amorphous film followed by annealing [10] or deposition at elevated temperature [11]. In the case of the former approach, a binary alloy which is highly immiscible is co-sputtered. Sluggish kinetics during deposition of immiscible alloys at room temperature has been shown to result in a chemically homogeneous amorphous film [6]. Annealing the samples at elevated temperature induces phase separation as a result of nucleation and growth or spinodal decomposition depending on the system [12–14]. This generally results in randomly oriented concentration modulations of the two constituents in a bicontinuous morphology if the constituents are of equal phase fraction.

Another processing route involves co-sputtering each immiscible element while heating the substrate. At temperatures high enough to activate phase separation during deposition, constituents self-organize into concentration modulations that are oriented in different directions based upon the deposition conditions [9, 11]. The interplay between the rate of phase separation and the rate of deposition determine the final morphology. Laterally, vertically, and randomly oriented concentration

modulations have resulted by controlling the substrate temperature. Phase field simulations have confirmed this self-organizing behavior [5].

In both synthesis routes, the resulting morphologies possess a single concentration modulation wavelength with phase separated domains oriented laterally, vertically, and randomly with respect to the substrate [5]. The challenge is to deposit a film with phase separation at multiple length scales forming a hierarchical structure. The current work addresses this challenge by deliberately depositing immiscible constituents, Cu and Mo chosen as the model system, at low deposition rates and high temperatures. The high temperature activates self- assembly via phase separation during deposition as has been shown before, while the low deposition rate creates a large disparity in mobility between the sputtered species assembling on the growing surface.

With differences of orders of magnitude in adatom mobility of the constituents [15, 16], heterogeneous structural evolution results in a bimodal architecture with Cu-rich and Mo-rich domains stabilizing at multiple length scales and undergoing further separations within each domain to produce pseudomorphic – or lattice-mismatched metastable phase – crystal structures that do not correspond to the bulk ground state of the constituent elements, namely BCC Cu and FCC Mo. Further, we altered the substrate temperature to coarsen the hierarchical morphology and change the crystal structure of the domains. Finally, we utilize cluster expansion formalism, parameterized with density functional theory (DFT) calculations to investigate

the phase stability of metastable Cu and Mo domains given the constraints of the system. Compression tests performed *in-situ* in a transmission electron microscope (TEM) show unprecedented mechanical behavior of extensive plastic deformability at room temperature at flow stress in excess of 2 GPa. This study provides new insights for bottom-up design of nanometallic architectures with high strength and high deformability.

4.2 Experimental Observations: Hierarchical, pseudomorphic Cu-Mo Morphologies at Multiple Length Scales

4.2.1 CuMo hierarchical structure and characterization

The morphology, including chemistry and crystal structure, of a co-deposited CuMo film at relatively low deposition rate of 0.12 nm/s is shown in Fig. 4.1. In HAADF phase contrast imaging, it was observed that these samples exhibited morphological features on at least two different length scales.

At low magnification, relatively large Cu-rich domains in the darker contrast of approximately 100 nm in lateral and vertical dimension were interspersed in a CuMo bicontinuous matrix. These faceted Cu-rich domains were homogeneously distributed through and across the thickness of the film as shown. The chemical composition of these domains were approximately 95 at.% Cu as measured by EDXS. The bicontinuous matrix maintained an approximate 45 at.% Cu composition as measured by EDXS and thus, Cu species were not removed from the matrix to form these large Cu-rich domains and abnormal grain growth can be ruled out as a cause

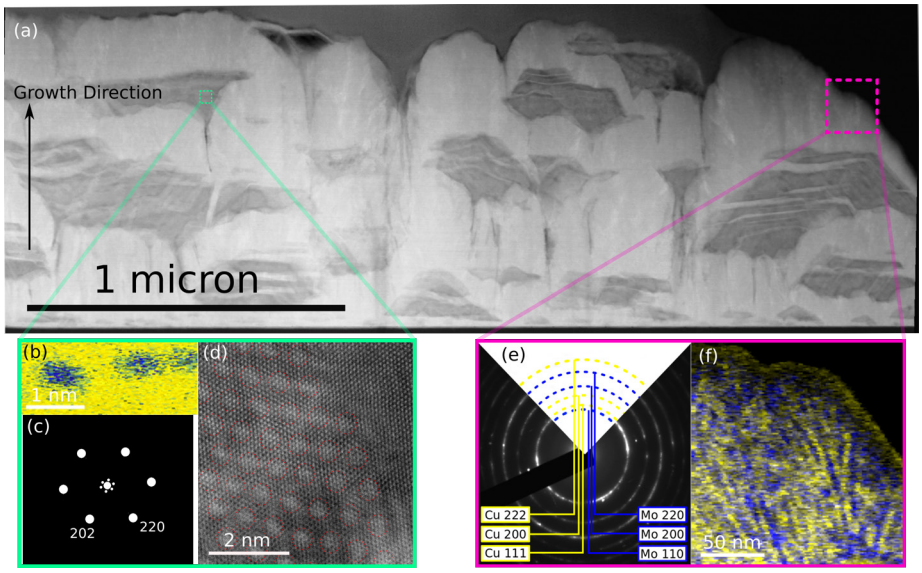

Figure 4.1: High-angle annular dark-field scanning transmission electron microscopy (HAADF-STEM) images of the sample deposited at 400°C and 0.12 nm/s taken along the [111] direction of FCC Cu. The high-level view of the sample in (a) displays the hierarchical structure of the sample throughout the thickness and length of the film. Direction of growth is from bottom to top in the image. At one length scale in (b-d), the single crystal Cu grains contain FCC Mo dispersoids arranged in an FCC superlattice as indicated in the power spectrum (c) taken from (d); indexed down the FCC [111] zone axis. The energy dispersive X-ray spectrum map in (b) shows a concentration of Mo corre- sponding to the brighter spots in the STEM image. Another length scale is presented in (ef) where Cu and Mo are constrained to a coherent BCC (Mo)-(Cu) and exhibit lateral concentration modulations with respect to the film- substrate interface. (e) shows an SADP from the bicontinuous region and only BCC Mo frequencies are present, but CuMo concentration modulations are observed in the EDXS mapping in (f). From Ref. [19].

of this growth, even though Cu in this structure has a mobility advantage compared to Mo [15, 16]. The origin of these large Cu-rich domains is instead from a modified Volmer-Weber thin film growth mechanism. In the Volmer-Weber growth mode, the adatom cohesion is stronger than surface adhesion and forms 3D adatom cluster or islands [17, 18]. The dramatic difference in mobility of Cu compared to Mo leads to inhomogeneous agglomeration in the growing film as the more mobile Cu readily coalesces compared to the Mo, which lags behind in surrounding, smaller clusters.

Probing the large Cu-rich domains in HAADF imaging at high magnification showed that these islands exhibited the bulk ground state crystal structure of FCC Cu. However, regions of periodically distributed Mo nano-particles were observed throughout each of the Cu- rich grains. Fig. 4.1(b) shows an EDXS mapping of the Cu-rich matrix in yellow and agglomerations of Mo-rich particles in an ordered FCC superlattice arrangement. FFT analysis shown in Fig. 4.1 (c) taken from the high magnification HAADF image in Fig. 4.1(d) shows bulk FCC Cu frequencies in the $< 110 >$ direction. Interestingly, FCC Mo spots are present in the FFT pattern as well, but tightly surrounding the center spot. These are frequencies from the ordered Mo nanoparticles within the Cu-rich matrix encircled in Fig. 4.1(d).

Previously, Mo has only been found to exist in an FCC state under high pressures [20]. However, our DFT-parameterized cluster expansion calculations described below have shown that the FCC (Mo) does have a low energy metastable state at compositions close to the Mo-end of the composition rage, which is consistent with

what we observe here. The ordered arrangement of Mo particles formed an FCC superlattice within the Cu-rich domains. This superlattice is not unlike those found in ultra-thin metallic multilayers and quantum dots [21, 22]. In our case, insufficient mobility in the Mo atoms results in them becoming trapped within the Cu- rich domains, preventing their agglomeration into larger precipitates. Critical accumulation of Cu leads to island nucleation and growth whereas regions with slightly less Cu and more Mo phase-separate into lateral concentration modulations.

At a larger length scale, the matrix surrounding the Cu-rich domains was observed to have a bicontinuous morphology with lateral Cu-rich and Mo-rich sheets extending from the substrate to the top surface of the film. The selected area diffraction pattern (SADP) shown in Fig. 4.1(e) only shows frequencies from the BCC Mo crystal structure. EDXS analysis of the matrix shows the presence of Cu-rich and Mo-rich domains with a lateral morphology that extend into the thickness of the film as sheets. High-resolution imaging of the bicontinuous matrix shows a coherent structure where Cu has stabilized into a metastable BCC (Cu) crystal structure and taken on the BCC Mo lattice parameter. A high magnification image of these Cu and Mo-rich domains can be in Fig. 4.2.

This has been shown before in Ti/Al [23], Cu/Nb [24], and Mg/Nb [25] multilayers where absolute length scale of the structure and the relative thickness of the individual layers have given rise to metastable structures. A plan-view image of the sample is shown in Fig. 4.3.

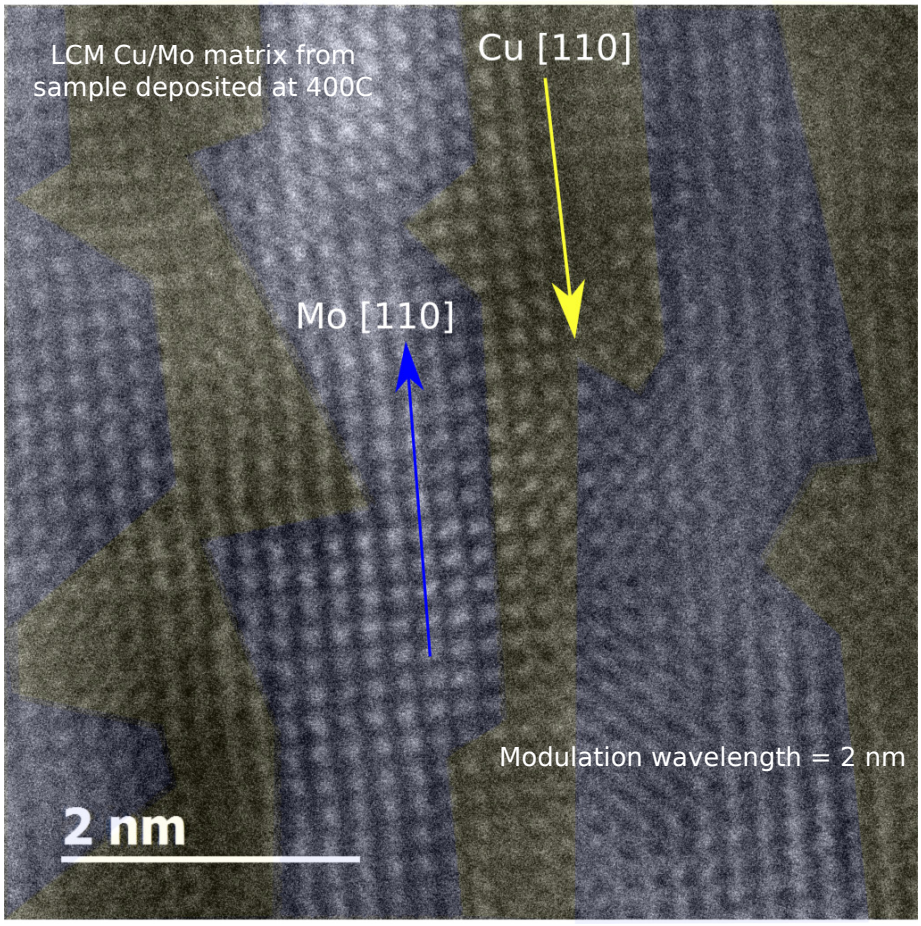

Figure 4.2: Highly magnified STEM image of BCC (Cu)-(Mo) composite matrix. At small length scales, BCC Cu is energetically favored to better fit the substrate lattice. Coherent BCC lateral concentration modulations formed the matrix of the Cu-Mo hierarchical structure surrounding the large Cu-rich domains. The scale of the Cu-rich domains – highlighted in yellow – is approximately 1 nm in lateral dimension and extend into the film as sheets and towards the surface of the film as rods. This is a view of the sample in plan-view. The direction of thin film growth is out of the page. From Ref. [19].

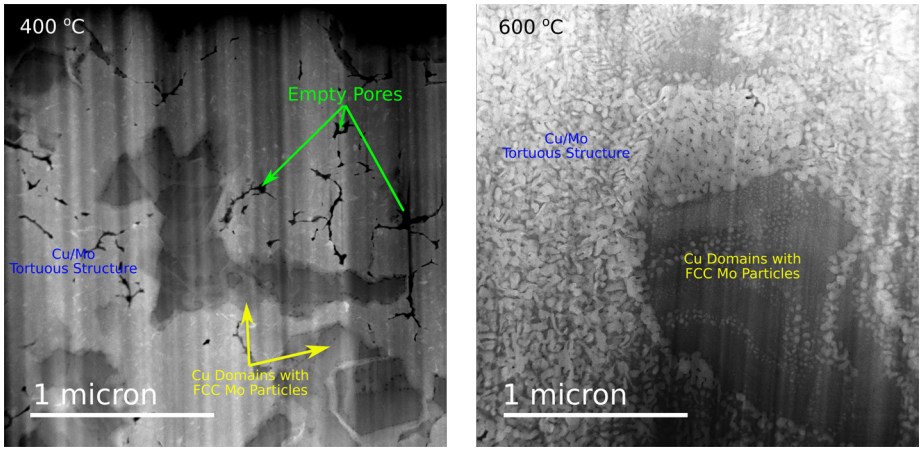

Figure 4.3: Plan-view images of the Cu-Mo hierarchical structure. (a) At 400 °C, the Cu-rich domains (darker regions) are scattered throughout the sample and surrounded by a crystallographically coherent, but chemically separated Cu-Mo lateral concentration modulations. In plan-view, the Cu-Mo domains are randomly organized and so the Cu-Mo domains are not columnar, but instead sheets that extend into the thickness of the film. The pure black regions of the image are pores in the sample. (b) At 600 °C, the structure at all length scales have coarsened. BCC Mo particles are observed in the Cu-rich domains (darker regions; bottom right) beginning at 600 °C. There are only two contrasts in this image: dark = Cu; bright = Mo. Scale bar, 200 nm. From Ref. [19].

This ordered structure has been discovered before in our work on CuMo [11] and other reports on AlSi systems [8], where the rate of deposition is slower than the rate of phase separation of the growing surface. This difference in rates allows for the formation of a phase separated template where each domain is at its terminal composition and subsequently deposited layers diffuse to like domains underneath [8, 11].

4.2.2 Equilibrium structures at higher deposition temperatures

Coarsening of the structures at all lengths scales was observed when Cu and Mo was deposited at higher substrate temperatures. At 600 °C, as shown in Fig. 4.4(a), the Cu-rich domains have expanded to approximately 200 nm in both the lateral and horizontal dimension.

The spacing between the Cu-rich domains has also increased. As shown in Fig. 4.4, the frequency of observable, periodic FCC Mo particle domains also increased. The most striking morphology change was the lateral concentration modulations that comprised the matrix. The chemical separation of the Cu- and Mo- rich domains was maintained at the higher temperature as compared to the sample deposited at 400 °C, but the two-fold increase in length scale in the Cu-rich domains no longer support a coherent BCC (Mo), BCC (Cu) crystal structure. Instead, the Cu- rich domains have crystallographically transformed into their bulk FCC Cu phase as shown in Fig. 4.4(b). The inter- face was observed as semi-coherent with the KurdjumovSachs orientation relationship, Cu(111)//Mo(110) and Cu<110>//Mo<111> . This is similar

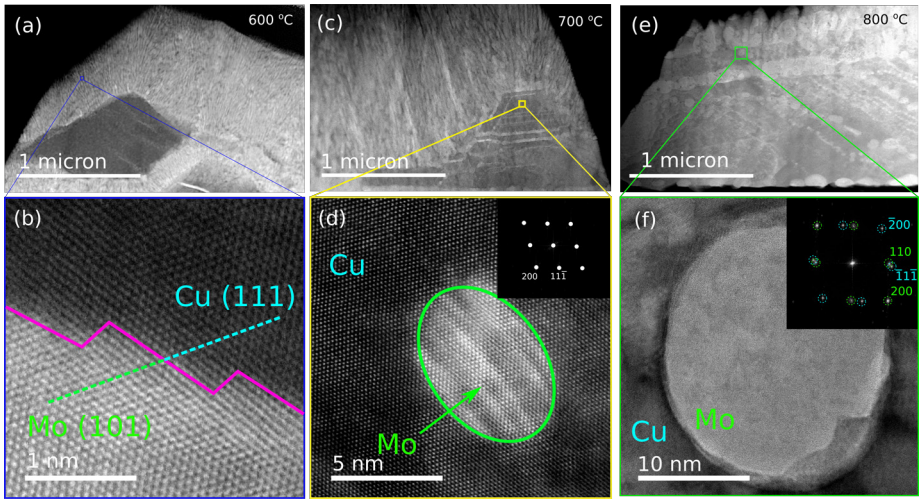

Figure 4.4: HAADF-STEM image of a CuMo film under the same conditions as in Figure 1, but deposited at 600C. The sample exhibits coarsening of all features and the phase separated matrix exists as BCC Mo and FCC Cu. (b) A highly magnified HAADF image showing the CuMo interface in the bicontinuous region. A KS orientation relationship was present. (c) At a substrate temperature of 700C further coarsening was observed and the larger Cu grains still contain FCC Mo particles, but each particle is much larger and are no longer arranged periodically. One of these particles is magnified in high resolution in (d) with the corresponding FCC [011] FFT pattern in the inset. Scale bar, 10 nm. For a CuMo sample deposited at 800 C as shown in (e), the features are again coarser. Only coarser BCC Mo particles were present in the Cu grains, one of which is shown in (f). From Ref. [19].

to Cu/Nb multilayers although oriented 90 degrees in relation to the substrate/film interface [5].

At 700 °C, further coarsening was observed as seen in Fig. 4.4(c). Interestingly, the periodicity of the FCC Mo particles was no longer observed. Rather, larger FCC Mo domains were found throughout the Cu-rich islands as if the Mo domains observed at lower substrate temperatures have coalesced as shown in Fig. 4.4(d). Even at the higher substrate temperature and larger size, the crystal structure of the Mo domains are still in the metastable FCC phase.

However, another crystallographic transformation occurred for the Mo particles at 800 °C as shown in Fig. 4.4(e) and Fig. 4.4(f). For substrate temperatures up to 700 °C, the (Mo) particles varied in size but maintained the metastable FCC crystal structure. There was a small density of equilibrium BCC (Mo) at this temperature. It was observed that only Mo particles above 8 nm were in the BCC phase. At 800 °C, most of the Mo agglomerates existed as larger particles, and have fully formed into the bulk BCC Mo state. The density of FCC vs. BCC Mo particle size and density are plotted in Fig. 4.5.

To obtain the density we measured the thickness of the TEM foil using EELS and then counted the number of particles in a given image with certain X and Y dimensions. We measured no BCC Mo in the Cu grains until 700 °C. The density of BCC Mo was still very small com pared to the FCC Mo even at at this temperature. At 800 °C, the density of stable BCC Mo particles increase dramatically. The size of

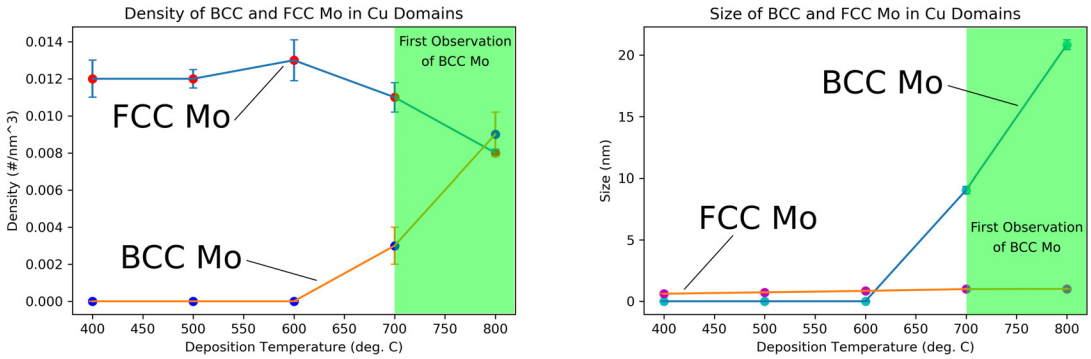

Figure 4.5: Density of FCC vs. BCC Mo particle size and density as a function of deposition temperature. A transition away from the metastable FCC Mo particles occured at 600 °C. A majority of equilibrium BCC Mo particles was observed starting at 800 °C. From Ref. [19].

each Mo structural polymorph trended linearly with increasing deposition temperature. As aforementioned, the size of the BCC Mo particles were no smaller than approximately 5 nm. This is much larger than the approximately 1 nm FCC Mo particles.

4.3 Calculations of Cu-Mo Phase Stability

We used the cluster expansion (CE) formalism [26–28] to parameterize the energetics of FCC- and BCC-based lattice alloys between Cu and Mo (as well as other Cu- refractory element pairs, as reported in supplementary information). Formally, a CE is defined by assigning occupation variables (with integer values), σ_i, to each site of a lattice that has configurational degrees of freedom, i.e. where more than one species can occupy a lattice site. Using this framework, we proceeded to explore the ground state of the FCC and BCC CuMo systems by systematically enumerating different occupancy configurations within an underlying FCC/BCC motif. Fig. 4.6 shows the results of these investigations. In these plots the Y axis represents the energy per spin. We are using a lattice model that reduces to a spin model with spin up and spin down corresponding to occupancy by species A/B respectively. Energy of each configuration is normalized by the number of spins. The legend is defined as follows:

1. Structure energies: these are the energies of each of the structures considered in the exploration of the configuration space. Each structure is defined in terms of a configuration of spins.

2. Ground state: these are the structures that belong to the convex hull, i.e. are most stable at each composition.

3. Random energies: this is the energy of a random configuration as per a model fitted against the structural energies calculated here. Essentially, the model is based on the cluster energy model, assuming perfectly random configurations.

Fig. 4.6 is notable in many respects. First of all, our investigation of the ground state in the case of the FCC Cu/Mo system suggests that Cu and Mo are actually miscible when the system is restricted to exist in the FCC state throughout the entire composition range. More specifically, the calculations show that the system undergoes a transition from endothermic to exothermic mixing as the system becomes richer in Mo. The calculations even suggest a high exothermic state at compositions close to a Mo-rich composition of $x = 5/6 = 0.83333$. At this composition, the system undergoes a LRO transformation and the ordered compound has an energy of formation relative to pure Cu and Mo in the FCC state of 200 meV/spin or close to 20 kJ/mol-atom. In the case of the BCC Cu/Mo system, on the other hand, the calculated energies of formation for configurations across the entire composition range suggest instead a tendency towards immiscibility, with a maximum energy of mixing of approximately +150 meV/spin or +15 kj/mol-atom. Notably, in this case there are configurations that exhibit ideal mixing (and to some degree exothermic

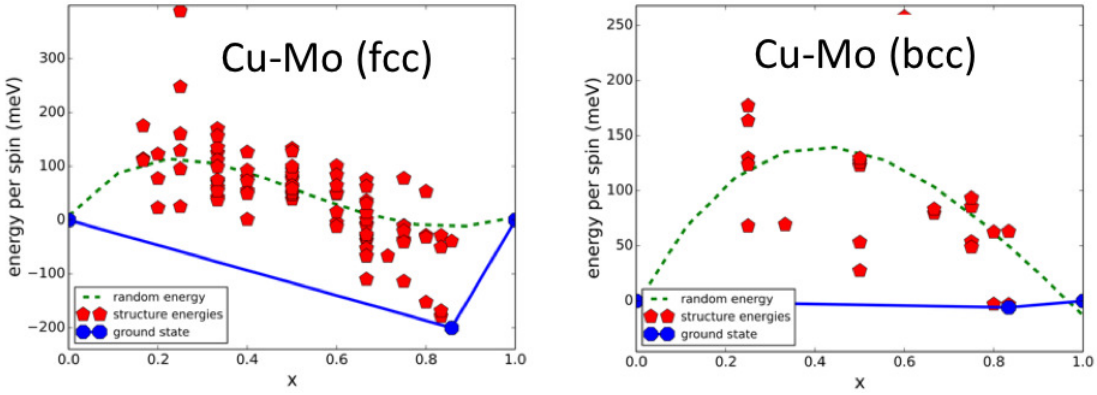

Figure 4.6: Plots of the energy per spin in meV versus the mole fraction of Mo (x) in a CuMo FCC system in the ground state.The calculations suggested a high exothermic state at compositions close to x = 5/6 = 0.83. The right image shows the same calculations for a CuMo BCC system where immiscibility is preferred. The legend is defined in the text. From Ref. [19].

tendencies) at compositions close to $x = 5/6 = 0.83333$, where x is the composition of Mo in the alloy.

These results are remarkable no type of constraint was imposed on the system, other than preserving the underlying FCC/BCC lattice. Each configuration, as stated above, was allowed to relax towards a (local) equilibrium, so the stabilization of a highly exothermic configuration in FCC CuMo at $x = 0.83333$ cannot be ascribed to coherency constraints of any kind. Liu and Zunger [29, 30] have shown how such constraints can lead to ordering in systems intrinsically immiscible in the bulk. Thus, contrary to what one might infer from the bulk phase diagram, Cu and Mo are at least partially miscible in the FCC state. The question then arises as to the reason for the observed immiscibility in the phase diagram. While a full phase stability analysis is beyond the scope of this work, the most likely explanation is the fact that the BCC-Mo state is very stable and the most stable tie-line between the Cu- and Mo-rich phases in this system are shared by a Cu-FCC and a Mo-BCC state, as shown schematically in Fig. 4.7.

To rule out any systematic issue with the calculated energetics for this system, we proceeded to investigate the alloying behavior in other Cu-refractory metal (RM) systems (CuNb, CuTa, and CuW) in the FCC state. As can be seen in Fig. 4.7, in all of these systems, similar asymmetric trends in which the system goes from immiscible to miscible as the amount of RM increases can be observed.

Any systematic error in the DFT calculations or the CE-based search is thus ruled

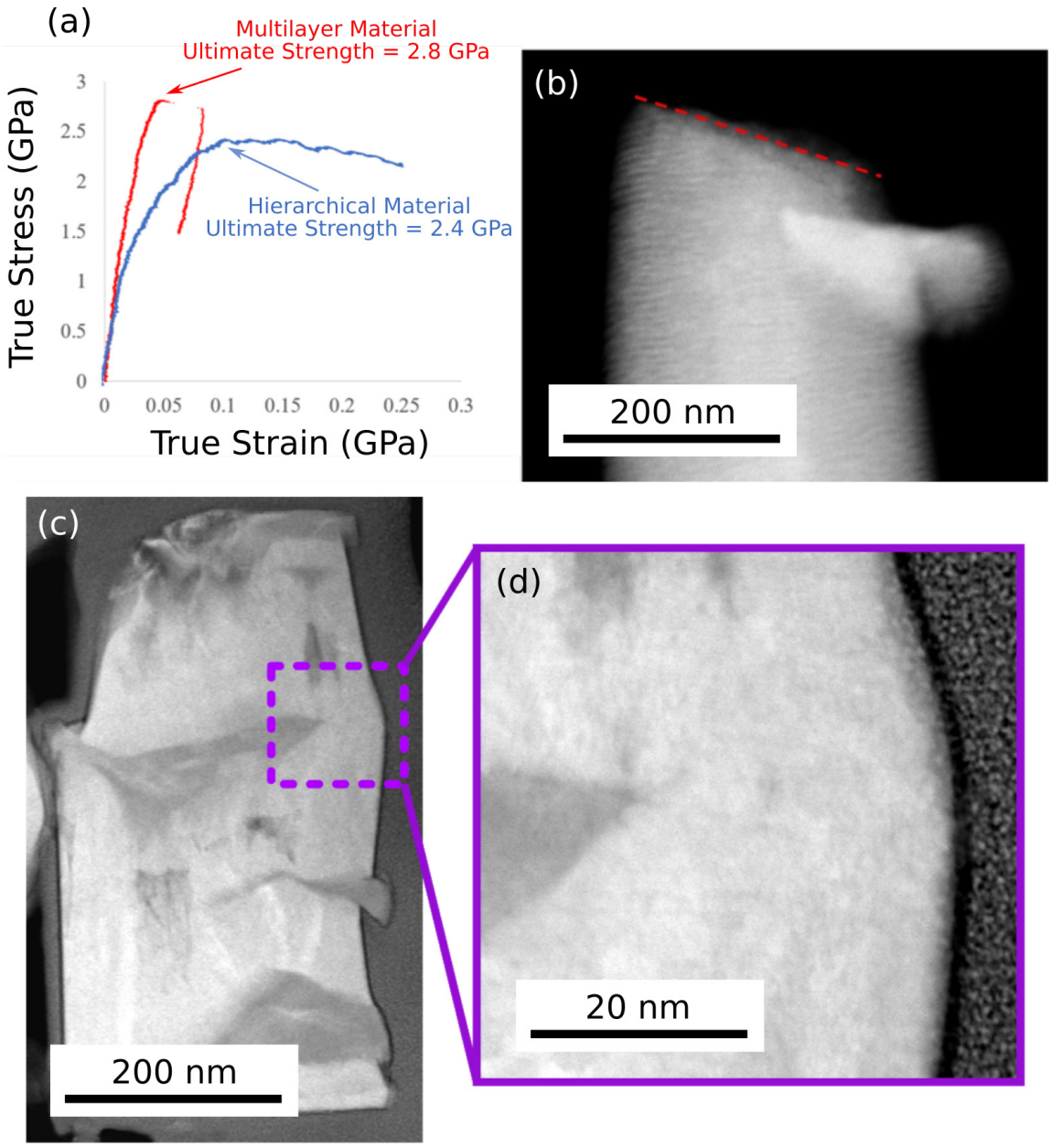

Figure 4.7: Schematic of phase stability competition between the FCC and BCC states in the CuMo system. From Ref. [19].

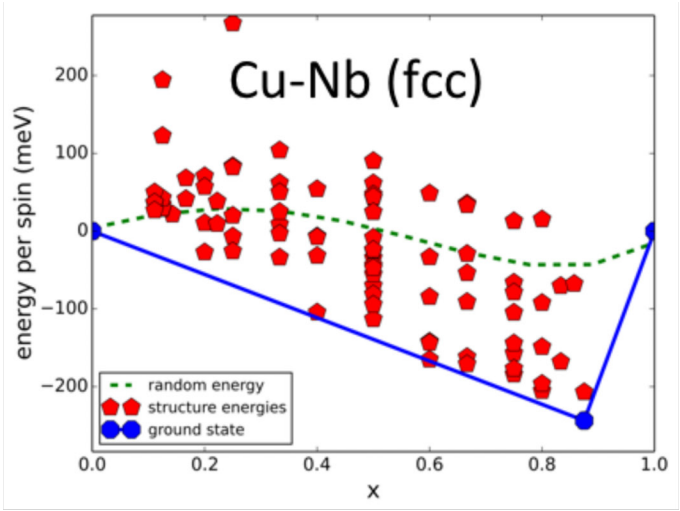

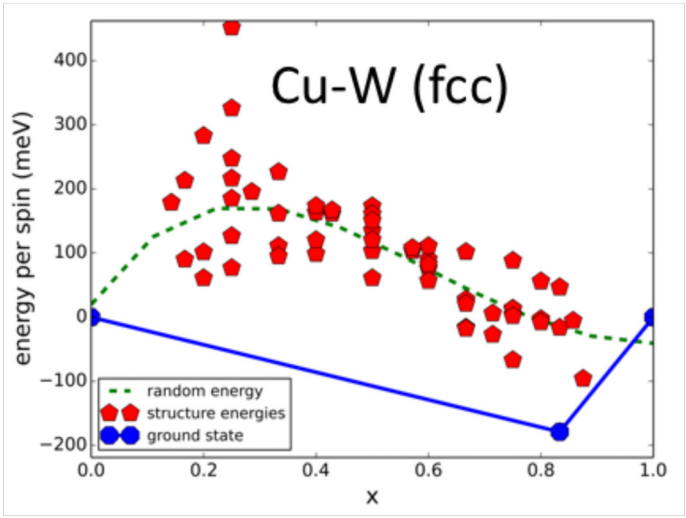

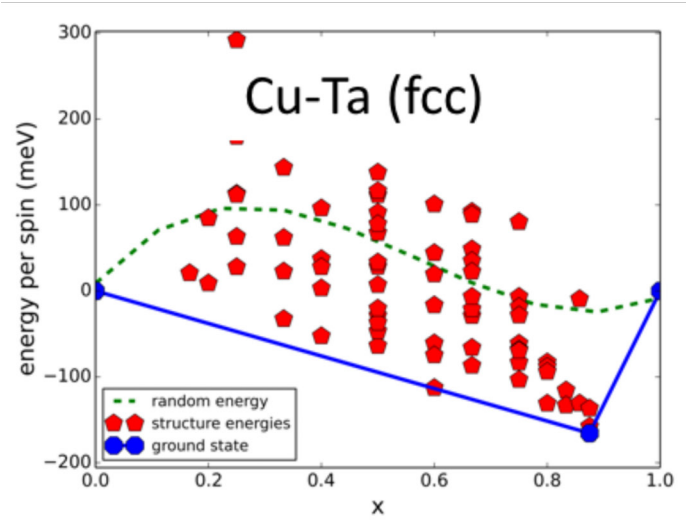

Figure 4.8: Ground state in the FCC Cu-X (X=Nb, Ta, W) systems as determined from Cluster Expansion (CE)-based search of the FCC configuration space in which the energetics were obtained from DFT-based calculations. x = Mole Fraction Mo. From Ref. [19].

out. Interestingly, these results are somewhat corroborated by recent investigations in the CuV multi-layered system [31]. In this system, Guo and coworkers investigated the evolution of growth stresses and interfacial structure in CuV multi-layered thin films and found that when the individual layers had thicknesses less than 0.5 nm considerable intermixing was present [14]. In their films, due to the considerably higher stiffness of V relative to Cu the BCC Cu state was stabilized. The explanation for the observed intermixing in the CuV case was ascribed to a surface exchange mechanism that resulted from the system attempting to minimize the interfacial energy between individual Cu and V layers. These results, however, suggest that an intrinsic thermodynamic tendency towards mixing may be prevalent in these systems.

For completeness, and to gain a better sense of the significance of the results presented above, we proceeded to calculate the ground state for the CuNi FCC system, as shown in Fig. 4.9, using the same CE- based framework as before.

In this case, it is shown that the system exhibits a small degree of immiscibility (of less than 2.5 kJ/mol-atom) although there are a large number of configurations lying on the CuNi ground state. CuNi form a prototypical isomorphous phase diagram at finite temperatures but the fact that it exhibits some tendency towards phase separation is a consequence of the Third Law as at low temperatures, when entropic contributions are vanishingly small, systems either order or phase separate.

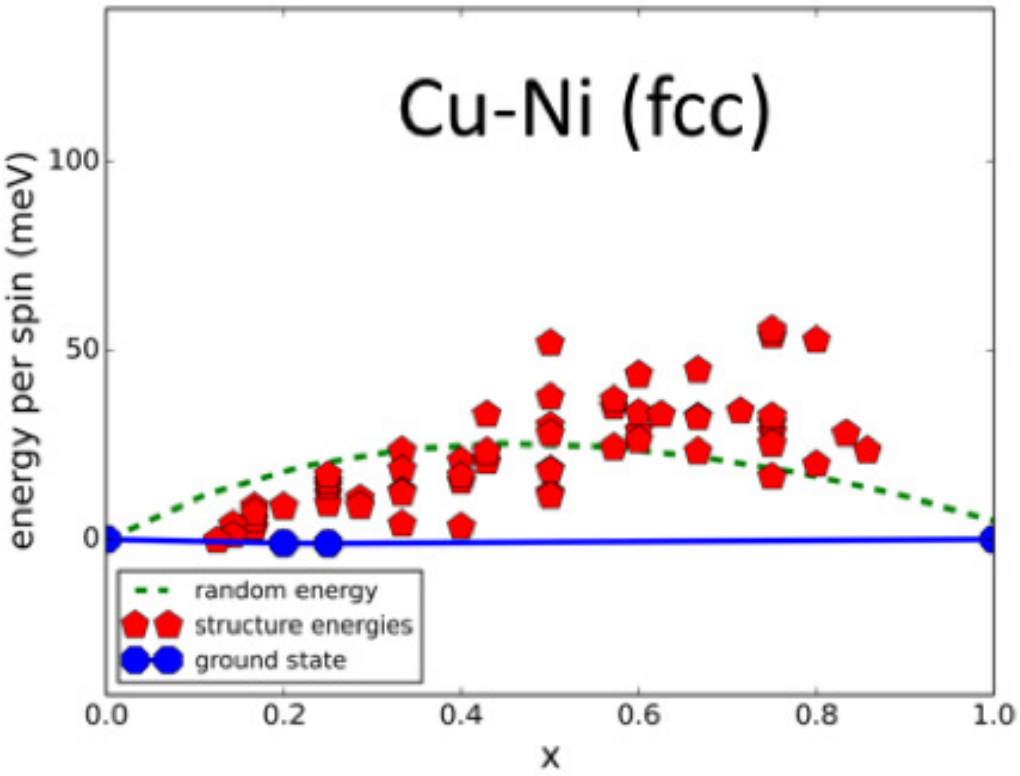

Figure 4.9: Ground state in the FCC Cu-Ni system. As determined from Cluster Expansion (CE)-based search of the FCC configuration space in which the energetics were obtained from DFT-based calculations. x = Mole Fraction Ni. The legend is defined in the text. From Ref. [19].

4.4 Hierarchical Morphologies: Comparison with Theory

We have demonstrated that nominally immiscible CuMo mixtures are able to self-organize into surprisingly rich, hierarchical structures. Our DFT calculations show that there are thermodynamic factors favoring such self-organization. However, understanding why these structures only form within a specific window of deposition rates and temperatures calls for an analysis of the kinetics of their formation. Phase separation during thin film growth has been shown to occur only on the exposed free surface because the interdiffusion rates, temperatures, and deposition times are too small to allow for significant diffusion in the bulk in many systems, including AlGe and CuMo [7, 11]. This situation has been named the "frozen bulk approximation by Adams *et. al.* [9]. In it, the morphology of the film below the surface is a record of the history of the surface composition profile in systems that phase separate during deposition. This means that depth into the film is equivalent to time [9]. Since thin film organization is strictly confined to the growing surface, any net vacancy flux required by Darkens analysis may be accommodated by changes in surface topography [32]. This is consistent with our observation of mounds that developed on the surfaces of the hierarchical structures as shown in Fig. 4.10.

Previously, the frozen bulk approximately has only been used to analyze homogeneously distributed concentration modulations with a single bilayer wavelength. To adapt this assumption to the morphology observed in our work, we combine it with a modified Volmer-Weber growth mechanism that results in large Cu domains

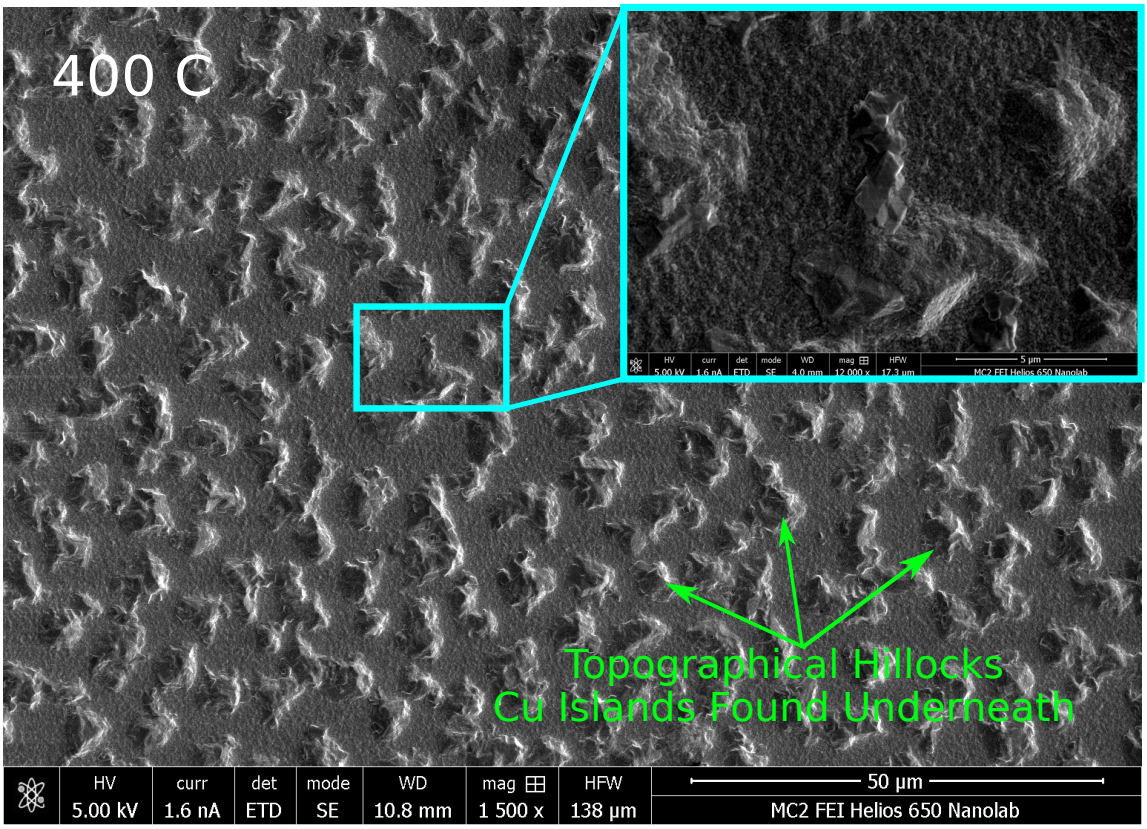

Figure 4.10: Secondary electron scanning microscopy image of the surface of the sample deposited at 400°C as shown in Fig. 4.1. Periodic hillocks or mounds were formed on the surface as a result of net vacancy flux required by Darken's analysis that were accommodated by these changes in surface topography. The large Cu islands were observed directly under these hillocks. From Ref. [19]

.

distributed throughout the film [18]. The inhomogeneity in crystal structure, chemical composition, and morphology in the CuMo hierarchical films studied here is a result of large differences in surface diffusion rates of the constituents combined with a low deposition rate. The sluggish diffusion of Mo atoms or clusters moving on the surface of the film is an order of magnitude smaller than the measured surface mobility of Cu [15, 16]. The frozen bulk approximation restricts atoms to only diffusing on the growing surface and the dissimilarity in surface diffusion rates leads to the Cu-rich and Mo-rich domains found on multiple length scales that were observed in this structure. A cartoon schematic in Fig. 4.11 shows the growth progression.

In Fig. 4.11, the first layer to arrive on the surface of the substrate is composed of an approximately equal phase fraction of Cu and Mo constituents. Phase decomposition begins as atoms whet the surface and like-atoms attempt to aggregate in like-domains as described by Lu and colleagues [5]. Before the next layer of material arrives on the surface, the faster Cu species diffuse on the surface and agglomerate much more readily than Mo and form Cu-rich domains.

At the next time step in Fig. 4.11, the subsequent few layers of material have arrived to form a complete mono- layer of material. The Cu domains have enlarged while the Mo-rich domains have also grown in size but at a slower rate and are left in-between the Cu domains. Cu atoms that have not yet reached the large Cu-domains are buried in between the Mo domains beginning the template for the lateral concentration modulated matrix. This first complete layer of material forms a

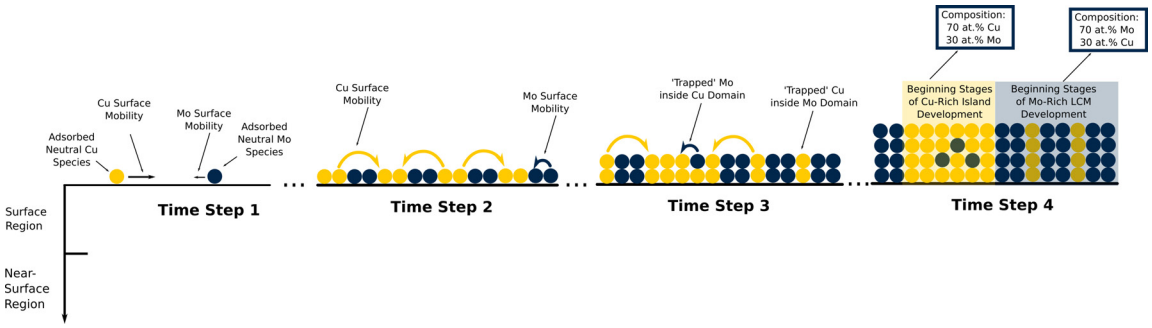

Figure 4.11: Schematic of the proposed modified Volmer-Weber growth mechanism. At each time step from left to right, the more mobile Cu atoms coalesce readily and form Cu "islands" at low deposition rates. The slower Mo species are left behind and instead form lateral concentration modulations with trapped Cu atoms. Cu atoms are represented as yellow and Mo atoms are blue.

template or seed for subsequent depositing atoms. During the rest of the deposition, the Cu and Mo atoms simply follow this template formed at the start of the films and develop a hierarchical structure.

A calculation of the surface diffusion length for Cu and Mo species is plotted in Fig. 4.12. We simply used the diffusion length equation,

$$d = \sqrt{Dt}, \tag{4.1}$$

here D is the surface diffusivity of Cu, t is the average time to deposit a monolayer, and d is the approximate spacing between the large Cu islands, to compute the surface diffusion length and compare this to the approximate spacing of the Cu islands. In the associated plot, at each of the deposition temperatures exposed to the constituents during sputtering 473, 673, and 873 K the Cu atoms are allowed to diffuse to greater distances than the average spacing between large Cu domains. This is unlike Mo, where at each of the deposition temperatures, the Mo species cannot diffuse long enough to agglomerate as the Cu atoms do.

Previous work on the CuMo system done at much higher deposition rates (0.7 nm/s) for each constituent does not exhibit hierarchical morphologies containing large Cu domains [11]. In this case, the higher deposition rates means that the growing surface is buried and frozen in place much faster. As such, there is not enough time for Cu atoms to agglomerate before being buried by the subsequent layer and the difference in mobility between the constituents is negligible, forming

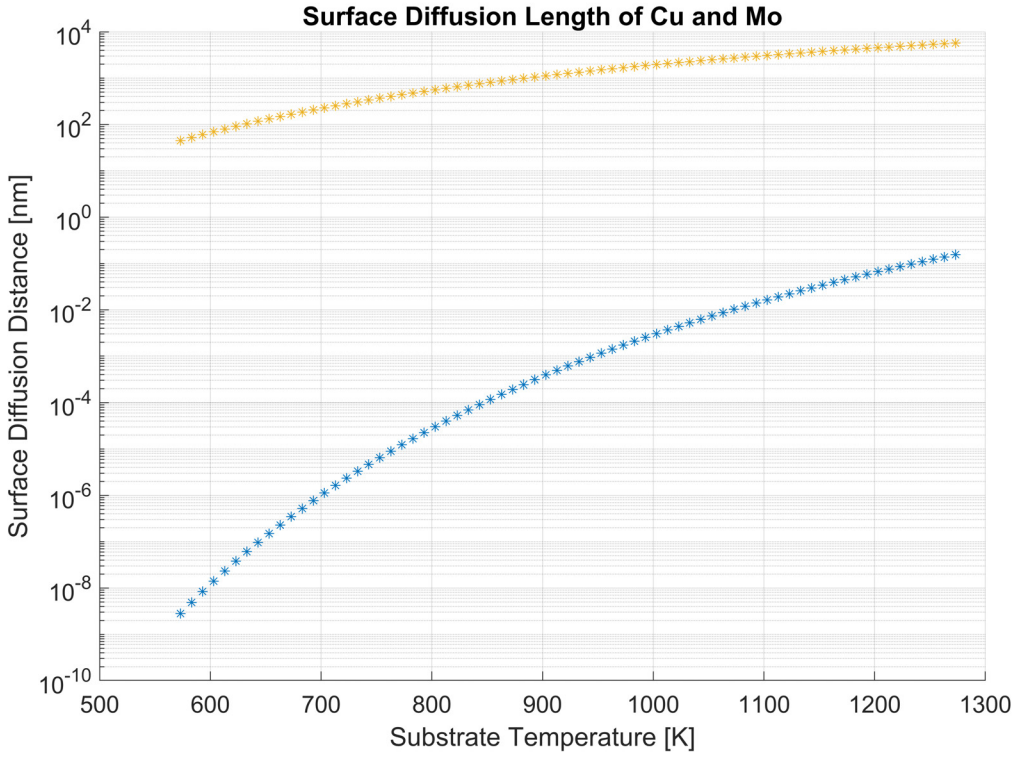

Figure 4.12: The yellow and blue curves are plots of surface diffusion lengths as a function of deposition temperature for Cu and Mo, respectively. The average time to deposit a monolayer of material (Cu and Mo) was used as the time parameter in the diffusion length equation. Comparing these diffusion lengths to the average spacing between large Cu domains as shown in Fig. 4.1, we observed that at low deposition rates, Cu atoms have enough time to diffuse to these large domains where Mo atoms do not. This is the case for all of the temperatures used in this study. From Ref. [19].

homogeneously distributed Cu/Mo concentration modulations.

4.5 Hierarchical Cu-Mo Thin Film: High Strength Material Without Shear Banding After Compression

The mechanical properties of this hierarchical structure are of particular interest to us because they provide a platform to study heterogeneous materials which have domains that are expected to be softer (the Cu-rich islands) and matrices that are expected to be exceptionally strong (Cu/Mo nanocomposite).

The structure studied here is comprised of Cu and Mo at two length scales: an interpenetrating 5 nm BCC Cu and 5 nm BCC Mo matrix; and 200 nm FCC Cu- rich domains containing FCC Mo nanoparticles that are approximately 1 nm in size. The stressstrain response of the hierarchical structure was investigated using nanopillar compression tests. Figure 4.13(a) shows a true stressstrain curve obtained by this technique.

Appreciable strain hardening can be observed until a maximum stress of 2.3 GPa was obtained at 12% plastic strain. Directly under the indent it was observed that the thickness of both Cu and Mo LCM domains increased to 7 nm. Further away from the indent tip, the LCM domains were reduced to 1.5 nm in length. The shape of the laminates was also altered to conform to the shape of the indent tip. The enhanced plastic deformation of this structure without shear banding is accounted for by the large Cu domains. The plasticity begins in the lower strength Cu domains, but the distributed Mo particles in these Cu grains increase the strength of the composite as a

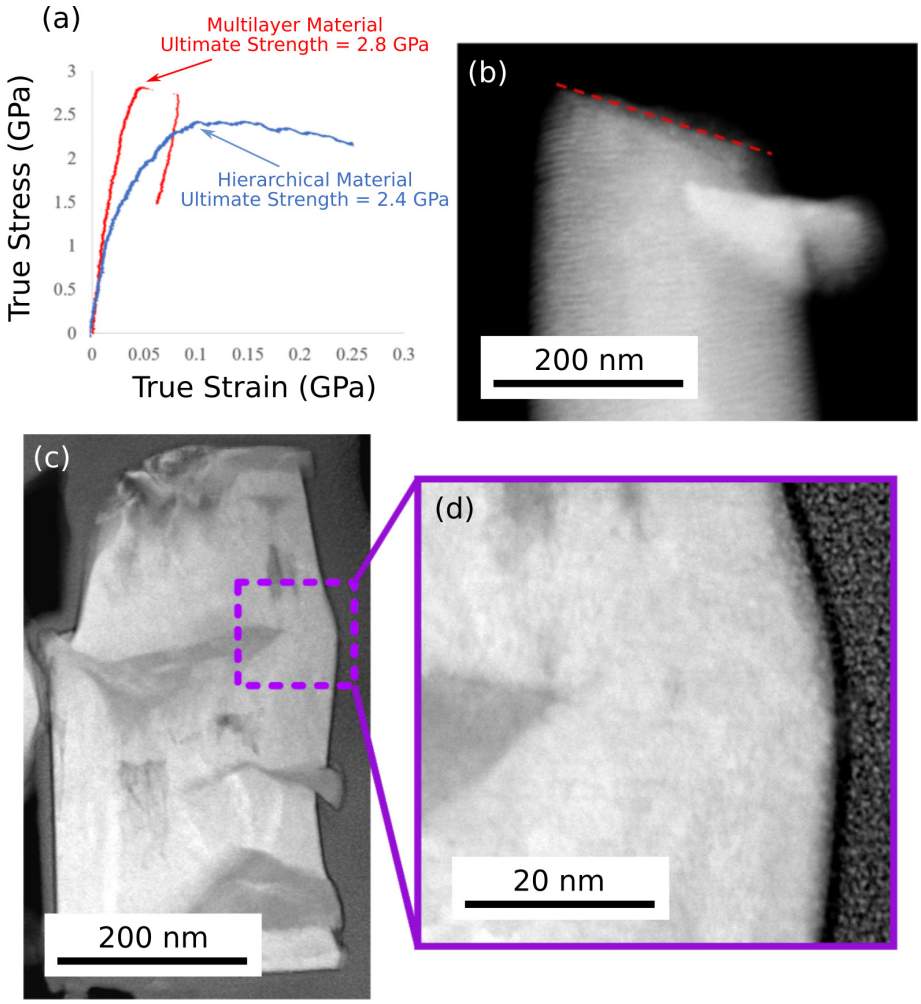

Figure 4.13: (a) True stress - true strain curves measured from nanopillar compression tests of the hierarchical structure (blue line and image (c)) and a 3 nm Cu/Mo multilayer (red line and image (b)). (b) STEM image of a 3 nm Cu / 3 nm Mo multilayer nanopillar after the com- pression test. (c) STEM image of a nanopillar made from the Cu/Mo hierarchical structure deposited at 400 °C after a compression test. (d) Magnified image of sample shown in (c) showing no plastic flow localization in the Cu/Mo LCM matrix. From Ref. [19].

result of precipitate hardening. As can be seen in the in-situ TEM compression tests presented in Figure 4.13, while the Cu domains are strain hardening, the bicontinuous Cu/Mo region begins to plastically deform. As elucidated in [33], the absence of shear banding is a result of the Cu grains diverting once a shear band encounters the Cu domains. In the bicontinuous region, the tortuousness of the interfaces make the glide of a dislocation difficult and thus limiting flow localization. Further high resolution in-situ TEM testing is required to confirm what happens to the Mo particles during deformation.

In contrast, the red curve in Fig. 4.13a shows data measured from a Cu/Mo multilayer with an individual layer thickness of 3 nm. A strain burst and stress drop were observed immediately after yielding. The lack of plasticity in the multilayer can be ascribed to localized shearing. A STEM image of the multilayered pillar after compression can be found in Fig. 4.13(b), where the top corner of the pillar completely sheared along the dotted line. Fig. 4.13(c) shows the nanopillar of the hierarchical structure after compression. The pillar remained intact with the deformation distributed throughout the thickness of the whole sample. A significant amount of strain came from the deformation of Cu rich islands, which is evidenced by the extrusions shown in Fig. 4.13(c). Because of the Cu island has access to the free surface of the nanopillar, the 2.3 GPa stress is an underestimate of the strength of the bulk material. With Cu rich islands fully constrained by the fine scale matrix, the stress level that can be sustained is expected to be higher. However 2.3 GPa

is already comparatively high, close to the 2.8 GPa maximum flow stress measured in the 3 nm multilayer, which is the highest stress value reported from a Cu/Mo based metallic material [33]. Gradual strain softening was observed in the hierarchical nanopillar after the peak stress. The stress remained above 2 GPa up to 20% plastic strain and no catastrophic failure was observed when the test stopped at 22% plastic strain. Figure 4.13(d) shows a magnified image of the region in the rectangle in Figure 4.13(c), where the matrix underwent highest amount of deformation. Shear band like those observed in Cu-refractory metal multilayers were not evident in the region [33–35]. Our hierarchical Cu/Mo structures thus provides high strength and sustainable plasticity with suppressed shear band formation.

It has been reported in previous works [20] that shear deformation will cause a structural transformation in BCC Mo. Mo will transform into FCC under significant pressure ($\approx$ 8 GPa) even at room temperature. In this work, structural transformations from BCC Mo to FCC Mo as a result of our nanopillar compression tests were not observed post-mortem. While further study is needed to confirm this by completing in-situ compression tests, the required shear stress was not applied during the nanomechanical testing in this work. Further experimentation will be conducted to confirm any potential phase transformations in FCC Mo particles.

Local stresses and strains where the localized deformation was observed were not determined in this work. This will need to be studied using crystal elastic-plastic and FEM models in future work. Additionally, micropillar compression tests on larger

samples (not just *in situ* TEM) as well as tensile and bend tests will be reported in future reports.

4.6 Conclusions

In summary, we have synthesized a novel, pseudomorphic CuMo hierarchical thin film with differing structure on multiple length scales. Cu and Mo constituents are chemically separated in the structure, but exist in metastable crystal structures at different locations within the film. These metastable states were rationalized via DFT calculations. At low temperatures, the matrix is comprised of coherent BCC CuMo lateral concentration modulations and large Cu-rich domains with ordered FCC Mo particles are scattered throughout the film. At higher temperatures, the structure on all length scales coarsens and the metastable Cu and Mo domains relax towards their bulk crystal structures.

Our results also show that a nanocomposite composed of large Cu islands and bicontinuous zones with a few nm length scale possesses very high strength as well as good deformability [33]. After large deformation, shear band formation was not observed in the nanocomposite, as opposed to in the multilayers [33]. The hierarchical structure is proposed to encourage the suppression of shear banding [33].

References

[1] R. Alert, P. Tierno, and J. Casademunt. Formation of metastable phases by spinodal decomposition. *Nature Communications*, 7(1):1–7, 2016.

[2] C.V. Thompson. Structure evolution during processing of polycrystalline films. *Annual Review of Materials Science*, 30(1):159–190, 2000.

[3] C. Nan and Q. Jia. Obtaining ultimate functionalities in nanocomposites: Design, control, and fabrication. *MRS Bulletin*, 40(9):719–724, 2015.

[4] W.D. Nix. Metallic thin films: stresses and mechanical properties. In *Metallic Films for Electronic, Optical and Magnetic Applications*, pages 353–421. Elsevier, 2014.

[5] C. Lu, Y.and Wang, Y. Gao, R. Shi, X. Liu, and Y. Wang. Microstructure map for self-organized phase separation during film deposition. *Physical Review Letters*, 109(8):086101, 2012.

[6] C.M. Müller, A.S. Sologubenko, S.S.A. Gerstl, and R. Spolenak. On spinodal decomposition in cu–34 at.% ta thin films–an atom probe tomography and transmission electron microscopy study. *Acta Materialia*, 89:181–192, 2015.

[7] C.D. Adams, M. Atzmon, Y.T. Cheng, and D.J. Srolovitz. Phase separation during co-deposition of al–ge thin films. *Journal of Materials Research*, 7(3):653–666, 1992.

[8] K. Fukutani, K. Tanji, T. Saito, and T. Den. Phase-separated al–si thin films. *Journal of Applied Physics*, 98(3):033507, 2005.

[9] C.D. Adams, D.J. Srolovitz, and M. Atzmon. Monte carlo simulation of phase separation during thin-film codeposition. *Journal of Applied Physics*, 74(3):1707–1715, 1993.

[10] C.M. Müller and R. Spolenak. An in situ x-ray diffraction study of phase separation in cu–ta alloy thin films. *Thin Solid Films*, 598:276–288, 2016.

[11] B. Derby, Y. Cui, J.K. Baldwin, and A. Misra. Effects of substrate temperature and deposition rate on the phase separated morphology of co-sputtered, cu-mo thin films. *Thin Solid Films*, 647:50–56, 2018.

[12] B. Gržeta, N. Radić, D. Gracin, T. Došlić, and T. Car. Crystallization of cu50w50 and cu66w34 amorphous alloys. *Journal of Non-crystalline Solids*, 170(1):101–104, 1994.

[13] A. Puthucode, M.J. Kaufman, and R. Banerjee. Early stages of crystallization in phase-separated amorphous copper-niobium alloy thin films. *Metallurgical and Materials Transactions A*, 39(7):1578–1584, 2008.

[14] Z. Zhang, J. Guo, G. Dehm, and R. Pippan. In-situ tracking the structural and chemical evolution of nanostructured cucr alloys. *Acta Materialia*, 138:42–51, 2017.

[15] J. Steigman, W. Shockley, and F.C. Nix. The self-diffusion of copper. *Physical Review*, 56(1):13, 1939.

[16] J.l Askill and D.H. Tomlin. Self-diffusion in molybdenum. *Philosophical Magazine*, 8(90):997–1001, 1963.

[17] K. Oura, V.G. Lifshits, A.A. Saranin, A.V. Zotov, and M. Katayama. *Surface science: an introduction*. Springer Science & Business Media, 2013.

[18] E. Bauer. Phänomenologische theorie der kristallabscheidung an oberflächen. i. *Zeitschrift für Kristallographie-Crystalline Materials*, 110(1-6):372–394, 1958.

[19] B. Derby, Y. Cui, J.K. Baldwin, R. Arróyave, M.J. Demkowicz, and A.l Misra. Processing of novel pseudomorphic cu–mo hierarchies in thin films. *Materials Research Letters*, 7(1):1–11, 2019.

[20] S.J. Wang, H. Wang, K. Du, W. Zhang, M.L. Sui, and S.X. Mao. Deformation-induced structural transition in body-centred cubic molybdenum. *Nature Communications*, 5(1):1–9, 2014.

[21] S.S.P Parkin, N. More, and K.P. Roche. Oscillations in exchange coupling and magnetoresistance in metallic superlattice structures: Co/ru, co/cr, and fe/cr. *Physical Review Letters*, 64(19):2304, 1990.

[22] F.X. Redl, K-S Cho, C.B. Murray, and S. O'Brien. Three-dimensional binary superlattices of magnetic nanocrystals and semiconductor quantum dots. *Nature*, 423(6943):968–971, 2003.

[23] D. Shechtman, D. Van Heerden, and D. Josell. Fcc titanium in ti-al multilayers. *Materials Letters*, 20(5-6):329–334, 1994.

[24] P.M. Anderson, J.F. Bingert, A. Misra, and J.P. Hirth. Rolling textures in nanoscale cu/nb multilayers. *Acta Materialia*, 51(20):6059–6075, 2003.

[25] B. Ham and X. Zhang. High strength mg/nb nanolayer composites. *Materials Science and Engineering: A*, 528(4-5):2028–2033, 2011.

[26] A. Van De Walle, M. Asta, and G. Ceder. The alloy theoretic automated toolkit: A user guide. *arXiv preprint cond-mat/0212159*, 2002.

[27] G. Kresse and J. Furthmüller. Efficient iterative schemes for ab initio total-energy calculations using a plane-wave basis set. *Physical Review B*, 54(16):11169, 1996.

[28] G. Kresse and J. Furthmüller. Efficiency of ab-initio total energy calculations for metals and semiconductors using a plane-wave basis set. *Computational Materials Science*, 6(1):15–50, 1996.

[29] J.Z Liu and A. Zunger. Thermodynamic states and phase diagrams for bulk-incoherent, bulk-coherent, and epitaxially-coherent semiconductor alloys: Application to cubic (ga, in) n. *Physical Review B*, 77(20):205201, 2008.

[30] J.Z. Liu and A. Zunger. Thermodynamic theory of epitaxial alloys: first-principles mixed-basis cluster expansion of (in, ga) n alloy film. *Journal of Physics: Condensed Matter*, 21(29):295402, 2009.

[31] L.F. Zeng, R. Gao, Z.M. Xie, S. Miao, Q.F. Fang, X.P. Wang, T. Zhang, and C.S. Liu. Development of interface-dominant bulk cu/v nanolamellar composites by cross accumulative roll bonding. *Scientific Reports*, 7(1):1–9, 2017.

[32] R.W. Balluffi, S.M. Allen, and W.C. Carter. *Kinetics of Materials*. John Wiley & Sons, 2005.

[33] Y. Cui, B. Derby, N. Li, N.A. Mara, and A. Misra. Suppression of shear banding in high-strength cu/mo nanocomposites with hierarchical bicontinuous intertwined structures. *Materials Research Letters*, 6(3):184–190, 2018.

[34] N.A. Mara, D. Bhattacharyya, P. Dickerson, R.G. Hoagland, and A. Misra. Deformability of ultrahigh strength 5 nm cu/ nb nanolayered composites. *Applied Physics Letters*, 92(23):231901, 2008.

[35] A. Misra, H. Kung, D. Hammon, R.G. Hoagland, and M. Nastasi. Damage mechanisms in nanolayered metallic composites. *International Journal of Damage Mechanics*, 12(4):365–376, 2003.

CHAPTER V

Comparison of Cu-Mo System to Other Phase Separating, FCC/BCC Thin Film Combinations

5.1 Introduction

Phase separation in metallic thin films has been extensively studied in a number of immiscible, binary metal combinations [1–4]. Given adequate kinetic conditions, co-deposition of immiscible constituents will lead to phase separation during growth [5]. While the same physical mechanisms that lead to phase separation in bulk materials also occurs in thin films, the process is complicated by a two factors as outlined by Atzmon *et. al.*: (1) deposition is occurring at a fixed, externally imposed rate and (2) atomic transport occurs preferentially along the advancing surface [3]. As such, the reaction front between decomposing material and decomposed material can be externally controlled through the deposition conditions, namely the deposition rate and deposition temperature. This is unlike bulk material phase separation.

The seminal work describing the phase separation process in thin films was done by Atzmon *et. al.* using a Cahn-Hilliard framework [3]. It was assumed that at

typical deposition temperatures, bulk diffusion was limited and adatom motion on the growing film was the dominant diffusion mechanism [3]. Atzmon described the concentration variation as a function of time as,

$$\frac{\partial c}{\partial t} = D_s \nabla^2 c + \frac{\nu}{\delta}(c_0 - c), \tag{5.1}$$

where c is the concentration profile, ν is the deposition flux, D_s is the surface interdiffusivity of the two elements, and δ is the width of the surface layer (on the order of the interatomic spacing). Atzmon also described the surface interdiffusion length, ρ, as the defining parameter determining the phase separated domain size. It was written as,

$$\rho = \sqrt{\frac{D_s \delta}{\nu}}. \tag{5.2}$$

Atzmon's model for phase separation in thin films was later verified empirically when Al and Ge were co-evaporated onto a substrate at elevated temperature by Adams *et. al.* [6]. This work found agreement with Eq. 5.2: as temperature increased, the domain size of lateral concentration modulations increased. According to the Atzmon model, as deposition temperature increased, the interdiffusion length increased through an increase in the surface interdiffusivity coefficient [3].

In more recent work, several studies have shown that it is the interdiffusion length that also determines the final orientation of the phase separated domains, not simply the domain size [2, 4, 7]. Lu and coworkers recognized that the interdiffusion length

actually describes a competition between the rate of phase separation (through the interdiffusivity coefficient) and the deposition rate as shown in Eq. 5.2 [2]. Their 2D phase field model showed that when the phase separation rate was greater than the rate of material being added to the film, lateral concentration modulations of the constituent phases would exist. If, however, the deposition rate was higher than the rate of phase separation, the resultant film would exhibit vertical concentration modulations of the two phases.

Kumar *et. al.* extending this phase field model in three dimensions and furthered this research by showing that when bulk diffusion is activated at higher deposition temperature, interconnections of the phases leads to random concentration modulations [8].

Our previous work showed that by controlling the deposition conditions and in turn controlling the competition between the rate of phase separation and deposition rate, transition between three archetypal morphologies was achieved [4]. At low deposition rates, however, hierarchical phase separation was observed in a few studies [9]. In this work, we discovered a novel, pseudomorphic CuMo hierarchical thin film with differing structure on multiple length scales. Cu and Mo constituents were chemically separated in the structure, but exist in metastable crystal structures at different locations within the film. These metastable states were rationalized via DFT calculations. At low temperatures, the matrix was comprised of coherent BCC CuMo lateral concentration modulations and large Cu-rich domains with ordered

FCC Mo particles are scattered throughout the film. At higher temperatures, the structure on all length scales coarsens and the metastable Cu and Mo domains relax towards their bulk crystal structures.

While we found these structures through experiment, no model for phase separating thin films has been put forth to describe the physical mechanisms that lead to the development of hierarchical thin film morphologies with phase separation occurring on multiple length scales. In this Chapter, we present preliminary results comparing the Cu-Mo system with other immiscible FCC/BCC thin film combinations. We also introduce a novel, co-deposited, ternary Cu/Mo/Ag thin film that also exhibited a hierarchical morphology. We use these results to suggest a modification to the Atzmon surface interdiffusion model. There still requires much simulation work to verify the subsequent discussion in this Chapter.

In attempt to describe the hierarchical morphology development in phase separating thin films at certain deposition conditions, we hypothesized in our previous work, that the interdiffusion length model put forth by Atzmon *et. al.* needs to consider the difference in mobility between the constituent materials and not simply assume a one interdiffusion diffusivity [4, 9]. For example, at a deposition temperature of 600 °C, the surface diffusivity of molybdenum adatoms on a Cu surface is 3.9×10^{-5} m^2/s as compared to 5×10^{-2} m^2/s for copper adatoms on a molybdenum surface [10]. We decided to test this hypothesis in this Chapter by comparing the results of Cu-Mo system [4, 9] to other immiscible systems with different kinetic and thermodynamic

properties. As such, we conducted a series of co-depositions of comparable, immiscible, and multicomponent systems at elevated temperature outlined in Chapter 2. These systems include: Cu/Ag, AgMo, and Cu/Mo/Ag. Each system is a metallic combination with different thermodynamic (e.g. heat of mixing) and kinetic (e.g. diffusivity) parameters, but still mutually immiscible. A deposition temperature of 600°C and relatively high and low deposition rates were chosen so we could compare these different systems at the same deposition conditions.

The phase diagrams for each system, as shown in Fig. 5.1, illucidate that these three systems have very limited mutual solubility, and phase separation into domains with atomically sharp interfaces is energetically preferable [11]. These systems are good model systems as they each have different kinetic properties [10], which allows for the physical diffusion mechanisms describing their transition in morphology to be studied. No ternary phase diagram for the Cu/Mo/Ag system exists to date.

The Cu/Ag system and Ag/Mo and the Cu/Mo/Ag systems are described in turn.

5.2 Results

5.2.1 Equiaxed, Phase-Separated Grains in the Co-deposited Cu-Ag Sample

Fig. 5.2 shows a comparison between Cu-Ag and Cu-Mo phase separated thin films deposited at 600 °C and two different deposition rates. Phase separation was observed in both of these systems at the given substrate temperature and material flux. The atomic number contrast images in Fig. 5.2 show a different transition in morphology depending on the deposition rate for each material system.

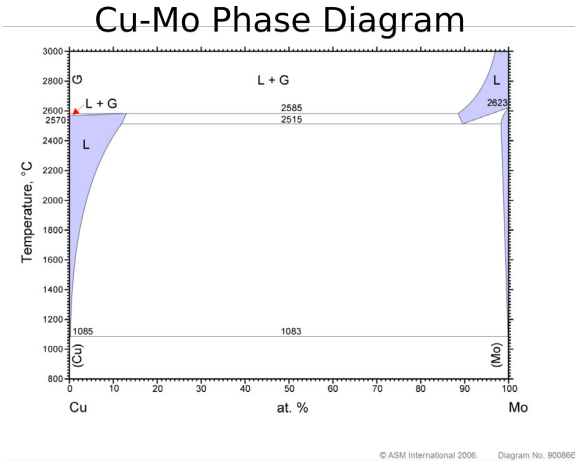

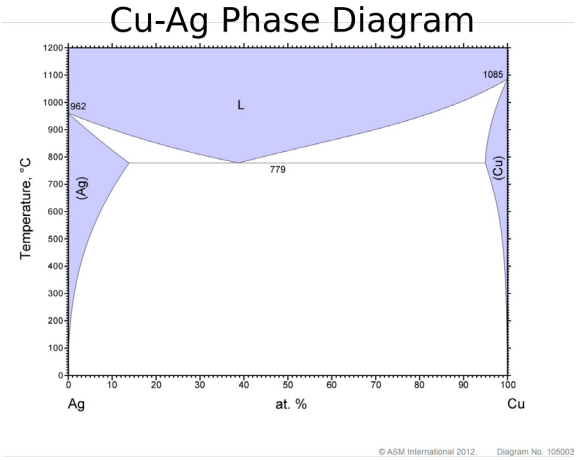

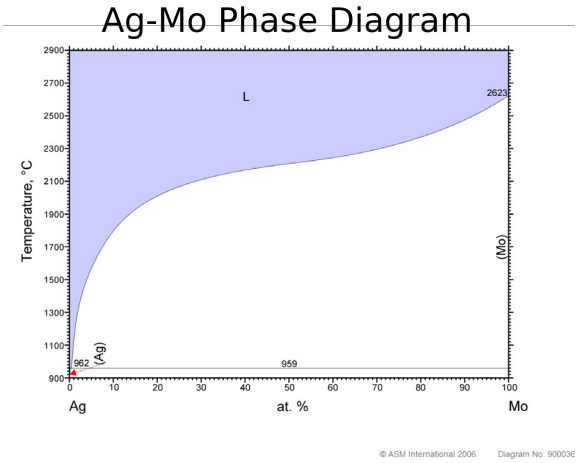

Figure 5.1: Phase diagrams showing very limited solubility for (a) Cu/Mo, (b) Cu/Ag, and (c) Ag/Mo [11].

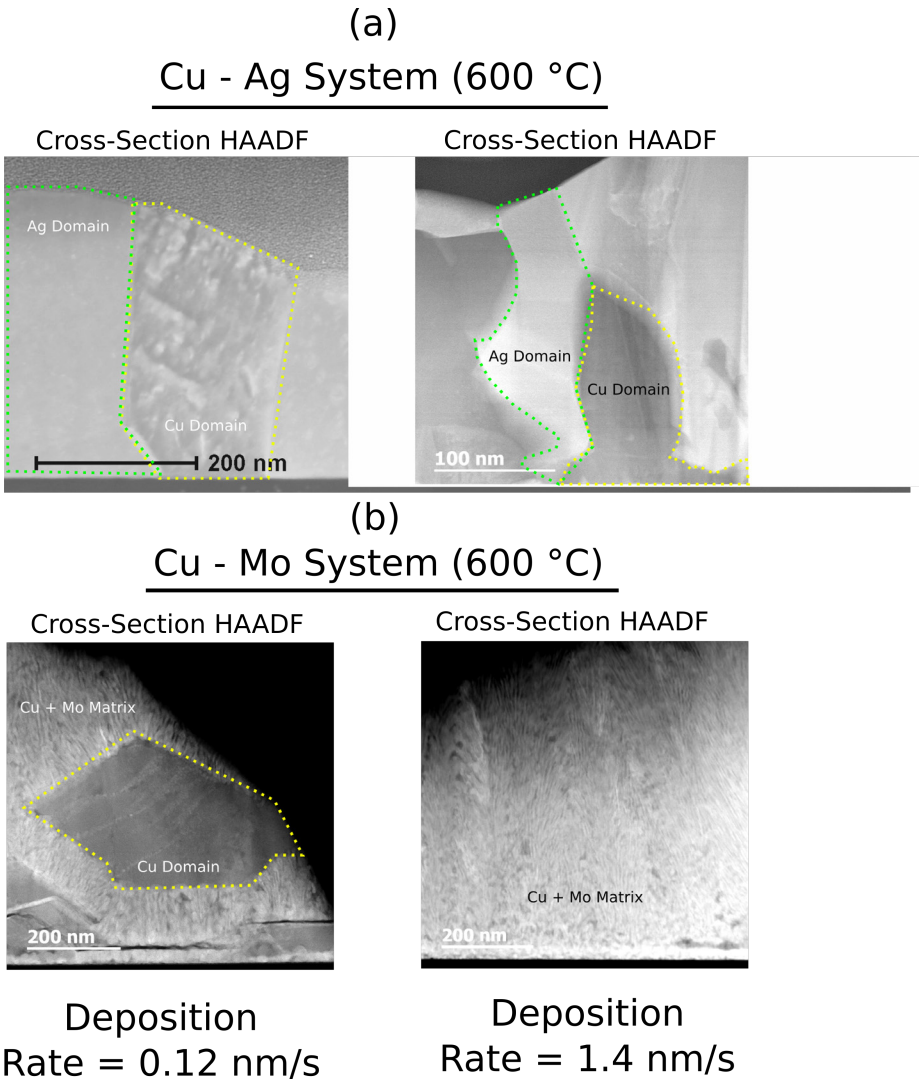

Figure 5.2: High Angle Annular Dark Field (HAADF) images of a DCMS, co-deposited Cu-Ag and Cu-Mo samples deposited at 600°C and equal phase fraction. In each image, the species (i.e. Cu, Mo, or Ag) with higher atomic number, appears bright as compared to the other constituent. In (a), we can see equiaxed grains of Cu and Ag formed during co-sputtering at 600°C at both deposition rates. In (b), however, the film exhibited a hierarchical structure when the deposition rate was decreased to 0.12 nm/s.

Equiaxed, Cu- and Ag- rich grains of approximately 75 nm grain size were present at the highest deposition rate for Cu and Ag, 1.2 nm/s. Cu grains appear darker relative to the higher atomic number Ag grains. Both of the Cu- and Ag- rich grains exhibited a relatively high aspect ratio with the grain's major axis pointed towards the film surface. Depositing the same amount of material at a lower deposition rate of 0.12 nm/s, a similar nanostructure was observed. Equiaxed grains of Cu and Ag were present throughout the film at an approximate grain size of 175 nm. The grains exhibited a smaller aspect ratio as compared to the sample deposited at a higher deposition rate, but were noticeably larger in size. Other than a change in grain size, the Cu/Ag phase separated morphology remained unaltered when the deposition rate was lowered.

A significant transition did occur in the Cu-Mo system, however, when the deposition rate was lowered. In Fig. 5.2(b), at the high deposition rate of 1.2 nm/s, Cu and Mo phases were distributed in lateral concentration modulations (LCM) at a modulation wavelength of approximately 7 nm. This morphology was homogeneously distributed across the entirety of the film. At low deposition rate, though, phase separation was no longer homogeneous but instead exhibited a hierarchical distribution of Cu- and Mo- rich phase separated domains. Large Cu-rich domains were observed to be contained within a laterally phase separated Cu-Mo matrix. High resolution images contained in our previous work [9] of the Cu domain showed that pseudomorphic, FCC Mo precipitates existed inside the FCC Cu domains. This

hierarchical morphology was observed across the sample. Raising the temperature of the sample during deposition did not relinquish this hierarchical morphology [9].

In summary, Fig. 5.2 shows that at the same deposition conditions, depositing two different systems results in a change in morphology evolution at changing deposition rate.

5.2.2 Hierarchical Morphology in the Co-deposited Ag-Mo Sample at Low Deposition Rate

Fig. 5.3 shows the evolution of the Mo-Ag system as a function of deposition rate. Heterogeneous phase separation of Ag and Mo led to the development of a hierarchical structure at both deposition rates studied here. Similar to the familiar Ag agglomeration observed in many single-phase films [12], relatively large Ag domains were observed to be surrounded by a Ag- and Mo- rich LCM matrix. These density of these larger domains was significantly less at the lower deposition rate, even though the phase fraction of Ag and Mo are equal in both samples. The deposition rate did not change the phase separated domain distribution, only the domain size. At the lower deposition rate of 0.12 nm/s, the Ag agglomerates were approximately 50 nm in diameter, while at 1.4 nm/s the domains were approximately 20 nm in diameter.

As shown in the FFT inset in Fig. 5.3, the Ag and Mo phase were observed to exist in their equilibrium FCC and BCC crystal phases, respectively. No evidence of nano-precipitates of Mo was present in the Ag agglomerates at either deposition rate, but more detailed high resolution TEM is required to confirm this observation. EDXS measurements show a higher concentration of Ag in the agglomerates as compared

to the matrix as shown in the EDXS map insetted in Fig. 5.3.

In summary, Fig. 5.3 shows that at both deposition rate conditions, a hierarchical morphology was observed. Higher temperature experiments have yet to be completed.

5.2.3 Deposition of Ternary System With Mutual Immiscibility

Previous studies into phase separating thin films have focused on binary, immiscible systems. In this section we introduce priliminary results on a system that has not yet been studied in the literature: Cu-Mo-Ag. Interestingly, each pair of metals in this combination is highly insoluble. Fig. 5.4 shows this co-deposited ternary system comprised of Cu-Mo-Ag at three different substrate temperatures.

This figure is notable for a few reasons. Phase distribution, as determined by atomic number contrast imaging, varied as a function of temperature. At 400 °C, Fig. 5.4(a) shows that a homogeneous morphology of lateral concentration modulations of Cu- and Mo- and Ag- rich domains. A hierarchical distribution of phase was observed when the film was deposited at 600°C. A large Cu domain approximately 500 nm was observed in the structure. The higher magnification inset image of the Cu domain showed the existence of precipitates of approximately 5 nm in diameter. The matrix, however, was characterized by 5 nm lateral domains of Mo- and Ag- rich domains as shown by the opposing inset image. At 800°C as shown in Fig. 5.4(c), a similar morphology was present with all length scales coarsened as compared to the sample deposited at 600°C. A notable difference at 800°C, though, is the presence

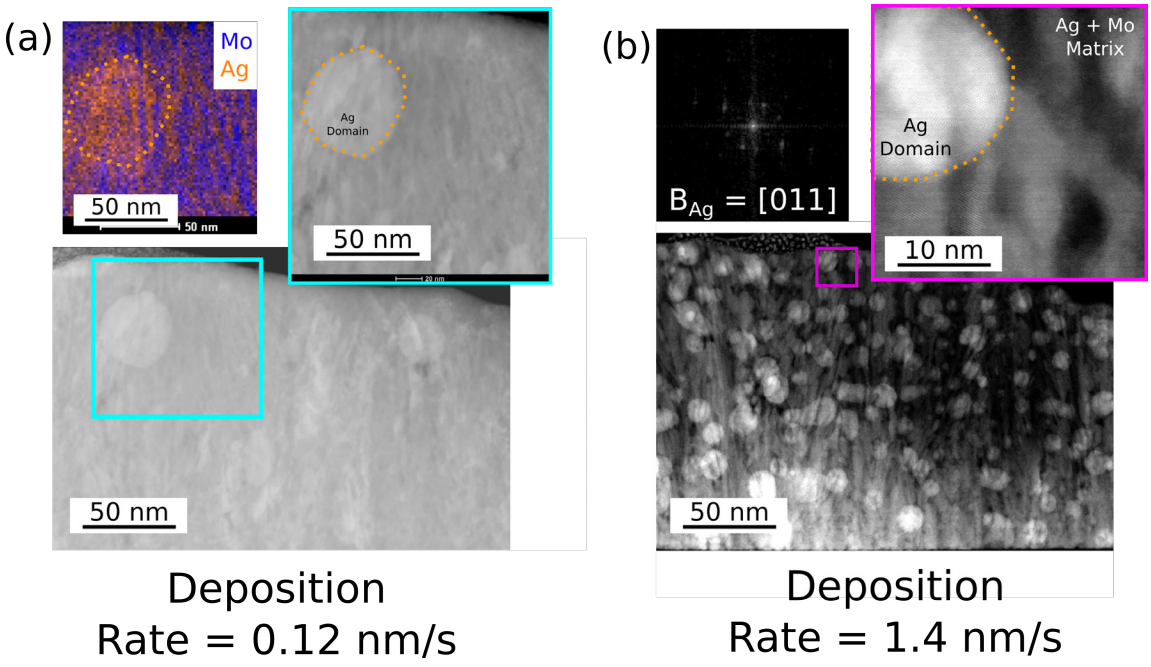

Figure 5.3: High Angle Annular Dark Field (HAADF) images of a DCMS, co-deposited Ag-Mo deposited at 600°C and equal phase fraction. At each deposition rate, a hierarchical phase separated structure was observed where an LCM matrix of Ag- and Mo-rich domains surrounded large Ag domains outlined in orange. At the lower deposition rate presented in (a) we see relatively coarse Ag domains scattered throughout the Ag-Mo matrix. The inset composition map shows the Ag-rich domain in the structure where Ag is highlighted in orange and Mo in blue. The composition map suggests a higher concentration of Ag in the agglomerate than the Ag-rich domains in the matrix. Each Ag agglomerate is approximately 50 nm in size. In (b), however, the higher deposition rate led to a decrease in the size of the Ag domains. The highly magnified HAADF image shows atomic resolution in the Ag agglomerate and suggests that there may be "trapped" Mo particles inside the domain. The FFT pattern taken from the magnified Ag domain shows the [011] FCC crystal structure of the Ag.

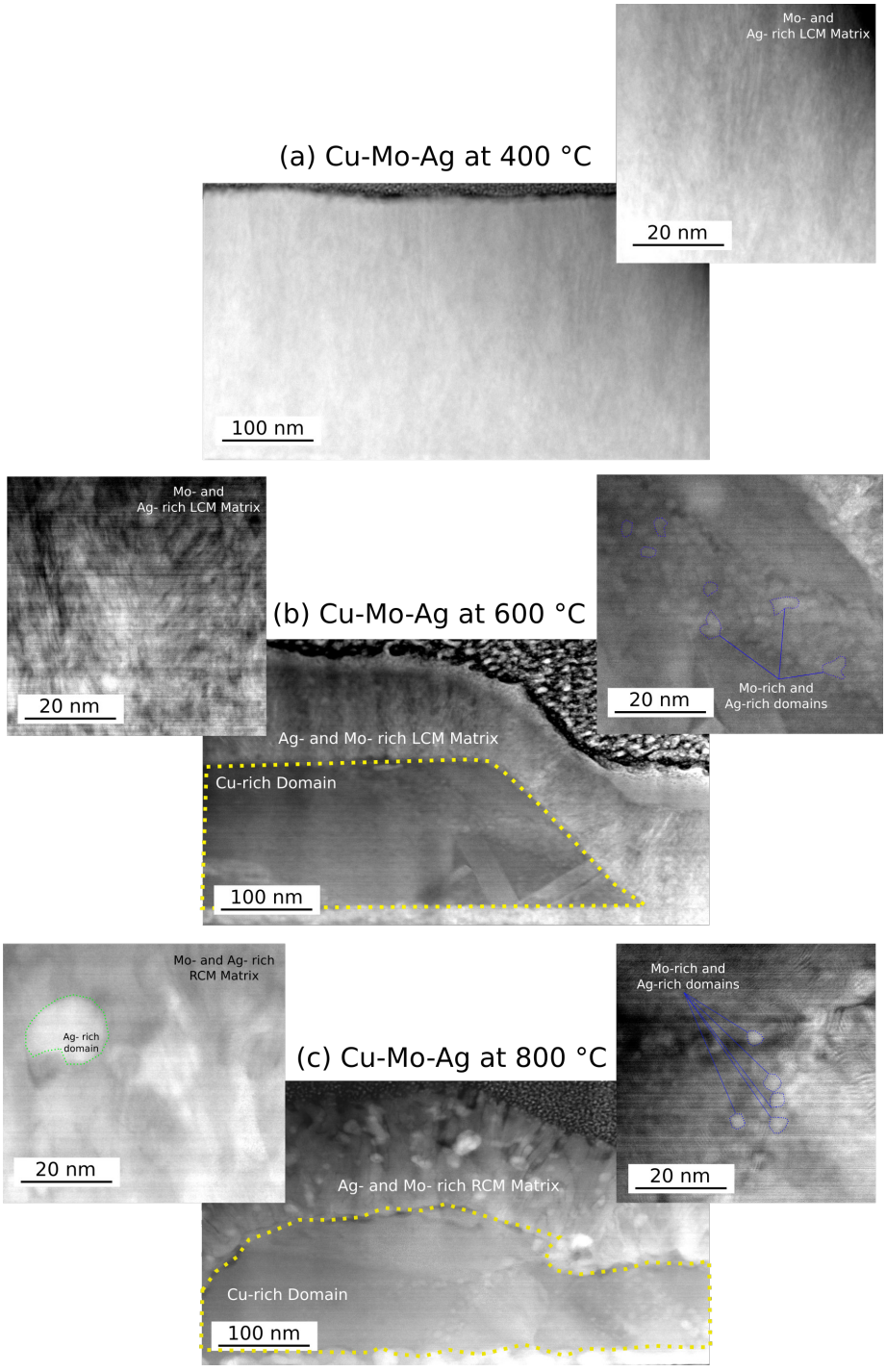

Figure 5.4: High Angle Annular Dark Field (HAADF) images of a DCMS, co-deposited Cu-Mo-Ag deposited at (a) 400°C, (b) 600°C, and (c) 800°C and equal phase fraction. The distribution of phases was altered as a function of substrate temperature. At 400 °C, a homogeneous LCM matrix of Cu- and Mo- and Ag- rich domains. A hierarchical structure was observed starting at 600°C with large Cu domains surrounded by an LCM matrix of Ag and Mo. The structure coarsened at 800°C, and silver agglomerates began to appear.

of Ag-rich agglomerates contained within the matrix. The matrix also seemed to exhibit a more randomized distribution of the Mo- and Ag- rich domains.

Detailed investigation into the structure of the precipitates inside the Cu domain will be completed in later work.

5.3 Discussion

5.3.1 Morphology Dependent Relative Surface Diffusion Lengths

Thermodynamics favored phase separation for all of the binary and ternary co-deposited samples introduced in this chapter. Mutual solid solubilities were extremely limited for each pair of constituents. And the kinetics established during deposition resulted in phase separated morphologies in each film.

Previous work into phase separated thin film morphologies have concluded that the controlling parameter for determining the final phase separated morphology is the surface diffusion length as written in Eq. 5.2 [3]. The domain size of phase separated thin film domains found by Adams *et. al.* is proportional to this value, which is dependent on the deposition rate and interdiffusion coefficient. The latter term is substrate temperature dependent. Additionally, 5.2 describes a competition between the rate of phase separation and the deposition rate. The competition between these two rates has been shown to determine the directionality of phase separated domains [2].

This surface diffusion model does not yet predict or adequately explain the physical growth mechanisms for the hierarchical structures described in this chapter or

in Chapter 4 [9]. Fig. 5.2 shows a dichotomy between two systems deposited at the same substrate temperature and deposition rates. The Cu-Mo system exhibited a hierarchical, phase-separated morphology at low deposition rate, but a homogeneous morphology at high deposition rate. This was not the case for the co-deposited Cu-Ag system at the two deposition rates. Equiaxed Cu- and Ag- rich grains with the same morphology were observed at both deposition rates. The domain size was, however, coarser at the low deposition rate for both systems. These data seem to suggest that the while the surface diffusion length during physical vapor deposition does control the domain size as originally predicted by Atzmon *et. al.*, it must be system-dependent. The Cu-Ag system did not exhibit the same hierarchical structure as did the Cu-Mo system.

This hypothesis was explored further by co-depositing Mo and Ag at elevated temperature. Fig. 5.3 shows that a hierarchical structure of Mo- and Ag- rich domains is present at both of the deposition rates tested and at the same substrate temperature. By lowering the deposition rate, the structure similarly coarsened to the aforementioned binary systems.

These observations empirically suggest that the surface diffusion length must be modified to include difference in diffusion coefficients for each of the constituents being deposited. Fig. 5.5 shows plots of the difference in surface diffusion length for each co-deposited pair studied in this work.

To determine this value, the difference in interdiffusion length between two con-

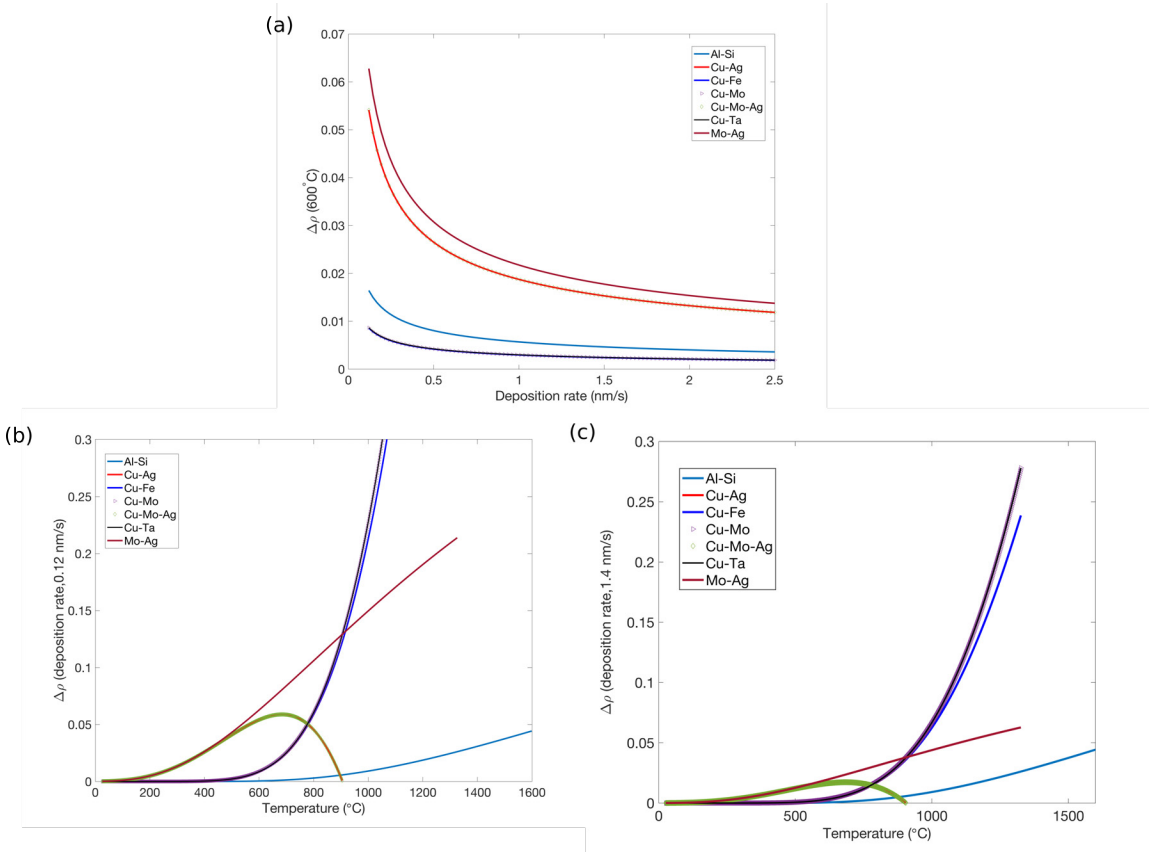

Figure 5.5: Surface diffusion length difference plots for a number of co-deposited, immscible systems: (a) surface diffusion length vs. deposition rate, (b) surface diffusion length vs. temperature (dep. rate = 0.12 nm/s), (c) and surface diffusion length vs. temperature (dep. rate =1.4 nm/s).

stituents, $\Delta\rho$, can be written as [7, 13],

$$\Delta\rho = \sqrt{\frac{(D_s)_A\delta}{\nu}} - \sqrt{\frac{(D_s)_B\delta}{\nu}}, \tag{5.3}$$

where the surface diffusivity was determined using literature values for self diffusivity for each constituent, $(D_s)_i$, and δ was assumed to be on the order of a few Angstroms.

Fig. 5.5 shows that there is a significant surface diffusion length deference between different systems depending on the deposition rate and substrate temperature. With substrate temperature kept constant at 600°C, we see that the Mo-Ag and Cu-Mo system have a large difference in surface diffusion length at low deposition rate. Comparing this to the Cu-Ag or Cu-Fe (to be introduced in the next chapter), the surface diffusion length is significantly lower. This difference decreases at higher deposition rate and constant temperature. A similar trend is observed at constant deposition rate and changing substrate temperature. These plots alongside the empirical evidence shown in this Chapter suggest that when the difference between surface diffusion length is high, the final film morphology will be hierarchical. When the difference in surface diffusion length is low, a homogeneous morphology would result.

When the difference in surface diffusion length is low, a dichotomy in phase separation processes occurs. As shown in Fig. 4.1 in Chapter 4, the constituent with a greater surface diffusion length (e.g. Cu in Cu-Mo at low deposition rate), will agglomerate and lead to a composition difference across the surface. The majority

phase agglomerates into a larger domain while the minority phase is "trapped inside" (e.g. Mo precipitates in the Cu domains). This is similar to the work done on the Cu-W, in which when a large dichotomy in the phase fraction of binary constituents led to a random distribution of the minority phase in larger domains of the other phase [1].

The matrix phase surrounding these agglomerates seems to develop similar to that process described in Chapter 3 for the homogeneous cases in regions where the phase fraction is still equal.

Much work is still required to determine the requisite parameters that need to be considered when trying to predict which deposition conditions will lead to a hierarchical phase separated structure.

5.4 Conclusions

In summary, we have deposited a series of immiscible systems with varying thermodynamic and kinetic properties under a number of deposition conditions. Depending on the system and deposition conditions, homogeneous and hierarchical morphologies resulted. For systems with large difference in surface diffusion length (i.e. Cu-Mo and Mo-Ag), a hierarchical structure was observed at certain deposition temperatures and rates. For other systems (e.g. Cu-Ag), a homogenous phase separated structure was present at all deposition conditions studied. This was a result of a low difference in surface diffusion length for the deposition conditions tested.

References

[1] FTN Vüllers and Ralph Spolenak. From solid solutions to fully phase separated interpenetrating networks in sputter deposited immiscible w–cu thin films. *Acta Materialia*, 99:213–227, 2015.

[2] Yong Lu, Cuiping Wang, Yipeng Gao, Rongpei Shi, Xingjun Liu, and Yunzhi Wang. Microstructure map for self-organized phase separation during film deposition. *Physical review letters*, 109(8):086101, 2012.

[3] Michael Atzmon, DA Kessler, and DJ Srolovitz. Phase separation during film growth. *Journal of applied physics*, 72(2):442–446, 1992.

[4] B. Derby, Y. Cui, J.K. Baldwin, and A. Misra. Effects of substrate temperature and deposition rate on the phase separated morphology of co-sputtered, cu-mo thin films. *Thin Solid Films*, 647:50–56, 2018.

[5] B. Cantor and R.W. Cahn. Metastable alloy phases by co-sputtering. *Acta Metallurgica*, 24(9):845–852, 1976.

[6] C.D. Adams, M. Atzmon, Y.T. Cheng, and D.J. Srolovitz. Phase separation during co-deposition of al–ge thin films. *Journal of Materials Research*, 7(3):653–666, 1992.

[7] K. Fukutani, K. Tanji, T. Saito, and T. Den. Phase-separated al–si thin films. *Journal of Applied Physics*, 98(3):033507, 2005.

[8] K. Ankit, B. Derby, R. Raghavan, A. Misra, and M.J. Demkowicz. 3-d phase-field simulations of self-organized composite morphologies in physical vapor deposited phase-separating binary alloys. *Journal of Applied Physics*, 126(7):075306, 2019.

[9] B. Derby, Y. Cui, J.K. Baldwin, R. Arróyave, M.J. Demkowicz, and A. Misra. Processing of novel pseudomorphic cu–mo hierarchies in thin films. *Materials Research Letters*, 7(1):1–11, 2019.

[10] H. Mehrer. Diffusion in solid metals and alloys. *Landolt-Börnstein numerical data and functional relationships in science and technology, Group III*, 26, 1990.

[11] H. Okamoto and T.B. Massalski. Binary alloy phase diagrams. *ASM International, Materials Park, OH, USA*, 1990.

[12] S.K. Sharma and J. Spitz. Hillock formation, hole growth and agglomeration in thin silver films. *Thin Solid Films*, 65(3):339–350, 1980.

[13] S.Y. Hu and L.Q. Chen. Spinodal decomposition in a film with periodically distributed interfacial dislocations. *Acta Materialia*, 52(10):3069–3074, 2004.

CHAPTER VI

Metal-ion-controlled Growth of 3D Bicontinuous Cu/Fe Morphologies

6.1 Introduction

The final thin film morphology of co-sputtered, immiscible materials, such as Cu and Fe, depends on the energy of the condensing adatoms on the substrate surface [1, 2]. The energy of these adatoms is largely determined by potential forces such as the substrate bias and the temperature applied to the substrate [3]. It was found that control over the direction of phase separation can be governed by manipulating the energy of adatoms through the deposition rate and temperature [4]. Specifically, deposition temperature and rate determine the balance between competing effects of phase separation and co-deposition-induced mixing. [5].

Deposition of phase separating materials at elevated temperatures has been well researched. The seminal work by Atzmon *et. al.* showed that the domain size of a phase separated thin film morphology is dependent on the interdiffusion length of the adatoms arriving on the growing surface [6]. The authors expressed the surface

interdiffusion length as,

$$\rho = \sqrt{\frac{D_s \delta}{\nu}}, \tag{6.1}$$

where D_s is the surface interdiffusivity, δ is a atomic layer of freshly deposited material, and ν is the deposition rate. Adams verified these conclusions by co-depositing the Al-Ge system [2].

Lu and coworkers, through a phase field simulation, observed that the surface diffusion length described by Atzmon is actually describing a competition between the rate of phase separation (the numerator term in Eq. 6.1) and the rate of deposition (the denominator term in Eq. 6.1) [1]. They discovered that depending on which rate is faster, the directionality of the phase separated domains can be altered. At one extreme, when the rate of phase separation is higher than the deposition rate, lateral concentration modulations form. When the deposition rate is slightly higher than the phase separation rate, vertical concentration modulations were predicted to form. At the other extreme, random conentration modulation form if the deposition rate is significantly faster than the rate of phase separation.

Many experimental results have supported the model put forth by Atzmon and Lu. Our previous work using heated DCMS of phase separating Cu-Mo films showed the exact transition in morphology as predicted by Lu and coworkers' phase field simulation prediction [4]. Sarakinos *et. al.* showed that the atomic arrangement and interfaces in the Cu-Ag and Ag-Mo systems can be precisely controlled via

the deposition properties [7–9]. In all of these experiments and simulations, it was concluded that the energy of the adatoms was the determining factor that defined the resultant phase separated morphology.

In this Chapter, we look specifically at how maniupulating the kinetic energy of adatoms beyond substrate temperature, substrate bias, and deposition rate, affects the nanoscale morphology of phase separating thin films [10]. High-power impulse magnetron sputtering (HiPIMS), a relatively new introduction to the sputtering community, is an energetic deposition technique during which a highly ionized flux condenses on the substrate surface [11]. Very large ion fluxes of sputtered metallic species is the source of the benefits provided by HiPIMS [12].

High power densities during HiPIMS ionizes the target material in the plasma. These ionized metallic species are highly energetic and induce ion etching during sputtering [13]. The benefit of using of metal ions instead of process gas ions used in radio frequency (RF) biasing of the substrate, is that metal ions that become included into the film do not lead to detrimental gaseous voids, but instead simply incorporate into the metal film. In RF biasing using Ar ions, Ar often becomes trapped as gaseuous inclusions into the film, leading to detrimental stress in the resultant structure [14].

While the HiPIMS technique has been extensively studied for single phase materials, a fundamental understanding of how adding kinetic energy through HiPIMS to co-sputtered immiscible metals such as Cu and Fe influences the phase separated

morphology remains outstanding. It is hypothesized that the added energy supplied by HiPIMS will result in nanoscale morphology changes when compared to depositing the same system using DC magnetron sputtering (DCMS). In this work, we test this hypothesis by co-depositing a Cu-Fe model system under a specific set of deposition conditions. We then apply the same deposition conditions to the Cu-Fe system but instead use a HiPIMS power supply and compare the resultant morphologies. We show that we can alter both the microscale and nanoscale morphology as a function of target material ion current. We reason our findings using an energetic model describing the adatom kinetics on the surface of the substrate. The methodology for this experiment was outlines in Chapter 2.

6.2 Micro and Nano-scale Morphology Changes as a Function of Ion Current Using HiPIMS

At a substrate temperature of 300 °C, phase separation was activated to decompose Cu and Fe species into domains of like phase. This can be seen in Figure 6.1, which shows HAADF images of a co-sputtered Cu-Fe system on an amorphous SiO_2 substate. Ankit *et. al.* [5] predicted that if the deposition conditions were such that the rate of phase separation was faster as compared to material flux, lateral concentration modulations (LCMs) of each phase would be the resultant morphology in three dimensions. LCMs of Cu and Fe that extended from the substrate to the film surface were observed as seen in the cross section STEM image presented in Fig. 6.1b.

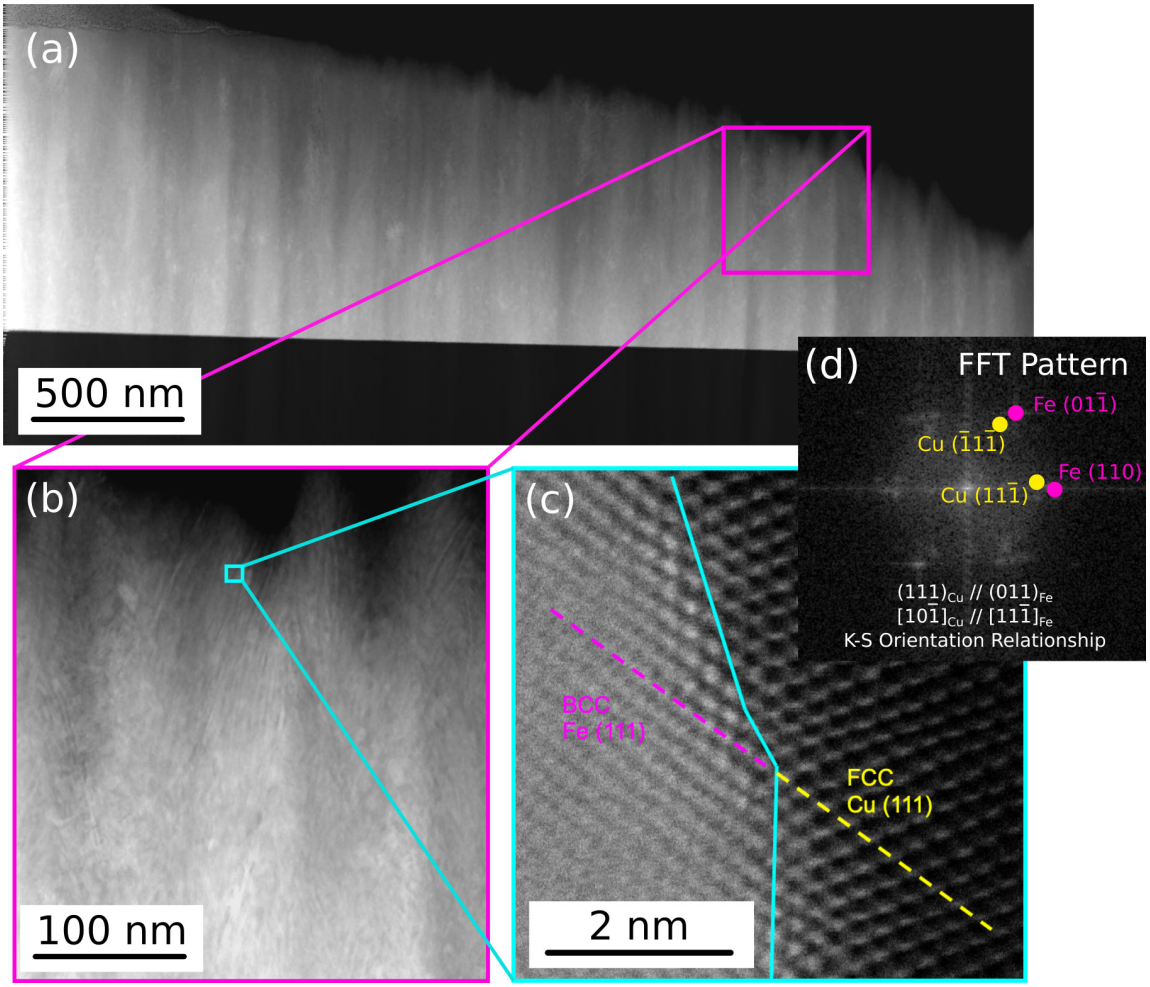

Figure 6.1: High Angle Annular Dark Field (HAADF) Images of a DCMS, co-deposited Cu, Fe sample at 300 °C and equal phase fraction. A low magnification view of the sample is shown in (a). A magnified image showing the lateral concentration modulations of Cu and Fe phase domains is shown in (b). An atomically resolved image of the sample alongside a corresponding FFT is shown in (c-d). The FFT pattern shows a Kurdjumov-Sachs orientation relationship between the FCC Cu and BCC Fe phases.

This was determined by the phase contrast shown in the figure (e.g. Cu-rich phase is brighter than Fe-rich phase). The plan-view image of the sample showed that grains containing phase separated Cu and Fe domains in a tortuous morphology. High resolution imaging showed that the Cu was in the face-centered cubic (FCC) crystal structure and the Fe was in the body-centered cubic (BCC) crystal structure. The interface between the FCC Cu and BCC Fe is shown in Fig. 2.2c. The orientation relationship as confirmed using fast-Fourier transformation was observed to be Kurdjumov-Sachs where $(111)_{\mathrm{fcc}}$ is parallel to $(011)_{\mathrm{bcc}}$ and $[10\bar{1}]_{\mathrm{fcc}}$ is parallel to $[11\bar{1}]_{\mathrm{bcc}}$.

A negligible number of Cu and Fe sputtered species were ionized during DCMS, and thus the final morphology was determined by the fixed kinetic energy of the adatoms supplied by the deposition temperature and material flux.

Kinetic energy can be added to the sputtered species by ionizing the vaporized target atoms through HiPIMS. The average energy per deposited atom was defined by Petrov and coworkers as [15],

$$< E_d >= E_i J_i / J_m, \tag{6.2}$$

where E_i is the average energy of ions, and J_i/J_m is the ratio of the energetic ion flux to the flux of condensing atoms.

To understand the effects of adding kinetic energy to the Cu and Fe adatoms, this same system was deposited using HiPIMS. Three different Fe ion currents were

selected to adjust the kinetic energy of the condensing Cu and Fe atoms as listed in Table 2.2. The temperature of the substrate was kept the same in order to compare the resultant morphologies to the DCMS sample. Cross-section TEM images of each morphology as a function of ion current are shown in Fig. 6.2.

Porosity was observed in all of the samples deposited with HiPIMS as shown in Fig. 6.2 (b-d). When viewing the sample on the microscale, large columnar grains approximately 200 nm in lateral dimension and extending from the substrate to the film surface developed during growth. Inter-columnar voids separated each of the columns at low Fe and Cu ion currents. As shown in Fig. 6.2(c), the porosity was reduced but a columnar structure was still observed. The sample was most dense nearest to the substrate surface, and then developed into a columnar structure beginning at approximately 175 nm in thickness. The column lateral length remained similar to that at lower ion currents (i.e. Fig. 6.2(b)). Finally, Fig. 6.2(d) shows that the density of the film was enhanced at the highest target currents studied. The film did exhibit porosity to a lesser extent than the previous films beginning at 500 nm film thickness. The highest Fe and Cu ion currents achieved with HiPIMS power gave rise to the largest lateral column dimensions of approximately 300 nm. In summary, increasing the ion current for each species lead to a significant decrease in the film porosity.

To achieve a significant level of ionization of the target species in the plasma, high pressures are required in HiPIMS [16]. For the Cu and Fe metals deposited in this

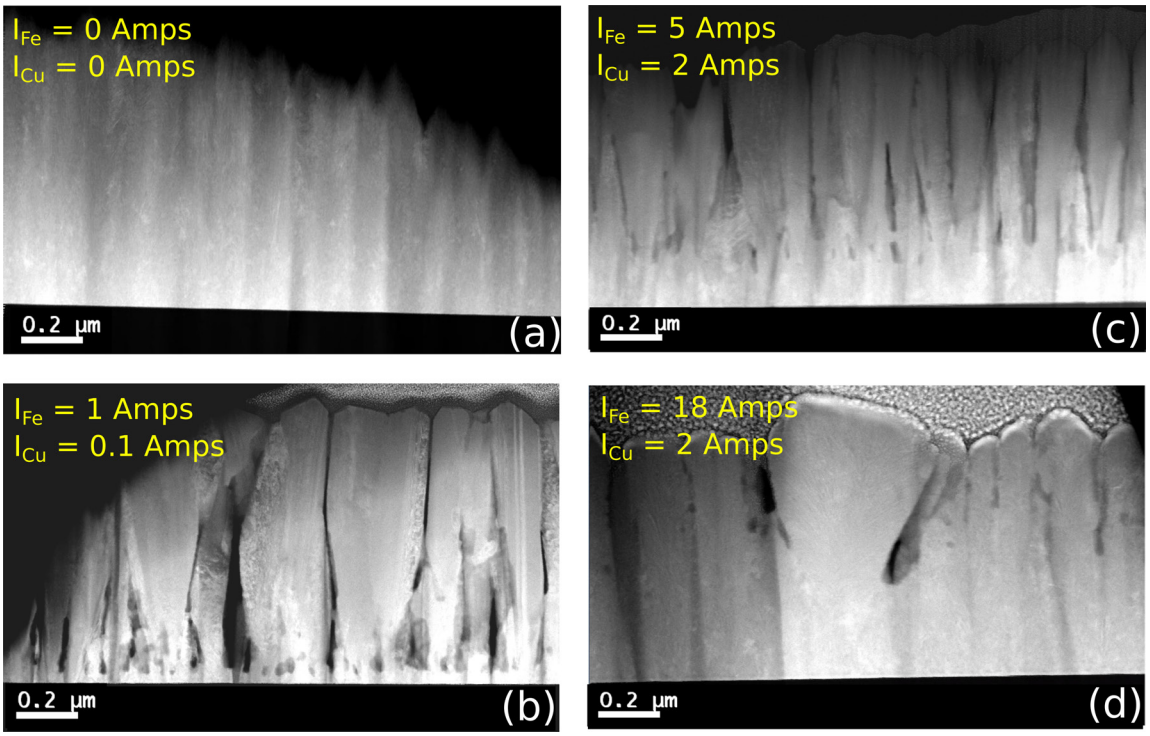

Figure 6.2: Cross sectional HAADF TEM images of Cu,Fe films grown by (a) DCMS and (b-d) HiPIMS. The columnarity and porosity of the film is reduced at higher ion currents in the HiPIMS-deposited samples.

work, a range of different gas pressures were tested to determine the best working gas pressure that would achieve a high level of ionization for Cu and Fe species in the plasma. High gas pressures, though, during deposition increases the likelihood of ion scattering events in the plasma. This reduces the energy of the arriving adatoms on the growing film surface and tends to drive tensile stress in the film [17]. This most likely explains the reason for the significant columnar porosity observed in the HiPIMS samples. In future, we will explore depositing at lower gas pressure, but higher potential to achieve the same ion currents studied here.

The effects of co-sputtering with HiPIMS was more pronounced in the self-organized nanoscale morphologies in the intra-columnar phase separated regions. Adding energy to the condensing adatoms on the surface of the growing film was expected to alter the phase separation mechanisms through the surface diffusion length. Characterizing the sample in S/TEM showed that an evolution in phase separation direction occurred as a function of ion current. Fig. 6.3 shows highly magnified S/TEM images of the samples presented in Fig. 6.2. Using a convergence angle of 111 degrees in the S/TEM, darker regions in the image indicated a lower atomic number material; in this case, Fe. Brighter regions indicate regions higher in Cu concentration.

As previously noted, lateral domains of Cu- and Fe- rich were observed when the species were co-sputtered using DCMS and ion current was negligible as shown in Fig. 6.3(a). As shown in Fig. 6.3(c), when Cu and Fe ion current was introduced at 0.5 amperes and 1 ampere, respectively, refined vertical concentration modulations

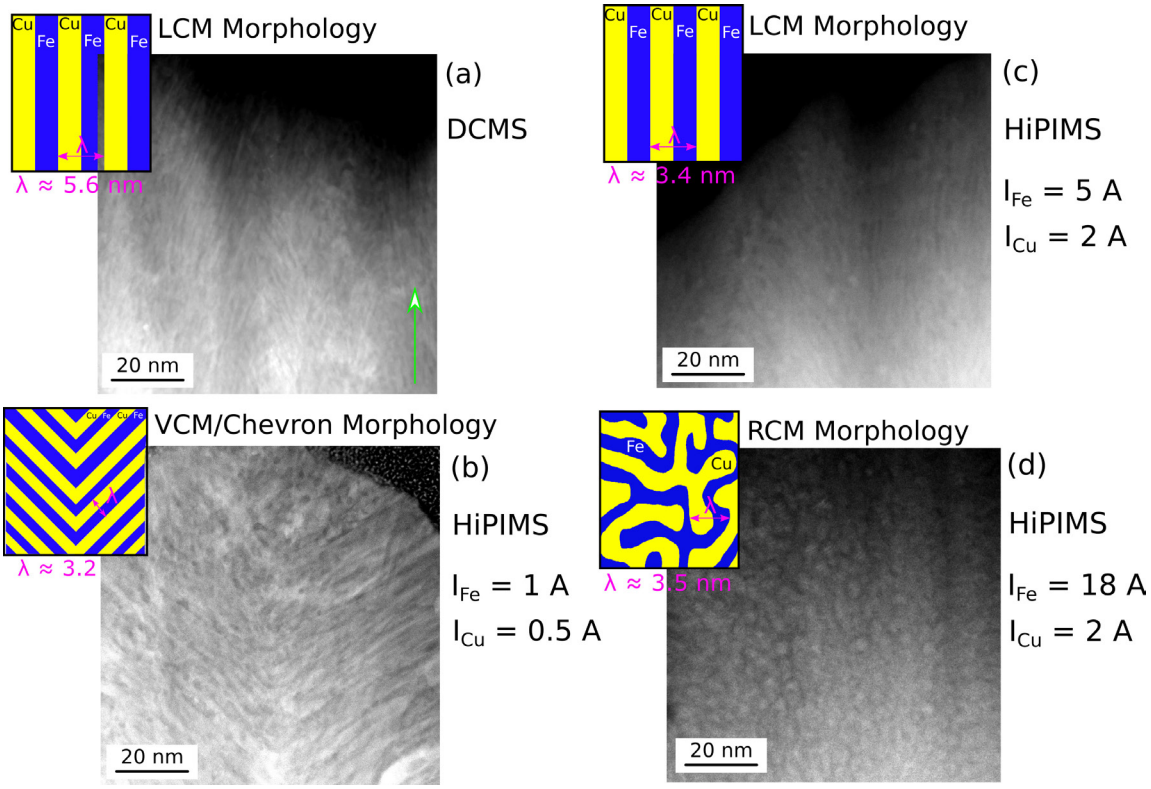

Figure 6.3: Cross sectional HAADF TEM images of Cu,/Fe films grown by (a) DCMS and (b-d) HiPIMS. The directionality of the phase separated structure evolves as a function of target current. The concentration modulations randomize with increasing ion current. The film growth direction is shown by the white arrow in the image.

(VCM) of Cu- and Fe- rich domains were exhibited. Fig. 6.3(b) shows that Cu and Fe atoms phase separated parallel to the growth direction forming vertical striations of Cu- and Fe- rich domains. The concentration modulation wavelength, was measured to be 5.6 ± 0.3 nm. while the wavelength in Fig. 6.3(b) was measured to be 3.2 ± 0.2 nm. These vertical domains were not observed to extend across the growth column, but instead formed a chevron like pattern branching from the center line of the column.

A noticeable change to the nanoscale morphology was observed when the Fe and Cu ion current was increased to 5 amperes and 2 amperes, respectively. In this case, the Cu and Fe domains were phase separated normal to the film growth direction into lateral concentration modulations (LCM) with a wavelength of 3.4 ± 0.3 nm.

At the highest ion currents studied in this work, 18 amperes of Fe ion current and 2 amperes of Cu ion current, the most significant change in nanoscale morphology was observed. In this case, the added surface diffusion length allowed for the LCM domains to interconnect and form randomly distributed domains of Cu and Fe. Fig.6.3(d) shows the random concentration modulations (RCM) of Cu- and Fe-rich domains.

Considering just the samples deposited with HiPIMS, we see a transition in morphology from VCM to LCM to RCM as a function of ion current. We use this change in energy of arriving adatoms to develop an surface diffusion model to explain these morphologies.

6.3 Discussion

Thin film morphology depends solely on the deposition conditions used during processing [18]. Deposition conditions, including deposition rate and substrate temperature, define the surface and bulk diffusion processes that control film microstructure [19]. Single phase thin film structure was first defined by the growth temperature normalized by the melting temperature of the deposited material, or

$$T_h = \frac{T}{T_m}. \tag{6.3}$$

At low temperatures, adatom mobility is small, and the nucleation rate of grains is high so fine-grained fibrous grains result [20]. At high temperatures, bulk diffusion is activated and so the resultant film is dense with equiaxed grains. These empirical data led to the development of a structural zone diagram (SZD) dependent on temperature [17]. This model was later improved upon by Thornton *et al.* when process gas pressure was included. Increases in gas pressure contracted the zones outlined in the diagram as sputtered atoms scattered off of neutral process gas atoms [21].

The substrate temperature provided kinetic energy to the adatoms landing on the growing film surface [22]. Ionized metal species bombarding the substrate surface, however, have energy that is kinetic in nature since they displace and heat the film [11]. For single phase materials, extra kinetic energy from ion bombardment allows for transition between structural zones to occur at lower temperatures [23]. This is sourced from the energetic species on the order of 10s of eVs [24] being more energetic

than their neutral counterparts and thus having a longer surface diffusion length [25–27]. In chromium nitride-based coatings it was found that ion bombardment from HiPIMS induced re-nucleation of grains similar to that structure found in zone III of the SZD even at room temperature [23].

In this work, we observed a change in both the Cu-Fe microscale and nanoscale morphology. The densification of the microscale Cu-Fe morphology as a function of ion current energy is similar to those findings for single phase materials as shown in Fig. 6.2. Porosity was found when HiPIMS was introduced. This is most likely due to high process gas pressure as predicted by [28]. The film became denser as the Fe and Cu ion current increased. As multiple *in situ* studies have shown, some of the energetic species do subplant into the growing film, but most condense onto the surface. [26, 27]. The increased surface diffusion length of the ionized species arriving on the growing film led to renucealtion events and suppressed the formation of fibrous grains, similar to the findings on chromium nitride films deposited using HiPIMS [29]. It may at first seem that these two ideas are inconsistent. Muller *et. al.* predicts a lower momentum for impinging species when the process gas pressure is high due to scattering [28]. On the other hand ionized species reaching the growing film surface have increased momentum as predicted by Anders [11]. We hypothesize that this is not an inconsistency when considering that some of the positively charged ions will reach the substrate despite the higher gas pressure and will have an increased momentum as predicted. This hypothesis is supported by the TEM data presented

in this work. The macroscopic porosity is a result of a majority of sputtered neutrals and ions losing momentum and cause porosity in the film. Since some of the ions with increased momentum reach the substrate, the nanoscale morphology can still change. This possible inconsistency is planned on being addressed in future experimentation when a quantification of the species arriving on the substrate can be elucidated.

The question remaining to be answered is how HiPIMS could change the nanoscale Cu-Fe phase separated morphology. Both empirical and theoretical findings on DCM sputtered immiscible binary systems, show that a competition between the surface diffusion length and the deposition rate determine the final phase separated morphology in these systems [4, 5].

As Lu and coworkers point out, when the rate of phase separation is high relative to the deposition rate, the species have enough time to phase separate into domains with the terminal composition predicted by the phase diagram [1]. As more material is added, like species diffuse to like domains and an LCM geometry in formed. When the deposition rate is comparable to surface diffusion length, a VCM morphology develops [1].

To begin our analysis, we assume the empirical evidence as shown by Patsalas *et. al.* that most of the ionized species have increased surface diffusion length. To approximate the surface diffusion length, we take the kinetic energy equation

described by Anders and colleagues as,

$$E_{\text{kin}} = E_0 + QeV_{\text{sheath}}, \tag{6.4}$$

where E_0 is the initial kinetic energy component of the plasma, Q is the ion charge state number, e is the elementary charge, and V_{sheath} is the voltage drop between the plasma and the substrate surface [11]. The product, QeV_{sheath} is the energy change due to acceleration in the sheath. We are free to then set $E_{\text{kin}} = \frac{1}{2}mv^2$, where m is the mass of the arriving adatom, and v is the approximate velocity in a direction normal to the growth direction [30]. Setting these two equations equal we have,

$$\begin{aligned} E_{\text{kin}} &= E_0 + QeV_{\text{sheath}} \\ &= \frac{1}{2}mv^2 \end{aligned} \tag{6.5}$$

Therefore we can determine the velocity of adatoms, ν, as

$$v = \sqrt{\frac{2E_0 + 2QeV_{\text{sheath}}}{m}}. \tag{6.6}$$

Since we know the deposition rate and the thickness of one layer of material, we can approximate the residence time of an adatom on the growing surface. The deposition rate for the HiPIMS samples was approximately 1.5 $\mathring{A}$/s and the average thickness of a Cu and Fe atomic layer is 1.33 $\mathring{A}$. Thus the approximate residence

Table 6.1: Table of inputs for Eq. 6.6

Input Variable	Value	Cu Ion Value	Fe Ion Value	Reference
Initial Energy of Plasma, E_0 [C]	1.6E-18			[31]
Ion Charge State Number, Q		2	3	[32]
Elementary charge, e [C]	1.6E-19			[33]
Mass, m [kg]		1.05E-25	9.3E-26	[33]

time of an adatom of the growing surface is 1s. Using this we can determine the surface diffusion length of an adatom as a function of ion energy.

We compiled Table 6.1 to show the values of the inputs used to determine the surface diffusion length as a function of ion current. Using these inputs, a plot of surface diffusion length as a function of sheath voltage can be graphed. Fig. 6.4 shows this plot.

Fig. 6.4 shows that at the highest ion currents studied in this work, the surface diffusion length is approximately 25 nm, which is approximately four times that found for DCMS, which has negligible ion current.

Despite the constant temperature, the increased surface mobility allows the film to access the same transition in film morphology found in the Cu-Mo system [4]. Since the deposition rate remains constant, the surface diffusion rate tends to be higher than the deposition rate. This led to the development of the LCM morphology when the surface diffusion rate was larger than the deposition rate. Eventually the RCM morphology was observed at the highest ion currents when the deposition rate was negligible compared the surface diffusion rate.

A qualitative reasoning for the change in morphology is shown in Fig. 6.5. During DCMS sputtering shown in Fig. 6.5(a), we see that approximately all of the condensing atoms are neutral with a mobility (arrow in image) defined by the gas pressure and the substrate temperature. When we ionize a significant portion of the condensing Cu and Fe atoms, they become much more energetic than their neutral

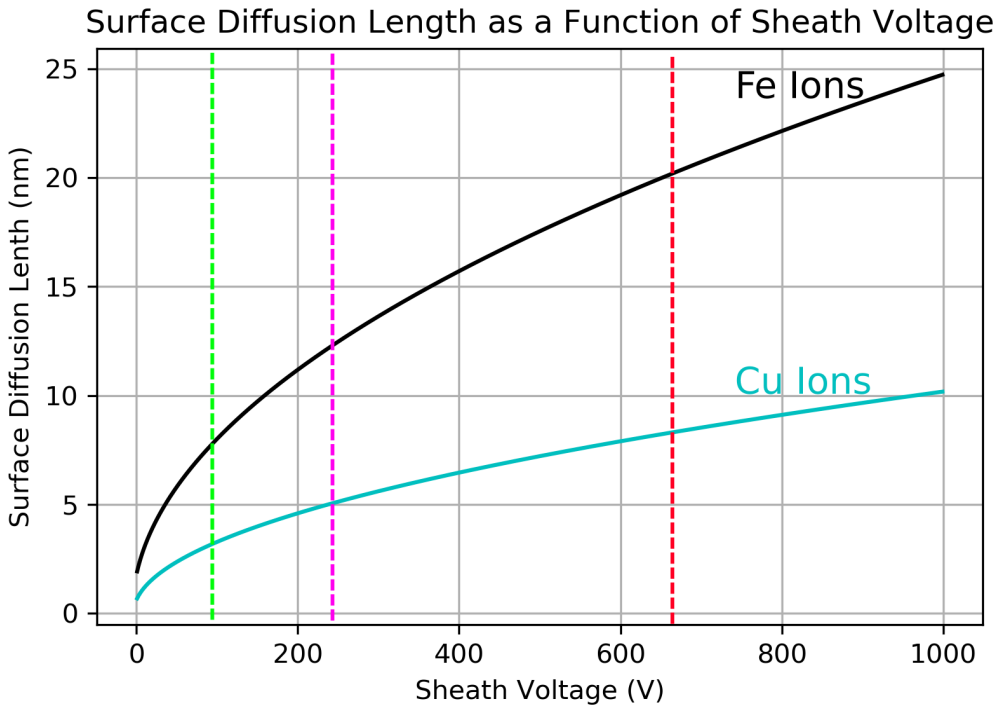

Figure 6.4: A plot of the surface diffusion length of condensed Cu and Fe adatoms as a function of voltage sheath. The voltage defines the ion current for each target. The surface length increases as a function of Cu and Fe ion current.

counterparts and enhance surface mobility on the growing surface. Unlike single phase HiPIMS, we have two ionized species contributing to the growth. The effect of the enhanced surface mobility is shown in Fig. 6.5(c), which is a highlighted view of the surface phenomena demarcated in the box in Fig. 6.5(b).

At "time step 1," condensed neutral adatoms have a mobility defined by the substrate temperature and gas pressure in the chamber. Ionized species, however, have an enhanced surface mobility that is larger than that describing the neutral adatoms. The Cu and Fe adatoms attempt to form an LCM structure on the substrate surface, but it's full formation is stunted when energetic Cu and Fe ions knock atoms to different positions in the structure. Tracking four example atoms, 1-4, we see that the energetic Cu and Fe ions knock previously deposited atoms to alternate positions, and then get incorporated into the film as neutrals in time step 3. These positions are random and lead to the development of an RCM-like structure as the film grows in time step 4.

The important distinction of this work compared to our previous work on Cu-Mo morphologies is that we are able to access new morphologies at a constant temperature. In the Cu-Mo, the RCM morphology was only observed at high substrate temperatures. This also coarsened the nanoscale morphology. By accessing the RCM morphology in the Cu-Fe at low temperature, the length scale could be maintained.

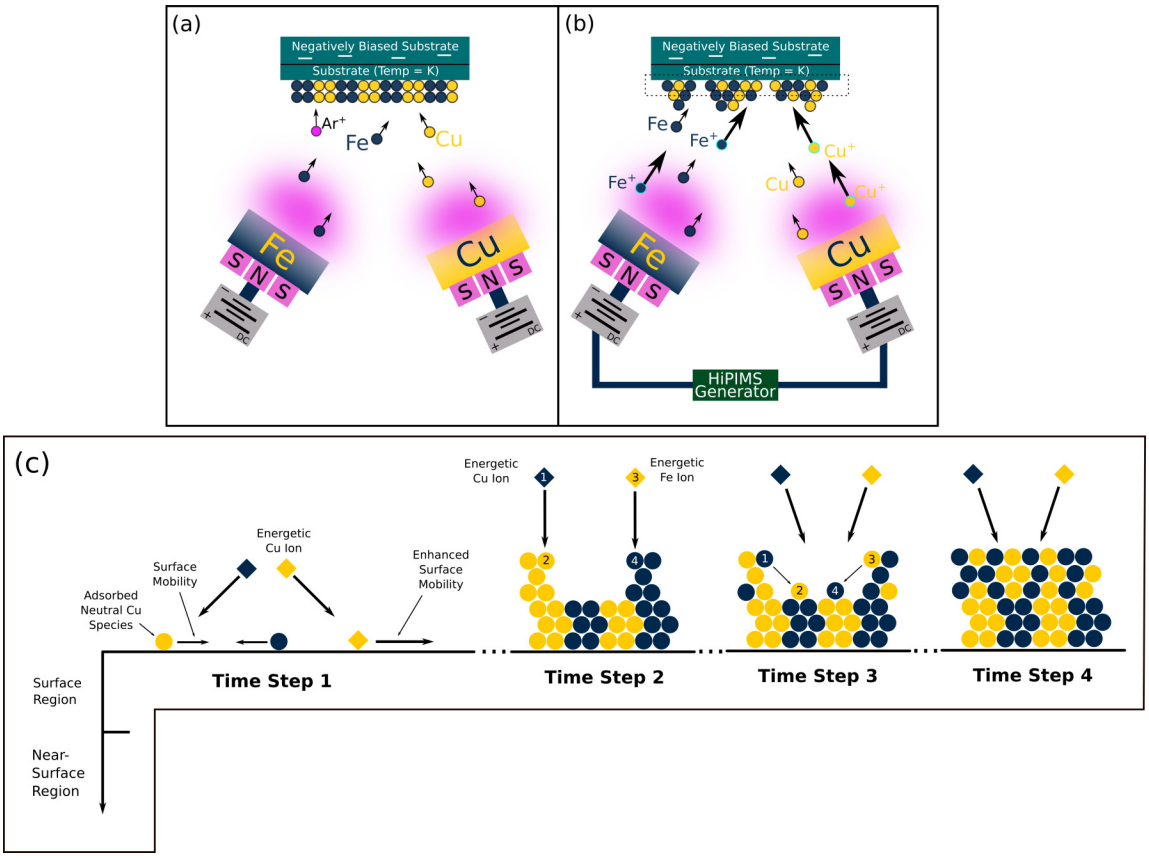

Figure 6.5: A cartoon schematic describing the difference between DCMS (a) and HiPIMS (b). Metal species become ionized using HiPIMS and are highly energetic. This kinetic energy increases the surface diffusion length when they condense on the substrate surface. The effect of this added surface diffusion length is shown in (c). The energetic Cu and Fe ions knock off previously deposited species and randomize the morphology. Atoms 1-4 are just example atoms to guide the eye. Diamonds represent metal ions and circles represent metal neutrals. Initially: atom 1 is a Cu ion, atom 2 is a neutral Cu, atom 3 is a Mo ion, and atom 4 is a neutral Mo.

6.4 Conclusions

In this work, we describe a transition in bicontinuous Cu and Fe morphologies depending on the ion current during HiPIMS. A co-sputtered sample deposited using DCMS, was observed to be in a LCM morphology with a modulation wavelength of 5.6 nm. Introducing Cu and Fe ions to the deposition using HiPIMS, the nanoscale morphology transitioned from VCM to LCM to RCM depending on the ion current. The ionized species condense on the substrate surface are highly energetic and have an increased surface diffusion length. Since nanoscale morphology in immiscible thin film systems is highly dependent on the surface diffusion length, the nanoscale morphology was altered as a function of ion current. At low ion current, Cu and Fe domains forming the morphology were observed to be in vertical striations. At higher ion currents, the Cu and Fe domains were observed to transition from LCM to an RCM morphology.

Given the added energy that HiPIMS imparts on the incoming sputtered flux, this technique is a good candidate for solving an outstanding scientific issue in the DCMS community: synthesizing nanometer-sized, bicontinuous nanocomposites [4]. Bicontinuous morphologies are characterized by two or more tortuous and phase separated domains that extend in three dimensions [34]. In this work, we have begun to address this issue by keeping the substrate temperature constant, but changed morphology via HiPIMS, and in future work, we will extend this study to other immisicible systems as well as explore the nanomechanical behavior of the new mor-

phologies possible with HiPIMS. In the future, substrate temperature effects will be elucidated by altering the substrate temperature during HiPIMS. A coarsening of the morphologies and a change in direction of the phase separated domains is expected as shown in our previous work using DCMS [35].

References

[1] Y. Lu, C. Wang, Y. Gao, R. Shi, X. Liu, and Y. Wang. Microstructure map for self-organized phase separation during film deposition. *Physical Review Letters*, 109(8), Aug 2012.

[2] C.D. Adams, M. Atzmon, Y-T. Cheng, and D.J. Srolovitz. Phase separation during co-deposition of alge thin films. *Journal of Materials Research*, 7(03):653666, Mar 1992.

[3] J.A. Thornton. Influence of apparatus geometry and deposition conditions on the structure and topography of thick sputtered coatings. *Journal of Vacuum Science and Technology*, 11(4):666670, Jul 1974.

[4] B. Derby, Y. Cui, J.K. Baldwin, and A. Misra. Effects of substrate temperature and deposition rate on the phase separated morphology of co-sputtered, cu-mo thin films. *Thin Solid Films*, 647:5056, Feb 2018.

[5] K. Ankit, B. Derby, R. Raghavan, A. Misra, and M.J. Demkowicz. 3-d phase-field simulations of self-organized composite morphologies in physical vapor deposited phase-separating binary alloys. *Journal of Applied Physics*, 126(7):075306, Aug 2019.

[6] M. Atzmon, D.A. Kessler, and D.J. Srolovitz. Phase separation during film growth. *Journal of Applied Physics*, 72(2):442–446, 1992.

[7] V. Elofsson, G.A. Almyras, B. Lü, M. Garbrecht, R.D. Boyd, and K. Sarakinos. Structure formation in ag-x (x= au, cu) alloys synthesized far-from-equilibrium. *Journal of Applied Physics*, 123(16):165301, 2018.

[8] V. Elofsson, G.A. Almyras, B. Lü, R.D. Boyd, and K. Sarakinos. Atomic arrangement in immiscible ag–cu alloys synthesized far-from-equilibrium. *Acta Materialia*, 110:114–121, 2016.

[9] K. Sarakinos, G. Greczynski, V. Elofsson, D. Magnfält, H. Högberg, and B. Alling. Theoretical and experimental study of metastable solid solutions and phase stability within the immiscible ag-mo binary system. *Journal of Applied Physics*, 119(9):095303, 2016.

[10] B.K. Derby and A. Misra. Metal-ion-controlled growth of 3d bicontinuous cu/fe morphologies. *Journal of Applied Physics*, 2020.

[11] A. Anders. A structure zone diagram including plasma-based deposition and ion etching. *Thin Solid Films*, 518(15):40874090, May 2010.

[12] A. P. Ehiasarian, J. G. Wen, and I. Petrov. Interface microstructure engineering by high power impulse magnetron sputtering for the enhancement of adhesion. *Journal of Applied Physics*, 101(5):054301, Mar 2007.

[13] J. Alami, J.T. Gudmundsson, J. Bohlmark, J. Birch, and U. Helmersson. Plasma dynamics in a highly ionized pulsed magnetron discharge. *Plasma Sources Science and Technology*, 14(3):525531, Aug 2005.

[14] D. Lundin and K. Sarakinos. An introduction to thin film processing using high-power impulse magnetron sputtering. *Journal of Materials Research*, 27(5):780792, Mar 2012.

[15] I. Petrov, F. Adibi, J.E. Greene, L. Hultman, and J-E Sundgren. Average energy deposited per atom: A universal parameter for describing ion-assisted film growth? *Applied Physics Letters*, 63(1):36–38, 1993.

[16] A. Anders, J. Andersson, and A. Ehiasarian. High power impulse magnetron sputtering: Current-voltage-time characteristics indicate the onset of sustained self-sputtering. *Journal of Applied Physics*, 102(11):113303, Dec 2007.

[17] M. Ohring. *The Materials Science of Thin Films*. Academic, 2002.

[18] R.F. Bunshah and C. Weissmantel. *Handbook of Hard Coatings: Deposition Technolgies, Properties and Applications*. Materials science and process technology series. Elsevier Science, 2001.

[19] P.B Barna and M. Adamik. Fundamental structure forming phenomena of polycrystalline films and the structure zone models. *Thin Solid Films*, 317(12):2733, Apr 1998.

[20] B.A. Movchan and A.V. Demchishin. Structure and properties of thick condensates of nickel, titanium, tungsten, aluminum oxides, and zirconium dioxide in vacuum. *Fiz. Metal. Metalloved. 28: 653-60 (Oct 1969).*, 1 1969.

[21] J.A. Thornton. Influence of substrate temperature and deposition rate on structure of thick sputtered cu coatings. *Journal of Vacuum Science and Technology*, 12(4):830835, Jul 1975.

[22] J. Alami, K. Sarakinos, F. Uslu, and M. Wuttig. On the relationship between the peak target current and the morphology of chromium nitride thin films deposited by reactive high power pulsed magnetron sputtering. *Journal of Physics D: Applied Physics*, 42(1):015304, Jan 2009.

[23] A.P Ehiasarian, P.Eh Hovsepian, L. Hultman, and U. Helmersson. Comparison of microstructure and mechanical properties of chromium nitride-based coatings deposited by high power impulse magnetron sputtering and by the combined steered cathodic arc/unbalanced magnetron technique. *Thin Solid Films*, 457(2):270277, Jun 2004.

[24] A. Anders. A review comparing cathodic arcs and high power impulse magnetron sputtering (hipims). *Surface and Coatings Technology*, 257:308–325, 2014.

[25] L. Hultman, J-E Sundgren, J.E. Greene, D.B. Bergstrom, and I. Petrov. High-flux low-energy (20 ev) n+ 2 ion irradiation during tin deposition by reactive magnetron sputtering: Effects on microstructure and preferred orientation. *Journal of Applied Physics*, 78(9):5395–5403, 1995.

[26] P. Patsalas, C. Gravalidis, and S. Logothetidis. Surface kinetics and subplantation phenomena affecting the texture, morphology, stress, and growth evolution of titanium nitride films. *Journal of Applied Physics*, 96(11):6234–6246, 2004.

[27] P. Patsalas and S. Logothetidis. In-situ monitoring of the electronic properties and growth evolution of tin films. *Surface and Coatings Technology*, 180:421–424, 2004.

[28] K. Müller. Stress and microstructure of sputter-deposited thin films: Molecular dynamics investigations. *Journal of Applied Physics*, 62(5):1796–1799, 1987.

[29] G. Greczynski, J. Jensen, J. Bhlmark, and L. Hultman. Microstructure control of crnx films during high power impulse magnetron sputtering. *Surface and Coatings Technology*, 205(1):118130, Sep 2010.

[30] X.W. Zhou, R.A. Johnson, and H.N.G. Wadley. A molecular dynamics study of nickel vapor deposition: Temperature, incident angle, and adatom energy effects. *Acta Materialia*, 45(4):15131524, Apr 1997.

[31] B. Chapman. *Glow discharge processes: sputtering and plasma etching*. Wiley, 1980.

[32] A. Anders. A periodic table of ion charge-state distributions observed in the transition region between vacuum sparks and vacuum arcs. *IEEE Transactions on Plasma Science*, 29(2):393398, Apr 2001.

[33] B.N. Taylor, P.J. Mohr, and M Douma. The nist reference on constants, units, and uncertainty. *available online from:. physics. nist. gov/cuu/index*, 2007.

[34] L. E. Scriven. Equilibrium bicontinuous structure. *Nature*, 263(5573):123125, Sep 1976.

[35] B. Derby, Y. Cui, J.K. Baldwin, and A. Misra. Effects of substrate temperature and deposition rate on the phase separated morphology of co-sputtered, cu-mo thin films. *Thin Solid Films*, 647:50–56, 2018.

CHAPTER VII

Bicontinuous Thin Film Material Response in Extreme Irradiation Environments

7.1 Introduction

The microstructure of alloys and nanocomposites can exert significant effects on Helium (He) accumulation in metals [1, 2]. Helium is generated in metals via transmutation when used in fast and thermal spectrum reactors [3]. Features including interface spacing and shape, crystallography, defect structure, and chemistry all influence He behavior [3–5]. Studying the effects of morphology on He behavior in metals is of major importance, as He accumulated in metals can result in significant embrittlement and eventual structural failure in a wide variety of energy-related applications [3, 6].

In bulk, single phase alloys, He does not remain in solution once it is forced into the material. Instead, He will precipitate into small bubbles. The typical life cycle of He precipitates in metals starts with the supersaturation of vacancies and migration of He interstitials [3]. The cause of supersaturation is the production of vacancy-

interstitial pairs by irradiation [3]. For a cluster of vacancies to grow into a void, there must be a net increase in the number of vacancies absorbed over the number of interstitials absorbed [3]. Clustering of these He impurities and vacancies leads to the formation of He-filled cavities, or nanometer-scale bubbles, throughout the material. Capillarity defines the equilibrium shape of these bubbles and in the absence of solid-state interfaces, the bubbles grow in size as equiaxed spheres [7–9]. In general, any He trapped in such bubbles cannot escape from the material. However, as these He-filled cavities grow, they may eventually impinge on a free surfaces, releasing the trapped He, and damage the surface [6].

When solid-state interfaces are introduced in the structure, for instance in a nanolayered geometry, the life cycle of He precipitates is altered. In a material containing heterophase thin metal layers on the nanoscale, He bubbles may remain confined within individual layers. In some cases, these bubbles may decorate interfaces in regular patterns, giving rise to the appearance of bead-like bubble microstructures in a cross-section view [10]. This arrangement is driven by location-dependent interface energies on the phase boundaries [11]. It has even been observed that bubbles on the interface can coalesce into elongated channels, in some cases [12].

He retained in both bulk alloy and nanocomposite geometries alters the mechanical response of these materials under load. In general, He precipitates harden the material as the He bubbles act like dislocation pinning points [3]. He retained in the sample may also lead to embrittlement of the material.

Much of the previous research into He retention in metals has focused on either bulk alloys or multilayered nanocomposites, with some recent progress on particulate-type morphologies [13]. Nanocomposites are materials comprised of at least two phase domains. In this respect, they are distinct from nanocrystalline metals, which are polycrystalline aggregates of a single phase. The most widely studied nancomposite metals are multilayers. By contrast, the constituent phases in our materials interpenetrate each other and have complex, irregular shapes. Moreover, the interfaces between the phases are highly curved, unlike the flat (zero curvature) interfaces found in layered composites.

The effect of more complex or general nanocomposite morphologies on He accumulation has largely remained unexplored. In this work, we fill this gap by investigating the effect of nanocomposite morphology on three aspects of He response: He retention, the size and distribution of He precipitates, and He-induced changes in mechanical properties. Our goal is to carry out a basic science investigation of the effect of the morphology of constituent phases in nanocomposite metals on He precipitation and retention. While many studies on He in nanocomposite metals have been carried out before, they have focused almost exclusively on layered composites. By contrast, we investigate composites consisting of interpenetrating phases with complex, irregular shapes. Scanning transmission electron microscopy (S/TEM) analysis of the pristine bicontinuous morphologies is first introduced followed by nuclear reaction analysis (NRA) analysis of each geometry to measure retention of He in each. Next,

S/TEM analysis of each nanocomposite after He implantation is presented and used to highlight the size and distribution of He in the samples. Finally, nanoindentation results are presented to show hardness increases as a function of He inclusion for each morphology.

7.2 Influence of Metal Nanocomposite Morphology on Helium Implantation Response

In the previous chapters, we discovered that the direction of phase separation (i.e. direction of concentration modulations) in immiscible, binary systems can be controlled via the deposition conditions [14]. In this chapter, we co-sputtered Cu and Mo at a composition of 45 at.% Cu at temperatures between 400 °C and 800 °C $[(T_H)_{\mathrm{Cu}} = 0.490.79; (T_H)_{\mathrm{Mo}} = 0.230.37]$ to induce phase separation during deposition. Nominally equiatomic composition was chosen to create bicontinuous morphologies of separating phases and avoid discrete particle formation. This deposition resulted in three distinct thin film morphologies as shown in Fig. 7.1. The detailed methodology for this experiment was outlined in Chapter 2.

As confirmed by phase field simulation, the determinant factor in controlling the final morphology during co-deposition of immiscible constituents is the interdiffusion length of the deposited species. This length is determined by a competition between the rate of phase separation and the deposition rate. Fig. 7.1 shows how the direction of phase separation changes as a function of the interdiffusion length.

Following the implantation method described in Chapter 2, the He concentration

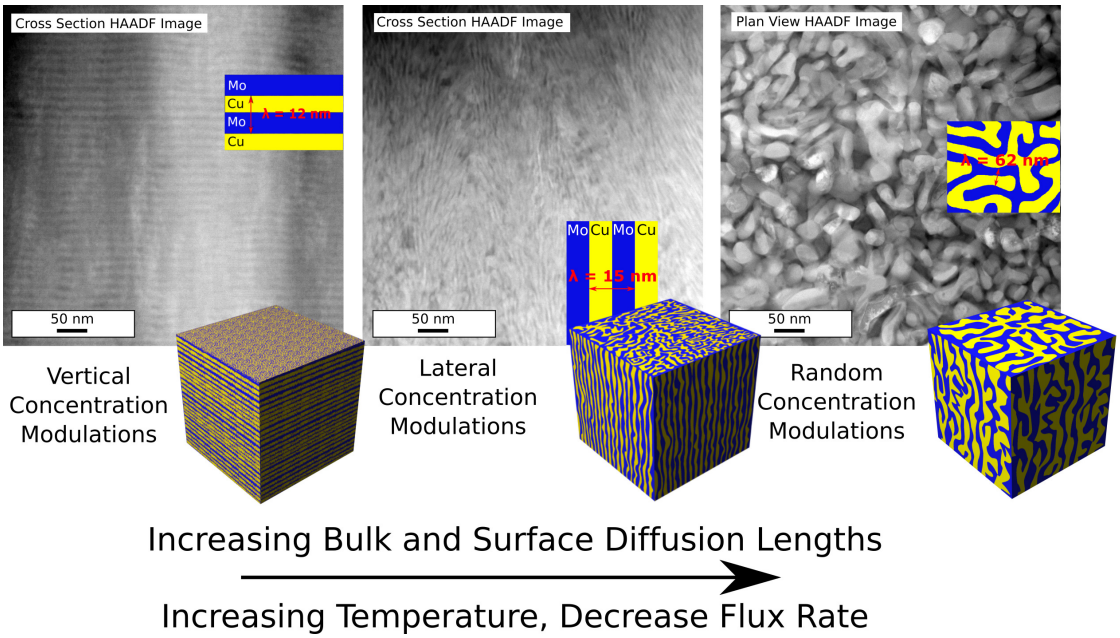

Figure 7.1: A 3D schematic of the evolution in morphology as a result of increasing interdiffusion length as a result of increasing substrate temperature. The co-deposited Cu-Mo system was observed to transition from the VCM to the LCM to the RCM structure as drawn.

for each morphology as a function of the implanted fluence is plotted in Fig. 7.2 below.

As a reference standard, a pure silicon wafer was implanted along with the three sets of CuMo films. Using the reaction pro- ton yield from the 3.010^{15} ions/cm^2 implanted Si, the ^{3}He retention in all CuMo films are easily obtained and plotted in Fig. 7.2. are estimated to be approximately $\pm 10\%$, resulting mainly from beam charge collection variations and ion stopping uncertainties among different samples.

The NRA results appear to suggest that the VCM morphology retains He efficiently while both LCM and RCM morphologies release He significantly as the fluence increases. On the other hand, He atoms are largely retained in the LCM film at low fluences but quickly leave the implanted region. As expected, the He-retention in the RCM film is somewhat in between the VCM and LCM structures.

For He outgassing to occur in the LCM and RCM composites, there must exist pathways for fast diffusion of implanted He to escape [15]. It is expected then that those morphologies containing heterophase interfaces that extend to the film surface (i.e. LCM and RCM), should exhibit increased outgassing. Unlike the VCM sample, where the interfaces extend laterally away from the surface, the tortuous interfaces in the LCM and RCM geometries should act as fast diffusion pathways for He escape. In order to explore this further, scanning transmission electron microscopy (STEM) foils were prepared and the films characterized.

The STEM allowed for simultaneous capture of both HAADF and BF-STEM

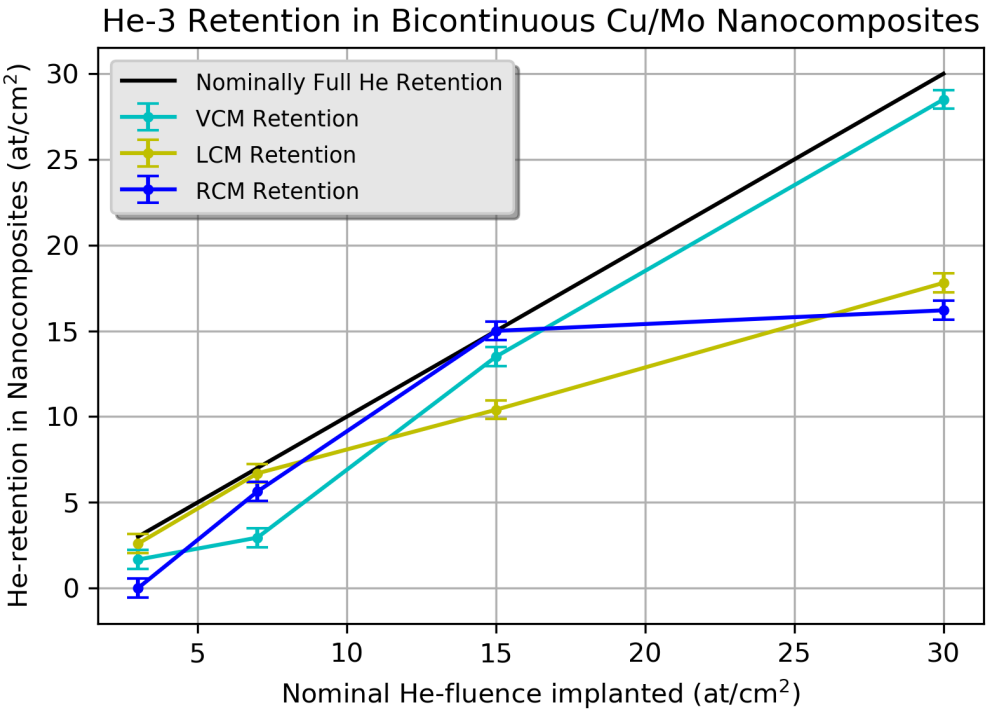

Figure 7.2: Plot of He retention in the metal composites vs the implanted nominal He fluence. Measurement error bars of 10% have been included in the presented data. It was observed that the RCM and LCM morphologies indicated a preference to retain less He as the fluence increased, which is indicative of He outgassing. From Ref. [16].

images. These are not true bright field images as diffracted electrons contribute to the intensity of the image. These BF-STEM images still allow for the observation of He bubbles in the specimens studied here and Fresnel fringes result from over- and under-focus conditions. The under and over focus conditions utilized in our study were 500 nm and +500 nm, respectively. He bubbles can readily be detected with these focus conditions.

To investigate the effect of He-release on the microstructure evolution, the LCM film was implanted to a much higher fluence of 1.0×10^{17} ions/cm^2 with a normal ^{4}He ion beam. S/TEM analysis of the Cu and Mo domains in the LCM composite after implantation shows a significant density of nanoscale He bubbles, as shown in Fig. 7.3.

The sample implanted at a fluence of 3.0×10^{16} ions/cm^2 showed the attraction of He bubbles at the FCC Cu and BCC Mo interfaces. To investigate the effect of He-release on the microstructure evolution, the LCM film was implanted to a higher fluence of 1.0×10^{17} ions/cm^2 with a normal ^{4}He ion beam. At increased fluence as shown in Fig. 7.4, He bubbles decorated the Cu/Mo boundary as demarcated by the green arrows.

In the focal series shown in the bright field STEM images, we observed strings of He bubbles along Cu and Mo phase boundaries in a pearl-like structure. This observation is consistent with the work done on He implanted FCC/BCC multilayer geometries, where the large density of misfit dislocation interfaces, nucleate He-filled

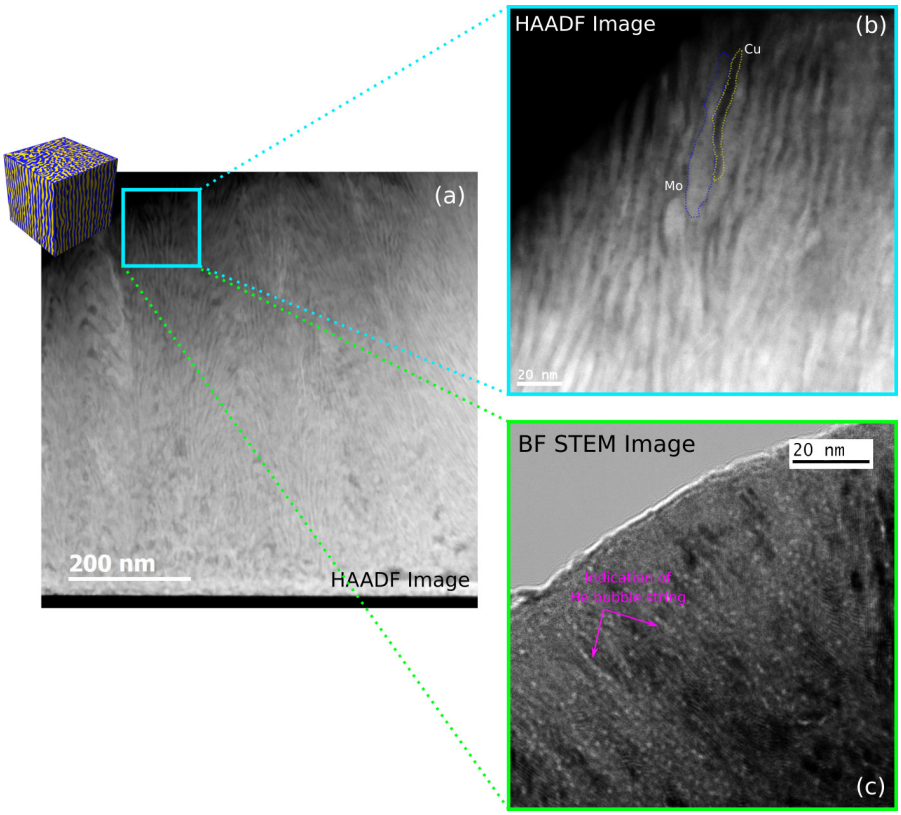

Figure 7.3: Bright field STEM and HAADF images of the nanocomposite comprised of lateral Cu and Mo concentration modulations (LCM) after 3He implantation at 20 keV and 250 C. Image (a) shows the LCM sample implanted at 3.01016 ions/cm2, where He precipitates were observed to agglomerate at the Cu and Mo interfaces, but not coalesce. The HAADF image in (b) shows the orientation of the Cu and Mo domains. The magnified BF STEM images in (c) better indicates strings of He bubbles around the phase boundaries separating Cu and Mo. Pink arrows point to He bubbles along the Cu-Mo interfaces. Linkage of the He bubbles into channels cannot be confirmed due to sample geometry and inherent sample thickness challenges, but may indicate initial nanochannel development. From Ref. [16].

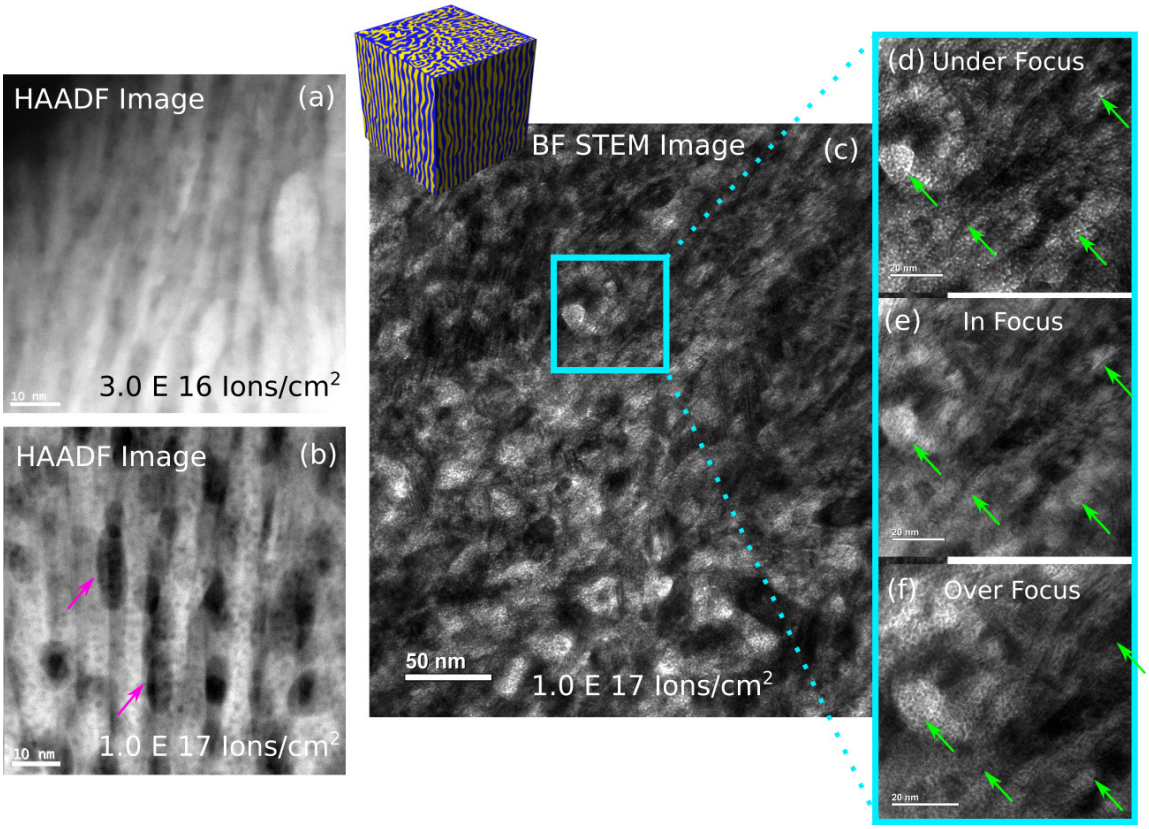

Figure 7.4: Bright field STEM and HAADF images of the nanocomposite comprised of lateral Cu and Mo concentration modulations (LCM) after 3He implantation at 20 keV and 250 °C. Image (a) shows the LCM sample implanted at 1.0×10^{17} ions/cm^2, where He precipitates were observed to agglomerate at the Cu and Mo interfaces, but not coalesce. The HAADF image in (a) shows the dark bubble formation along the FCC/BCC interface. The corresponding S/TEM bright field image is shown in (b). A focal series showing indication of He nanochannel formation is shown in images (c-f). From Ref. [16].

cavities due to preferential wetting [11].

The S/TEM Z number-contrast images from the same sample more clearly show what is occurring in the structure. The bright regions show the phase separated Mo domains while the dark domains are the Cu bands. It was observed that, while He bubbles did collect at the phase boundaries, large voids were also present within the softer FCC Cu domains as indicated by the pink arrows. This is in contrast to smaller He bubbles being present in the harder BCC Mo phase. Larger bubbles in the softer phase material has been observed in several multilayer systems, including He implanted Cu/Nb and Cu/Fe and is consistent with the results presented here [17–19].

As compared to the widely researched He-implanted multi-layer nanocomposite geometries, this LCM structure exhibited contrasting He bubble behavior. As aforementioned, He bubbles in multilayer geometries are confined within each layer by the heterophase interfaces and small domain size. The bubbles as they grow, then, exist inside the domains or align along the interfaces parallel to the film-substrate direction.

Fig. 7.5 shows He bubble distributions in the RCM composite. While the FCC/BCC interface did attract He bubbles as shown by the pink arrows, the coarse Cu and Mo domains allowed for the He precipitates to grow into each phase in a spherical shape. Without confinement by short concentration modulations, the He bubbles were not forced to coalesce into a channel and could cross into adja-

cent BCC or FCC domains, which is consistent with the results from He-implanted Cu/Nb nanolayers [20]. Selected area diffraction patterns from the 800 °C sample taken before and after implantation are provided in Fig. 7.6.

These images show that before implantation the sample exhibited the equilibrium FCC Cu and BCC Mo. After implantation the diffraction pattern indicated peak broadening between the Cu [111] peak and Mo [110] suggesting possible phase mixing or crystal size reduction.

Larger portions of the He bubbles were also observed to grow in the Cu domain. This suggests that small length domain size as in the LCM geometry is necessary to contain He bubbles at the interface.

The domain length scale and shape of interfaces in these 3D, bicontinuous Cu/Mo samples determine the mechanical properties, including hardness, modulus, and strain characteristics. To better understand the effects of He precipitates on the mechanical response of these nanocomposites, we performed a series of nanoindentation experiments on each of the film morphologies for high fluence samples.

As is shown in Fig. 7.7, before any implantation occurred, each morphology had a baseline hardness value of 2.92 ± 0.65 GPa for VCM, 4.18 ± 0.65 GPa for LCM, and 3.35 ± 0.65 GPa for the RCM morphology.

Our previous work outlines the differences in hardness between each of these morphologies in their pristine state (i.e. before implantation) and why the direction of concentration modulation will make one softer than the other [21]. In general,

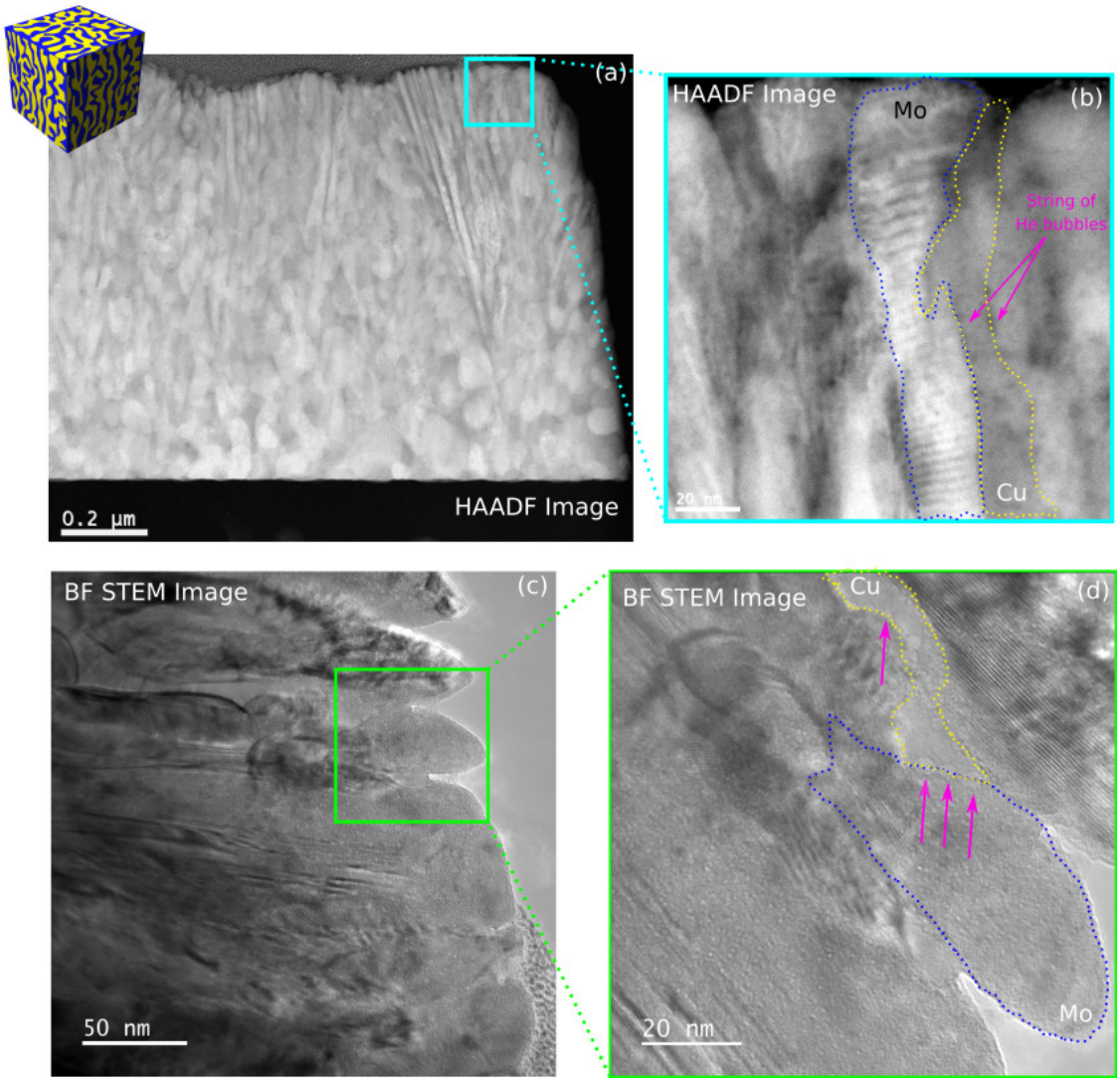

Figure 7.5: Bright field STEM images of RCM morphology after He-3 implantation at 20 keV and 250C. Significant bubble formation was observed along the Cu and Mo phase boundary and inside each Cu phase. No linkage or formation of He nanochannels were observed. Pink arrows point to He bubbles along a CuMo interface. The Cu and Mo domains are highlighted with yellow and blue, respectively. (a,b) show the HAADF images, while (c,d) show higher magnification BF STEM images. From Ref. [16].

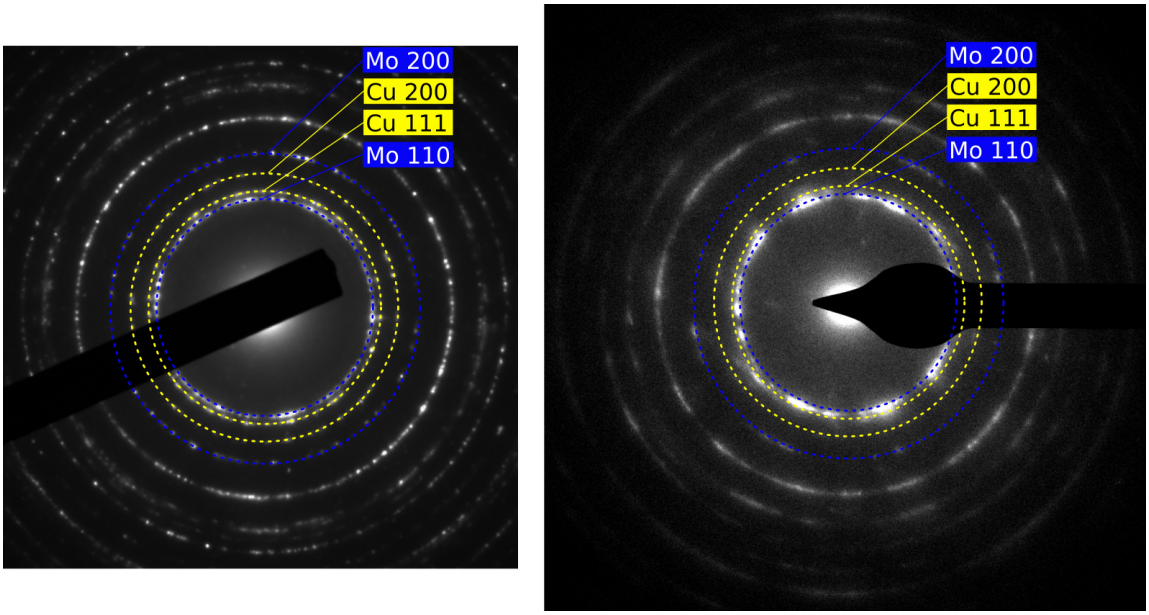

Figure 7.6: Selected area diffraction patterns from the 800 C sample (a) before irradiation and (b) after irradiation. Equilibrium FCC Cu and BCC Mo phases were present in both cases. Peak broadening was observed in (b) and could indicate Cu and Mo mixing or phase domain refinement. From Ref. [16].

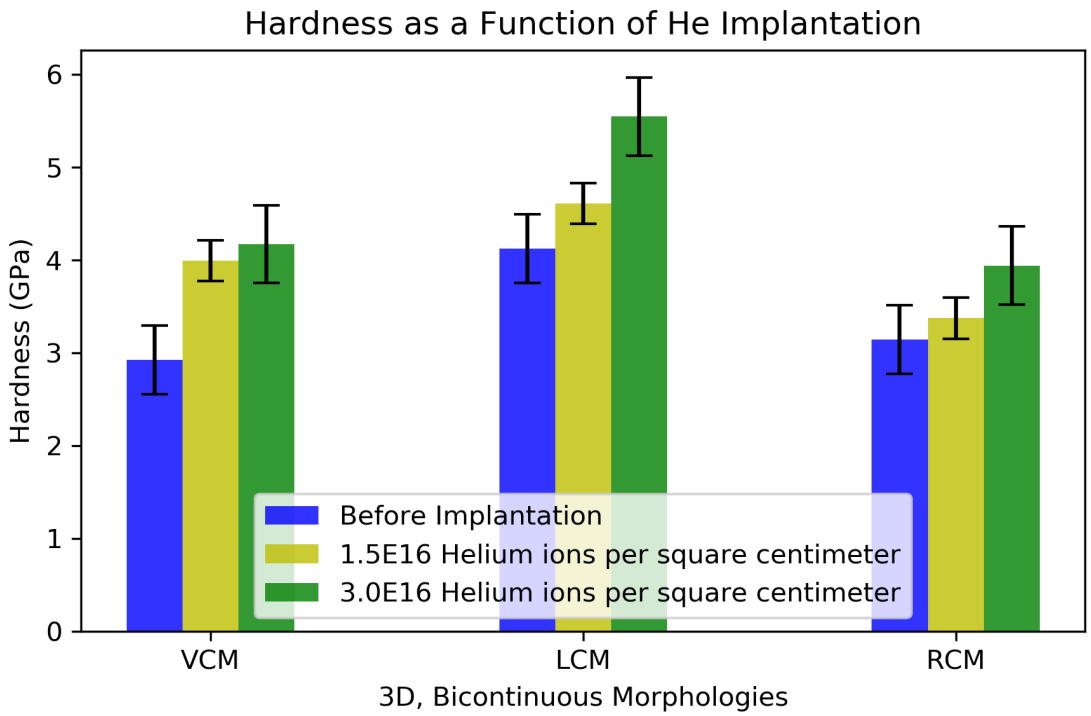

Figure 7.7: Change in nanoindentation hardness after He-ion implantation for each studied morphology. An observable increase in the hardness was observed after implantation. From Ref. [16].

different mechanisms describe the deformation for each morphology, which leads to some morphologies being harder than others.

These baseline hardness values are comparable in value to hardness data collected for multilayered FCC/BCC thin films. In these geometries, flow strength increases as the layer size decreases.Similar to these results it was generally observed here that as composition wavelength decreased, the hardness increased.

After He implantation, the hardness of each morphology increased modestly. Hardening as a result of He bubbles contained within grain interiors is a well-known phenomenon; pinning of glide dislocations at He precipitates hardens the material. For bubbles that decorate an FCC/BCC interface, the mechanism to describe hardness increase is non trivial. As outlined in [10], when a dislocation glides towards an interface its core dissipates as a result of weak shear strength at the boundary. The increased yield strength is then determined by single dislocations crossing He-lined interfaces, which provide a higher barrier to slip.

7.3 Conclusions

In summary, this work has shown that He behavior in nanocomposite is morphology dependent. The size and distribution of the He bubbles were changed when the domains were altered from lateral (LCM) to randomly orientated (RCM). Specifically, smaller He bubbles lined the lateral Cu and Mo domains in the LCM geometry. In the RCM case, the bubbles grew into larger equiaxed voids at the Cu and Mo interfaces. These He bubble morphologies can be contrasted to the widely studied

multilayer geometries. While the He bubbles similarly aligned along the heterophase interfaces, there is directionality of the He bubbles towards the free surface (i.e. film surface) that influences the He retention in the samples. As demonstrated by NRA, differences in He retention as a function of nanocomposite morphology was observed. Hardness measurements of each sample after implantation shows moderate hardening with He inclusions.

References

[1] T.R. Allen, J.I. Cole, J. Gan, G.S. Was, R. Dropek, and E.A. Kenik. Swelling and radiation-induced segregation in austentic alloys. *Journal of Nuclear Materials*, 342(1-3):90–100, 2005.

[2] X. Zhang, N. Li, O. Anderoglu, H. Wang, J.G. Swadener, T. Höchbauer, A. Misra, and R.G. Hoagland. Nanostructured cu/nb multilayers subjected to helium ion-irradiation. *Nuclear Instruments and Methods in Physics Research Section B: Beam Interactions with Materials and Atoms*, 261(1-2):1129–1132, 2007.

[3] G.S. Was. *Fundamentals of radiation materials science: metals and alloys*. springer, 2016.

[4] A.D. Brailsford and L.K. Mansur. The effect of precipitate-matrix interface sinks on the growth of voids in the matrix. *Journal of Nuclear Materials*, 104:1403–1408, 1981.

[5] J. Gan, E.P. Simonen, S.M. Bruemmer, L. Fournier, B.H. Sencer, and G.S. Was. The effect of oversized solute additions on the microstructure of 316ss irradiated with 5 mev ni++ ions or 3.2 mev protons. *Journal of Nuclear Materials*, 325(2-3):94–106, 2004.

[6] H. Ullmaier. The influence of helium on the bulk properties of fusion reactor structural materials. *Nuclear fusion*, 24(8):1039, 1984.

[7] W.D. Wilson. Theory of small clusters of helium in metals. *Radiation effects*, 78(1-4):11–24, 1983.

[8] J. Hosson, L. Caspers, and A.V. Veen. Atomistic studies of helium trapping in metals. *Radiation Effects*, 78(1-4):25–36, 1983.

[9] G.J. Thomas. Experimental studies of helium in metals. *Radiation Effects*, 78(1-4):37–51, 1983.

[10] N. Li, J.J. Carter, A. Misra, L. Shao, H. Wang, and X. Zhang. The influence of interfaces on the formation of bubbles in he-ion-irradiated cu/mo nanolayers. *Philosophical Magazine Letters*, 91(1):18–28, 2011.

[11] A. Kashinath, A. Misra, and M.J. Demkowicz. Stable storage of helium in nanoscale platelets at semicoherent interfaces. *Physical review letters*, 110(8):086101, 2013.

[12] D. Chen, N. Li, D. Yuryev, J.K. Baldwin, Y. Wang, and M.J. Demkowicz. Self-organization of helium precipitates into elongated channels within metal nanolayers. *Science Advances*, 3(11):eaao2710, 2017.

[13] T. Schuler, D.R. Trinkle, P. Bellon, and R. Averback. Design principles for radiation-resistant solid solutions. *Physical Review B*, 95(17):174102, 2017.

[14] B. Derby, Y. Cui, J.K. Baldwin, and A. Misra. Effects of substrate temperature and deposition rate on the phase separated morphology of co-sputtered, cu-mo thin films. *Thin Solid Films*, 647:50–56, 2018.

[15] M.J. Demkowicz, Y.Q. Wang, R.G. Hoagland, and O. Anderoglu. Mechanisms of he escape during implantation in cunb multilayer composites. *Nuclear Instruments and Methods in Physics Research Section B: Beam Interactions with Materials and Atoms*, 261(1-2):524–528, 2007.

[16] B.K. Derby, J.K. Baldwin, Y. Wang, M.J. Demkowicz, A. Misra, and N. Li. Influence of metal nanocomposite morphology on helium implantation response. *Scripta Materialia*, 177:229–233, 2020.

[17] K. Hattar, M.J. Demkowicz, A. Misra, I.M. Robertson, and R.G. Hoagland. Arrest of he bubble growth in cu–nb multilayer nanocomposites. *Scripta Materialia*, 58(7):541–544, 2008.

[18] N. Li, N.A. Mara, Y.Q. Wang, M. Nastasi, and A. Misra. Compressive flow behavior of cu thin films and cu/nb multilayers containing nanometer-scale helium bubbles. *Scripta Materialia*, 64(10):974–977, 2011.

[19] Y. Chen, E. Fu, K. Yu, M. Song, Y. Liu, Y. Wang, H. Wang, and X. Zhang. Enhanced radiation tolerance in immiscible cu/fe multilayers with coherent and incoherent layer interfaces. *Journal of Materials Research*, 30(9):1300–1309, 2015.

[20] W.Z. Han, N.A. Mara, Y.Q. Wang, A. Misra, and M.J. Demkowicz. He implantation of bulk cu–nb nanocomposites fabricated by accumulated roll bonding. *Journal of Nuclear Materials*, 452(1-3):57–60, 2014.

[21] Y. Cui, B. Derby, N. Li, and A. Misra. Design of bicontinuous metallic nanocomposites for high-strength and plasticity. *Materials & Design*, 166:107602, 2019.

CHAPTER VIII

Conclusions and Suggestions for Further Work

Phase separation during thin film co-deposition has been investigated through laboratory experiments on FCC/BCC thin films and phase field simulation methods. Mechanical behavior of these materials was tested under extreme conditions, including mechanical deformation and irradiation.

Homogenous and hierarchical thin film morphologies were presented and analyzed in terms of an interdiffusion analytical model. Evolution in the direction of phase separated domains was found to be a function of deposition conditions including substrate temperature and deposition rate.

At high deposition rates of 1.4 nanometers per second, bicontinuous interfaces of FCC/BCC materials were shown to change directionality as a function of deposition temperature. At a low substrate temperature of 400°, the competition between deposition rate and the rate of phase separation led to the development of vertical concentration modulations. Increasing the substrate temperature to 600°, lateral concentration modulations of the two phases were observed. At the highest temper-

atures used during deposition, 800°, the phases exhibited a bicontinuous structure of the FCC and BCC material. The competition between the rate of phase separation and deposition rate, which describes the surface diffusion length of each constituent, was the parameter used to analyze these structures.

At low deposition rates of 0.12 nanometers per second, the phase separated morphology exhibited a novel hierarchical material. Difference in surface diffusion length of the constituent materials led to phase fraction differences in the growing thin. This resulted in several different length scales of phase separation. On one length scale, large domains of FCC Cu were present and contained pseudomorphic, FCC Mo particles. On another length scale, lateral concentration modulations of the BCC and FCC material was present.

This work concluded by changing the energy of the adatoms arriving on the substrate surface by using HiPIMS. By altering the kinetic energy of the arriving adatoms, the nanoscale phase separated morphology of Cu-Fe was altered at a constant deposition temperature.

These phase separated thin films with bicontinuous interfaces were shown to exhibit high plastic flow stresses and enhanced ductility relative to monolithic thin film morphologies. Additionally, the bicontinuous character of the interfaces in these films allowed for He outgassing after having been implanted with He ions. These results show promise in using these materials in nuclear applications.

Lastly, the completion of this work has brought forth the following points which

may be both interesting and beneficial to future studies of phase separation during thin film co-deposition:

1. In Chapter 3, we discovered three distinct Cu-Mo phase separated morphologies. The thermal stability of these structures was never tested. We hypothesize that should these structures be annealed at some high temperature, each morphology would evolve into the RCM structure with bulk diffusion being activated. To test this theory, the three Cu-Mo morphologies found in Chapter 3, should be placed in a vacuum furnace and heated to some high temperature for some amount of time. The resultant structures should then be studied in the TEM. Should any structures beyond the RCM be found, this would provide insight into the thermal stability of these structures.

2. In Chapters 4 and 6, it was hypothesized that the hierarchical growth of these immiscible thin films is due to mobility differences between the constituent species. We found phase separation on multiple length scales in the Cu-Mo, Ag-Mo, and Cu-Mo-Ag thin films. Large domains of the more mobile species (e.g. Cu and Ag) we found to be interspersed inside a bicontinuous matrix. To gain insight on this hypothesis future work needs to elucidate the thermodynamic and kinetic property or properties that give rise to this hierarchical morphology. To test this hypothesis experimentally this involves vapor depositing at least four more immiscible combinations. Two combinations should include con-

stituents that have small mobility differences and the other two should include species with large mobility differences. These depositions should include not only metal-metal combinations, but metal-nitride combinations as well. Metal-nitride combinations are interesting for their functional properties and the constituents would normally have large mobility differences. Empirically plotting the resultant morphology (using TEM) against the mobility differences will give insight as to the governing mechanisms to the growth of these hierarchical thin films structures. Corresponding phase field simulation studies that include mobility differences between the depositing species, will assist in determining the governing thermodynamic or kinetic property that gives rise to these morphologies. Predictive capability over phase separating thin film morphologies will result and will be profoundly important in utilizing these morphologies in next generation technologies.

3. In Chapter 4, the origin of the FCC Mo precipitates inside of the single crystal Cu domains was not fully understood. We hypothesize that Mo particles that arrive on the Cu agglomerates during deposition are "stuck" inside those Cu grains due to low mobility of the Mo precipitates. To test this hypothesis, vapor depositions of two materials with large phase fraction differences (e.g. 90 percent Cu and 10 percent Mo) should be completed. If our hypothesis holds, the resultant film morphology should develop into the less mobile species forming

a superlattice inside large grains of the more mobile species. This study would give insight into the development of this FCC Mo superlattice that formed inside the Cu-Mo hierarchical structure.

4. In Chapter 5, a ternary Cu-Mo-Ag system was co-deposited and the initial results on the resultant morphology presented. A unique morphology of large Cu grains embedded into a bicontinuous matrix of Mo and Ag was found. A fully bicontinuous morphology was the expected morphology. We hypothesized in that work, that the more mobile species (e.g. Cu) agglomerates in the morphology leaving behind the less mobile species in the matrix. However, Ag in this system is much more mobile than Cu. We hypothesize that for ternary systems, the mobility differences of the constituents during deposition cause phase fraction differences in the growing film. However, the mechanism for why Ag does not agglomerate in the film remains an outstanding scientific challenge. An experimental study depositing the Cu-Mo-Ag systems under a range of deposition conditions is required to understand this growth mechanism. By keeping the deposition rate constant and increasing the mobility of the species during deposition through the substrate temperature will determine whether Ag begins to agglomerate at higher temperature or not at all. Understanding the growth of these mutually immiscible ternary systems will guide our understanding of the growth mechanisms during binary system film growth.

5. In Chapter 6, a new co-deposition technique known as HiPIMS was used to co-deposit the immiscible Cu-Fe system. Refinement of the phase separated structure was shown at a constant deposition temperature but increasing target ion current. We hypothesized in that work, that utilizing HiPIMS at a lower process gas pressure would eliminate the porosity shown in the Cu-Fe films produced. Fewer target neutral and ion collisions with the process gas is predicted to lower the degree of porosity in the film. In the future, a HiPIMS study should be done on an immiscible system at a process gas pressure of 3 mT and a range of target ion currents. This study would give insight as to whether it is possible to have a sufficient target ion current at low pressure, but still maintain the increased interdiffusion length that HiPIMS affords the growth.

6. In Chapter 8, NRA suggested the outgassing of He in nanocomposites of Cu and Mo with random concentration modulations. We hypothesized that the bicontinuous interfaces in this morphology that extend in three dimensions towards each surface, provided fast diffusion pathways (i.e. along the interface) for He bubbles and promoted outgassing. This hypothesis was tested using NRA methods, which measured the He retention in each nanocomposite morphology as a function of fluence. However, this hypothesis was not confirmed via TEM BF imaging. We hypothesize that if such outgassing is occurring,

nanochannels filled with He should have formed along the interface. High resolution S/TEM imaging of these bicontinuous interfaces after He implantation should show the presence of these channels. Through focus contrast imaging will highlight the location of these bubbles. Our current study did not have access to this instrumentation before publication. It is a worthy scientific endeavor for the future that will show the mechanism behind He outgassing in these bicontinuous nanocomposite structures.